University of Sussex

A University of Sussex PhD thesis

Available online via Sussex Research Online:

http://sro.sussex.ac.uk/

DESIGN OF CUSTOMISED TOTAL KNEE IMPLANTS WITH MUSCULOSKELETAL DYNAMIC SIMULATIONS

LINJIE WANG

A thesis submitted in partial fulfilment of the requirements of the University of Sussex for the degree of Doctor of Philosophy

Department of Engineering and Design

University of Sussex

April 2019

Declaration

I hereby declare that this thesis has not been and will not be, submitted in whole or in part to another University for the award of any other degree.

Signature: Linjie Wang……………………………………………………….

Abstract

Effects of a customised total knee implant (CTKI) on the contact forces and relative motions of the tibiofemoral and patellofemoral joints have been investigated with computer simulations by applying the patient-specific muscle forces on the lower limb and the joint reaction forces at the ankle and hip joints.

Firstly, a method was proposed and realized to create a CTKI based on the geometry of a patient's knee joint using ANSYS Mechanical APDL. Secondly, a patient-specific musculoskeletal model was built to calculate the muscle forces and joint reaction forces during a squat motion. Finally, a dynamic finite element (FE) model was created in ANSYS incorporating the aforementioned forces and the CTKI to calculate the contact forces and relative motions of the tibiofemoral and patellofemoral joints. In addition, an off-the-shelf symmetric total knee implant (STKI) with cruciate ligaments (CLs) retained was simulated for comparison analysis.

Knee joint collateral ligaments with nonlinear properties and pretensions were created in the dynamic FE model. A series of dynamic simulations of a squat motion with different initial laxities of the collateral ligaments were performed on the CTKI model under three treatment scenarios of CLs: both CLs retained, anterior cruciate ligament (ACL) removed and both CLs removed. Results showed that only the CTKI model with both CLs retained resulted in similar femoral external rotation and posterior translation with those of the healthy knees. There were not big differences in the tibiofemoral compressive forces among the three scenarios. All the three tibiofemoral compressive forces showed good agreement with other research results from either in-vivo measurements or simulations. The CTKI has better mobility than the traditional STKI designs.

The curvatures of the tibial bearing surfaces have been varied in the transverse and longitudinal directions. Compared with the STKI, the CTKIs could restore patient's knee function to normal, though the tibiofemoral compressive force observed in CTKIs was larger than that of the STKI in the late 25° of simulated knee flexion angles, which was caused by the large passive knee ligament forces and the larger knee motion ranges.

The patella has also been studied and compared between the unresurfaced and resurfaced patellar components. The laxity of patellofemoral ligament was firstly tested on the unresurfaced patellar component. Then, the same dynamic boundary conditions were applied on three different patellar button components. Differences were found in the patellar internal rotation and medial tilt motions between the unresurfaced and resurfaced patellar components. The original patellar button component showed contact between the patellar bone and the femoral component apart from contact between the patellar component and the femoral component. The scaled-up button was able to avoid the contact between the patellar component and the femoral component and reduce the patellar medial translation. However, it resulted in larger patellofemoral force than that of the original and flat patellar components. The patellofemoral forces on the scaled-up patellar component were more fluctuating due to less conformity of the contact surfaces. The scaled-up patellar components were found to have two contact areas on the patellofemoral joint, while the original one had only one contact area.

Acknowledgements

First and foremost, I would like to thank my supervisor, Dr Chang Jiang Wang who has given me the most support and encouragement for completing this work. Without his enlightenment and invaluable suggestions, this work could not have been completed. I thank him for his patience and his willingness to give me freedom to explore the unknown.

I would also like to thank my second supervisor, Prof Julian Dunne who introduced me to Dr Chang Jiang Wang and provided a precious opportunity of studying at University of Sussex. I thank the Department of Engineering, University of Sussex for its financial support and thank Professor B.J. Fregly and his colleagues for providing publicly accessible data.

Last but not least, I appreciate my parents for their infinite care and love. It is them who have been encouraging me to bravely pursue my happiness and fulfil my dreams. I would also appreciate my most lovely girlfriend, Jennifer Ka Chun Choi. It is her thoughtful kindness and heart-warming love that accompanied me to get through the most difficult time. My life has become more colourful and joyful because of her.

Table of contents

List of figures

List of tables

Abbreviations

A-A	Adduction-abduction
aACL	Anterior bundle of anterior cruciate ligament
ACL	Anterior cruciate ligament
aLCL	Anterior bundle of lateral collateral ligament
aMCL	Anterior bundle of medial collateral ligament
A-P	Anterior-posterior
aPCL	Anterior bundle of posterior cruciate ligament
APDL	ANSYS parametric design language
BCS	Bi-cruciate stabilized
BF	Biceps femoris
BW	Body weight
CL	Cruciate ligament
CLL	Collateral ligament
CMC	Computed muscle control
CR	Cruciate-retaining
CS	Coordinate systems
CT	Computed tomography
CTKI	Customised total knee implant
EMG	Electromyography
Eq.	Equation
FD	Forward dynamics
FDK	Force dependent kinematics
FE	Finite element
F-E	Flexion-extension
FKN	Normal contact stiffness factor
GAS	Gastrocnemius
ID	Inverse dynamics
I-E	Internal-external
IK	Inverse kinematics
KKS	Kansas knee simulator
KP	Key point

LCL	Lateral collateral ligament
LGAS	Lateral gastrocnemius
lPFCL	Lateral patellofemoral collateral ligament
lRL	Lateral retinaculum ligament
lRLi	Inferior bundle of lateral retinaculum ligament
lRLm	Middle bundle of lateral retinaculum ligament
lRLs	Superior bundle of lateral retinaculum ligament
MCL	Medial collateral ligament
MGAS	Medial gastrocnemius
M-L	Medial-lateral
mLCL	Middle bundle of lateral collateral ligament
mMCL	Middle bundle of medial collateral ligament
MPC	Multipoint constraint
mPFCL	Medial patellofemoral collateral ligament
MRI	Magnetic resonance imaging
mRL	Medial retinaculum ligament
mRLi	Inferior bundle of medial retinaculum ligament
mRLm	Middle bundle of medial retinaculum ligament
mRLs	Superior bundle of medial retinaculum ligament
OKR	Oxford knee rig
pACL	Posterior bundle of anterior cruciate ligament
PCL	Posterior cruciate ligament
PFCL	Patellofemoral collateral ligament
PID	Proportional-integral-derivative
PL	Patellar ligament
pLCL	Posterior bundle of lateral collateral ligament
pMCL	Posterior bundle of medial collateral ligament
pPCL	Posterior bundle of posterior cruciate ligament
PS	Posterior-stabilised
QECD	Quadric edge collapse decimation
PSR	Poisson surface reconstruction
RF	Rectus femoris
RL	Retinaculum ligament

ROM	Range of motion
RRA	Residual reduction algorithm
SAR	Sartorius
S-I	Superior-inferior
SM	Semimembranosus
SO	Static optimization
SOL	Soleus
ST	Semitendinosus
STKI	Symmetric total knee implant
TA	Tibialis anterior
TFL	Tensor fasciae latae
TKA	Total knee arthroplasty
TKI	Total knee implant
TKR	Total knee replacement
UKR	Unicompartmental knee replacements
VI	Vastus intermedius
VL	Vastus lateralis
VM	Vastus medialis
2D	Two-dimensional
3D	Three-dimensional

Chapter 1

Introduction

Total knee replacement (TKR), also known as total knee arthroplasty (TKA), has been an effective surgical procedure to relieve the pain of patients of severe osteoarthritis. The number of people undergoing TKR surgery is still increasing. According to the National Joint Registry (NJR) for England, Wales and Northern Ireland, around 90 000 TKRs were carried out each year.[1] The number of TKR surgeries was also projected to increase to 3.48 million by 2030 in the USA.[2]

Although the TKR is one of the most common procedures in orthopaedic surgery and one of the most successful in all of medicine, the satisfaction of patients after the surgery is only about 80% [3–5]. According to the literature [6,7], the TKR is not achieving its goal of relieving the residual pain or restoring the limited function in large proportion of patients. 27% of clinically residual knee pain was caused by the femoral implant overhang and the overhang was correlated with a 90% increase in the risk of pain.[8] The study of Bonnin et al. [9] also pointed out that the mediolateral oversizing might lead to worse clinical results and unexplained pain in patients. As regard to the functional limitation of implanted knees, it is mainly because of the widely used traditional design of the off-the-shelf total knee implants (TKIs). The traditional designs of TKIs are characterized with the symmetric geometric shape and simplified arc-shaped condyles. Due to the standardisation of sizes and types of the traditional designs, it would not only restrain the mobility of implanted knees, but also lead to the overhang or underhang of the femoral component over the bones, bringing in potential risks of postoperative knee pains and discomfort.

Under this circumstance, experimental asymmetric design of TKI was tested and compared with the symmetric posterior stabilized designs by Walker et al. [10]. The asymmetric design was concluded to be able to produce the asymmetries in the motion of the anatomic knee. ConforMIS is the first and only company that apply customised TKI based on patient-specific knee shapes. Its customised TKI is built based on three curves: medial, lateral J-curves and patellofemoral J-curve which can be extracted from the geometric information of patient-specific knee [11,12].

Patil et al. [12] used the active infrared surgical navigation system and Oxford knee rig to compare a customised knee implant from ConforMIS with a standard off-the-shelf cruciate retaining (CR) TKI from DePuy and found that patient-specific designed knee implant could produce kinematics that were more closely resembling normal knee kinematics than standard off-the-shelf implants. Zeller et al. [5] also conducted the kinematic analysis between the ConforMIS implant and a traditional design TKI from Zimmer by using fluoroscopic method. Same conclusion was drawn that the customised TKI could produce a kinematics more similar to a normal knee.

1.1 Research aim and objectives

Given the drawbacks of off-the-shelf symmetric TKIs, and lack of studies on the design and analysis of customised TKI, this study aims to create a customised TKI and predict its performance using a dynamic finite element model with consideration of patient-specific muscle forces.

The objectives of this thesis are:

- proposing a computer modelling method of creating a customised TKI based on patient's knee anatomy;

- calculating patient-specific lower limb muscle forces and ankle joint loads for evaluating dynamic responses of the customised TKI;

- creating a patient-specific finite element knee simulation model that incorporates the effect of the lower limb inertias, muscle forces and ankle joint loads;

- analysing and comparing motions and forces of the tibiofemoral and patellofemoral joints between the customised TKI and an off-the-shelf TKI.

1.2 Structure of the thesis

The thesis consists of ten chapters.

Chapter 1 introduces an outline of the research and the structure of the thesis.

Chapter 2 is the literature review. Human knee joint, total knee replacement implants, knee test rigs and musculoskeletal models are introduced and described.

Chapter 3 proposes a method of creating a customised femoral implant based on the patient-specific shape of distal femur and building the tibial implant based on the condylar surfaces of the femoral implant. The parametric modelling of both femoral and tibial components is performed in ANSYS Mechanical APDL. The original three dimensional (3D) knee joint model is built from the knee joint computed tomography (CT) images which are downloaded from the online accessible resource [13].

In **Chapter 4**, a patient-specific musculoskeletal model is built to calculate the muscle forces and joint reaction loads for the squat motion using OpenSim. The kinematic marker data and ground reaction forces used for musculoskeletal model simulations are from the same subject whose knee joint CT images are used for creating the customised total knee implants (CTKIs) in Chapter 3. All the experimental data including CT scans were downloaded from the online accessible resource [13] and measured and collected by Fregly et al. [14].

In **Chapter 5**, an ANSYS transient dynamic FE model is created based on the Oxford knee rig and Kansas knee simulator. In the dynamic model, the TKI models are coupled with the knee joint ligaments and muscles across the knee and ankle joints. Two contact pairs of tibiofemoral and patellofemoral joints are recruited.

In **Chapter 6**, the dynamic performances of both CTKI and one symmetric TKI (STKI) from DePuy are investigated. The tibiofemoral compressive forces, relative motions and ligament forces and elongations of two designs are compared. The results of CTKIs under three scenarios of knee cruciate ligaments are also shown and compared.

In **Chapter 7**, the effect of curvatures of tibial bearing surfaces on the dynamic responses of CTKIs is investigated. Apart from the tibiofemoral compressive forces, relative motions and ligament forces and elongations, the tibiofemoral and patellofemoral contact stresses of CTKIs in five knee flexion angles are also shown and compared with those of the STKI.

In **Chapter 8**, the effect of resurfaced and unresurfaced patella on the knee joints is investigated. The joint forces, relative motions and contact stresses of both patellar models are compared and analysed. The size and shape of patellar button implants are also studied to compare their influences on the patellofemoral relative motions and contact stresses.

In **Chapter 9**, the main findings, conclusions and research limitations are summarised and discussed.

Chapter 10 is the last chapter of this thesis. It puts forward some ideas about improving the customised total knee implant modelling and the musculoskeletal modelling for future study.

1.3 Original contribution to the body of knowledge

The main contribution of the research is creating a computer model of customised total knee implant and a dynamic computer knee simulation model with consideration of physiological muscle forces and ground reaction loads, in order to address patient dissatisfaction with traditional TKI due to the component overhang and restricted mobility. This work is the first to combine the total knee implant model with the patient-specific muscle forces and joint reaction loads in the knee joint simulation. It can virtually test either customised total knee implants or traditional designs with realistic loads, and optimise design parameters. The customised TKI is computationally simulated to have better mobility than the traditional design, and meanwhile have the potential to replicate normal knee kinematics.

The original contributions of this thesis to the body of knowledge are listed below:

- A method of creating customised total knee implant is proposed. The femoral component is built based on the geometry of the patient-specific distal femur. The condylar surface curvature of the femoral component is then used to determine the tibial component bearing surfaces.

- A dynamic FE knee simulation model is built based on the Oxford knee rig and Kansas knee simulator to assess the dynamic performances of total knee replacement implants. Unlike previous studies, the closer-to-physiological muscle forces across the knee and ankle joints are applied for simulation along with the nonlinear properties of ligaments. The effect of the quadriceps muscle wrapping around the femur distal is also considered. The improved simulation models also allow applying three translational forces and two torques on the ankle joint. The muscle insertion locations are determined from the OpenSim patient-specific musculoskeletal model, which makes simulation closer to physiological environment rather than using a mechanical experiment rig.

- The joint reaction forces and muscle forces applied on the dynamic FE model are patient-specific and imported from the simulated results of the OpenSim musculoskeletal model. In the process of calculating those forces, the ground reaction forces are included. This can help directly observe and understand the dynamic responses and characteristics of the customised implant under more practical, physiological and patient-specific loading conditions rather than using simplified experimental forces.

- The FE dynamic responses of the CTKI under three different scenarios of knee cruciate ligament treatments are simulated and compared along with a traditional design, STKI. The loading on the medial and lateral knee condyles during the squat motion can be obtained together with the motions of knee joint and all ligaments forces and their elongations. This helps understand kinematic and kinetic differences between the CTKI and STKI.

- The influence of the curvatures of tibial bearing surface on the tibiofemoral joint is investigated. The stresses of both tibiofemoral and patellofemoral joints of CTKI and STKI are shown and compared.

- The influence of the unresurfaced and resurfaced patella on the patellofemoral joint is analysed. The influence of the size and shape of patellar button components on the patellofemoral joint is also investigated.

Chapter 2

Literature review

2.1 Human knee joint and its anatomy

Human knee is one of the largest and most complex joint in the human body. As shown in Figure 2. 1, the knee joint consists of three major bones: a femur, tibia and patella bone. The knee joins the thigh with the leg/shank and consists of two joints: one between the femur and tibia, which is called tibiofemoral joint, and another between the femur and patella, which is patellofemoral joint.[15] The femur distal consists of two condyles and a trochlear groove. The femoral condyle which is located on the inner side of the body is called medial condyle, while another is named lateral condyle which is on the outer side of the body. The medial condyle is larger than the lateral condyle due to more weight bearing caused by the centre of mass being medial to the knee. The two femoral condyles articulate with the corresponding tibial bearing surfaces, while the femoral trochlear groove accommodates the patella and allows it to slide as a pulley system.
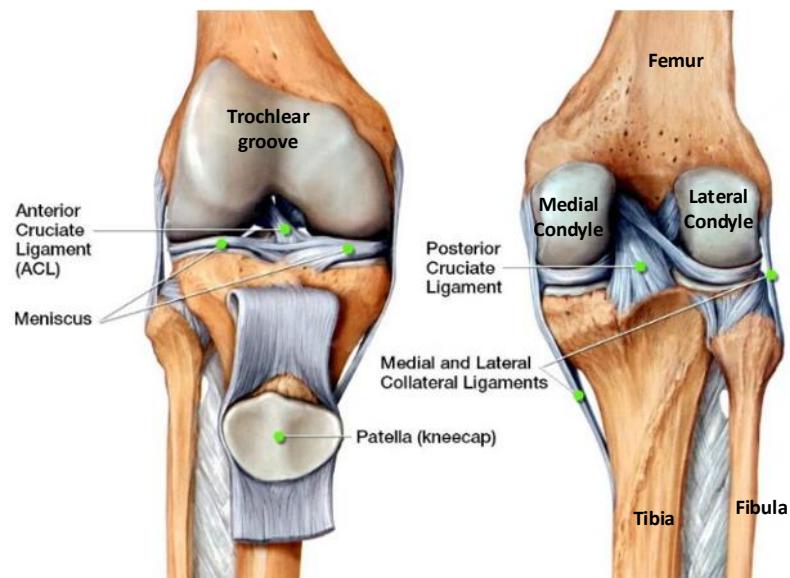
Figure 2. 1 Knee joint bones and some ligaments [16]
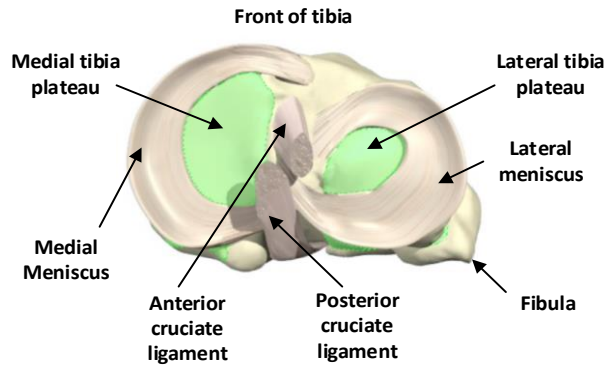
Figure 2. 2 Tibia in the proximal view [17]
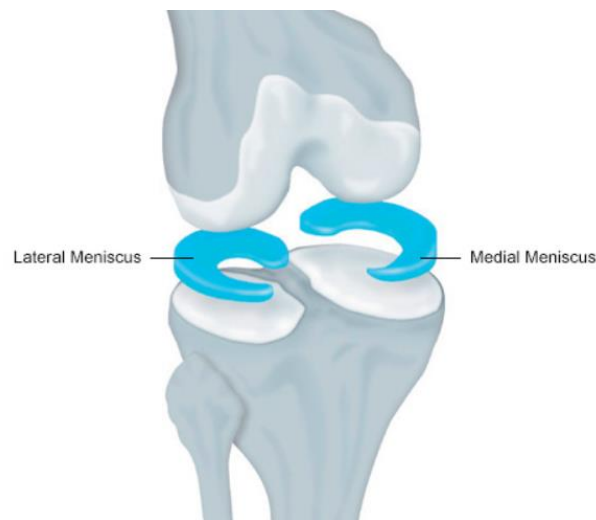
Figure 2. 3 Medial and lateral menisci [18]

In Figure 2. 2 and Figure 2. 3, two crescent-shaped pieces of cartilage are shown and called the medial and lateral menisci. They are located on the top of the tibial plateau and act to protect and cushion the joint surface and bone ends, such as dispersing the load of the body weight, reducing friction during movement, and absorbing shock between the femur and tibia produced by activities such as walking, running and squatting. Because of the menisci's wedge shape in the radial cross section, two tibial bearing areas are actually concave shapes, although the lateral tibial plateau is convex shape.

Surrounding the bones of knee joint are ligaments which play important roles in protecting the knee and provide stability: cruciate ligaments (anterior and posterior cruciate ligaments, ACL and PCL) which are located in the centre of the knee as shown in Figure 2. 1 and Figure 2. 2, tibiofemoral collateral ligaments (medial and lateral

collateral ligament, MCL and LCL) on two sides of the knee respectively in Figure 2. 1, patellofemoral collateral ligaments (medial and lateral patellofemoral collateral ligaments, mPFCL and lPFCL) in Figure 2. 4 that connect patella with femur and patellar, retinaculum ligaments/patellotibial ligaments (medial and lateral retinaculum ligaments, mRL and lRL) in Figure 2. 4 connecting patella with tibia and providing medial and lateral stability to the patella. The ACL prevents the femur from sliding backward on the tibia (or the tibia sliding forward on the femur) and also controls rotational movement of the tibia in relation to the femur, while the PCL prevents the femur from sliding forward on the tibia (or the tibia from sliding backward on the femur). The MCL and LCL prevent the femur from sliding side to side and restrict extreme varus-valgus motion. The latter four ligaments are recognized as four major ligaments that play the most significant roles in stabilizing the knee joint during all kinds of daily activities.
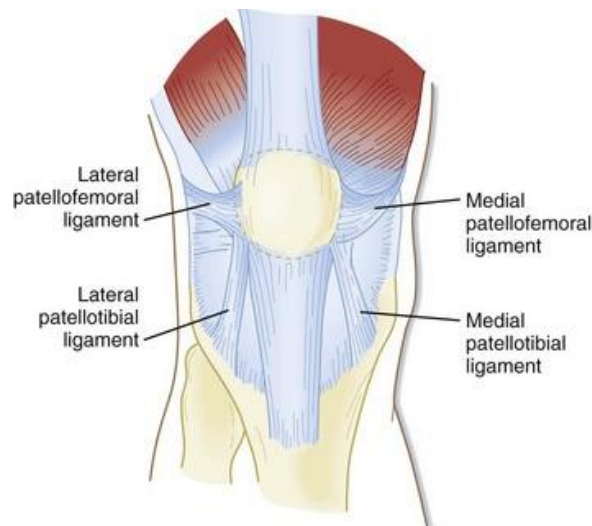
Figure 2. 4 Patellofemoral and Patellotibial ligaments [19]
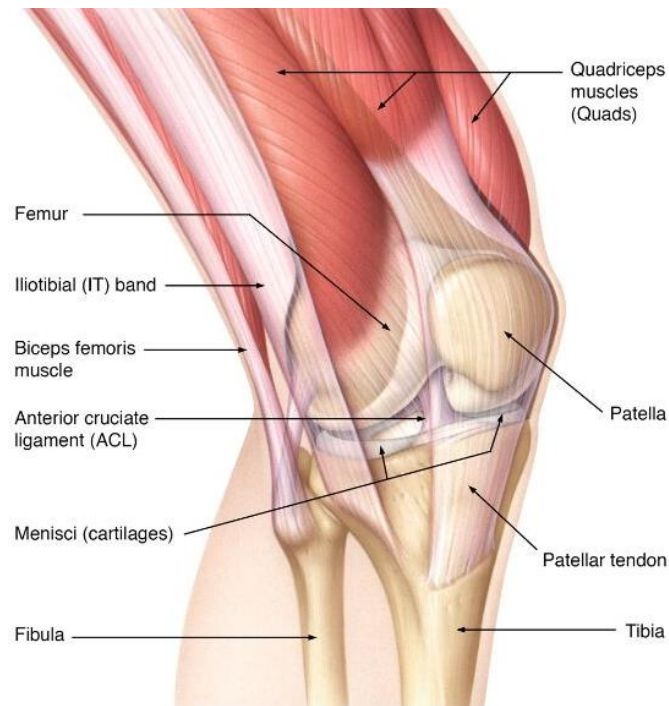
Figure 2. 5 Knee joint anatomy lateral view [20]

Besides the effective action of ligaments, muscles acting over the knee joint provide secondary dynamic stability.[21] The most important one is the quadriceps muscle group which is shown in Figure 2. 5. It is composed of four distinct muscles and provides the main extension moment for the knee joint. The four distinct muscles are the rectus femoris (RF), the vastus medialis (VM), the vastus lateralis (VL) and the vastus intermedius (VI) shown in Figure 2. 6. Among quadriceps muscles, the RF is the only muscle bundle that acts on both the hip and knee joints, while the other three bundles connect the patella with the femur bone on different muscle insertion points. The quadriceps muscle loads are balanced by the passive force produced by the patellar tendon in Figure 2. 5 or also called patellar ligament (PL) that attaches to the tibial tuberosity. The hamstrings muscles which are located on the back of thigh act antagonistically to the quadriceps muscles to flex the knee. They are comprised of three muscles: the biceps femoris (BF), the semitendinosis (ST) and semimembranosus (SM) muscles. The hamstrings flex the knee while also extending the hip. Many of the muscles that cross the knee joint also cross other joints, giving them functionality about two joints. It is this dual functionality and partial redundancy which leads to complexity when modelling the joints.[22] A summary of the muscles that act across the knee joint is shown in Table 2. 1.
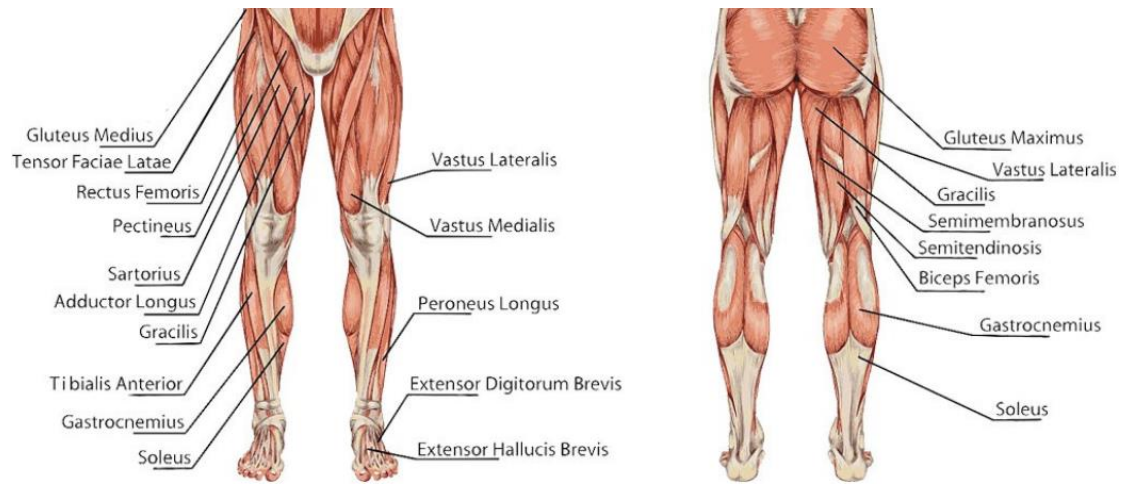
Figure 2. 6 Human lower extremity muscles [23]

Table 2. 1 Major muscles acting over the knee joint [24]

Muscle	Origin	Insertion	Action
Gracilis	Inferior edge of symphysis pubis	Proximal medial surface of tibia	Adducts thigh at hip joint; flexes and rotates leg at knee joint
Pectineus	Pectineal line of pubis	Distal to lesser trochanter of femur	Adducts and flexes thigh at hip joint
Adductor longus	Pubis—below pubic crest	Linea aspera of femur	Adducts, flexes, and laterally rotates thigh at hip joint
Adductor brevis	Inferior ramus of pubis	Linea aspera of femur	Adducts, flexes, and laterally rotates thigh at hip joint
Adductor magnus	Inferior ramus of ischium and pubis	Linea aspera and medial epicondyle of femur	Adducts, flexes, and laterally rotates thigh at hip joint
Sartorius	Anterior superior iliac spine	Medial surface of tibia	Flexes knee and hip joints; abducts hip joint; rotates thigh laterally at hip joint; and rotates leg medially at knee joint
Quadriceps femoris		Patella by patellar tendon, which continues as patellar ligament to tibial tuberosity	Extends leg at knee joint
Rectus femoris	Anterior superior iliac spine and lip of acetabulum		
Vastus medialis	Greater trochanter and linea aspera of femur		
Vastus lateralis	Medial surface and linea aspera of femur		
Vastus intermedius	Anterior and lateral surfaces of femur		
Biceps femoris	Long head—ischial tuberosity; short head—linea aspera of femur	Head of fibula and lateral epicondyle of tibia	Flexes knee joint; extends and laterally rotates thigh at hip joint
Semitendinosus	Ischial tuberosity	Proximal portion of medial surface of body of tibia	Flexes knee joint; extends and medially rotates thigh at hip joint
Semimembranosus	Ischial tuberosity	Proximomedial surface	Flexes knee joint; extends and medially rotates thigh at hip joint
Gastrocnemius	Lateral and medial epicondyle of femur	Posterior surface of calcaneus	Plantar flexes foot at ankle; flexes knee joint
Soleus	Posterior aspect of fibula and tibia	Calcaneus	Plantar flexes foot at ankle

2.2 Knee Kinematics

Driven by the lower extremity muscles and restricted by the knee articulation structures, the femur can move with respect to the tibia in a controllable and regular way. The main rotation of the knee is flexion-extension (F-E). Apart from this motion, there are also internal-external (I-E) rotation, adduction-abduction (A-A) rotation, anterior-posterior (A-P) translation, medial-lateral (M-L) translation and superior-inferior (S-I) translation

between femur and tibia. The magnitudes and patterns of these motions are dependent on the geometric shapes and conditions of knee joint, effects of muscles and ligaments around knee joint, and external loads such as the ankle joint loads transmitted from the ground reaction forces. When the knee is flexed, the shank or lower leg is internally rotated, while when the knee is extended, the shank is externally rotated. With the flexion of knee joint, the passive A-A rotation of knee joint also increases. It can reach a few degrees with the knee flexion up to 30°. When the knee is flexed beyond 30°, instead, motion in the frontal plane again decreases because of the limiting functions of the soft tissues.[25, 26]

During the knee flexion, the tibia also moves posteriorly with regard to the femur. The mean A-P range measured by Belvedere et al.[26] was 25.8±5.9 mm and it mostly occurred within the first 70° of knee flexion. Additionally, the mean range for the M-L translation was reported 4.8±2.8 mm, while that of the S-I translation was 23.8±3.3 mm.

Freeman et al.[27] used magnetic resonance imaging (MRI) to study the relative movements between the femur and tibia. To understand the knee motion, the knee flexion was divided into three arcs on the femoral condyle in the sagittal plane, which were extension arc, functional active arc and passive arc. The extension arc was defined as the range between 20° knee flexion and full extension. The knee flexion angles between 20° ±10° and 110°/120° was called the functional active arc that covered most of human daily activities. Over this arc, the medial condyle was found not to move anteroposteriorly due to the medially cup-shaped tibial bearing surface, while the lateral condyle rolled back producing the tibial internal rotation with the knee flexion. The posterior horn of the medial meniscus was attached firmly to the tibia to provide a posterior wall to the cup-shaped tibial surface, however, the lateral meniscus moved with the anteroposterior motion of the lateral femoral condyle in relation to the tibia during the knee flexion and rotation. Between 110°/120° and 145°/160° knee flexion was the passive arc, in which the effective moment arm was not affected by the effect of thigh muscles. Both femoral condyles were found to be in contact with the posterior horns of the menisci instead of the tibial articular surfaces.

2.3 Total knee component designs

The knee is vulnerable to injury and to the development of osteoarthritis. Once patients are diagnosed with severe destruction of the knee joint associated with the progressive pain and impaired function, they would be recommended for the total knee replacement (TKR). During a surgery of TKR as shown in Figure 2. 7, a surgeon removes the surface of patient's bones that have been damaged by osteoarthritis or other causes, and replaces the knee with an artificial implant that can best fit patient's anatomy.
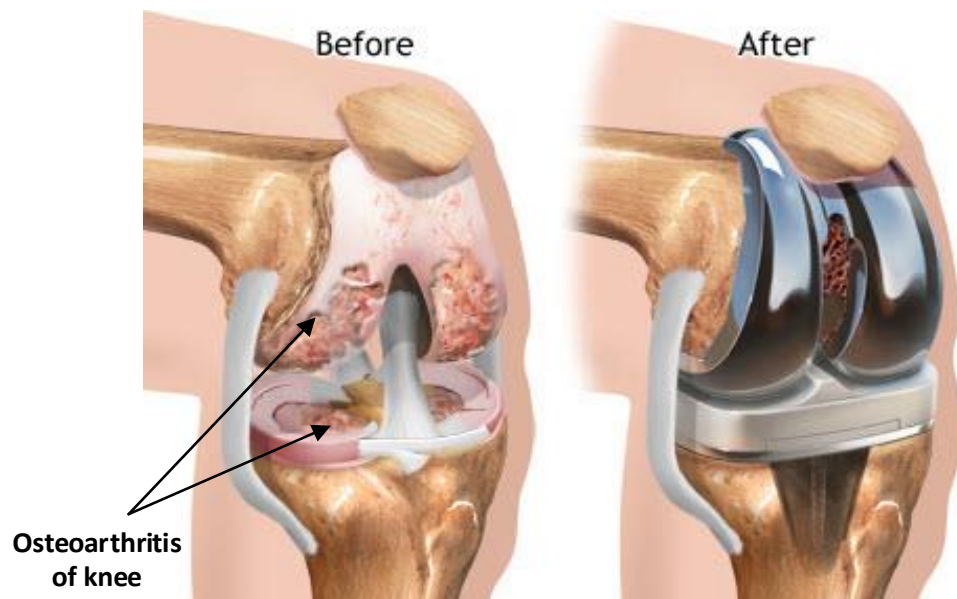
Figure 2. 7 Before and after total knee replacement (TKR) surgery [28]

There are typically three components used in the traditional TKRs: femoral component, tibial component and patellar implant. The femoral component (see Figure 2. 8, B) is generally made of cobalt-chrome alloy and comprised of two symmetric arc-shaped condylar surfaces. In the middle anterior of the two condylar entities is a groove that allows the patella to move up and down as the knee joint flexes and extends. The tibial component (see Figure 2. 8, C and D) usually consists of two parts: tibial insert or spacer which is made of ultra-high molecular weight polyethylene (UHMWPE), and titanium-alloy tibial tray. The patellar implant (see Figure 2. 8, F) is a dome-shaped or button-shaped piece of polyethylene that is attached to the retained patella bone and in contact with the femoral groove during all sorts of daily activities.
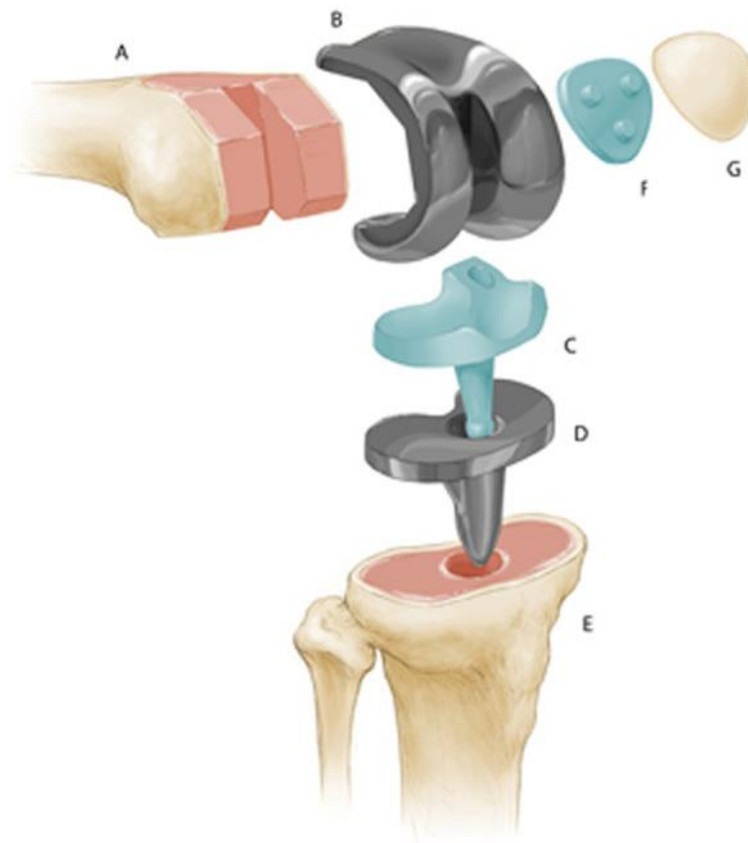
Components of knee replacement surgery. The femur is cut (A) to fit the femoral component (B); the tibial plate (D) inserts into the hollowed-out tibia (E); the spacer (C) sits between the femoral and tibial implants; the patellar implant (F) fits onto the underside of the knee cap (G).

Figure 2. 8 Components of TKR [29]

It was reported in literature [30] that there were over 150 designs of knee implants on the market. According to the implant functions and surgery purposes, the implant designs could be categorised into several groups. One of the most commonly used type of implant in TKR is a posterior-stabilized (PS) component [31]. In this design, the cruciate ligaments are removed and a cam-post mechanism substitutes (see Figure 2. 9) for the function of posterior cruciate ligament (PCL). With the cam-post mechanism, the femur bone can be prevented from sliding forward too far in relation to the tibial counterpart. However, according to the study of Van Duren et al. [32], the cam-post mechanism was not very effective in that it did not generate normal femoral roll-back, and the cam might contribute to roll back above 80 degree. Additionally, this type of design may induce some other problems such as high risk of cam-mechanism polyethylene wear. Therefore, the ultra-congruent (UC) inserts, also named deep-dish components, were developed in

order to increase the implant conformity and to reduce stresses on the bone-implant interface.[33] But the problem it would cause was early loosening due to the high congruence and low mobility of the implant.[34] Lützner et al. [35] concluded that UC inserts might be useful to preserve bone stock in case of PCL deficiency, but it could not increase the range of motion (ROM). Another design similar to the PS component with a post-cam mechanism is the cruciate-substituting components. It was designed with a dual cam mechanism shown in Figure 2. 10 for purpose of substituting for the function of anterior cruciate ligament (ACL) and PCL. It had the same issue with the PS design that although the medial-lateral stability had been improved because of the increased contact between the cam-post components, the wear also increased significantly. It appeared that wear severity was highly dependent on ligament balancing, because it was rarely an issue with a well-balanced knee. If the post was acting as a secondary stabilizer to coronal motion, it would wear out over time.[36]

Figure 2. 9 Fully conforming post-cam mechanism of posterior stabilizer [31]

Figure 2. 10 cruciate-substituting implant design [37]

As contrast to the PS component, cruciate-retaining (CR) designs do not have the cam-

post mechanism but to retain patient's posterior cruciate ligament if it is healthy enough to continue stabilizing the knee joint. Studies comparing a CR-TKR with intact PCL with a CR-TKR without PCL showed significant decline in kinematics in the design removing PCL.[36] There are also designs of bi-cruciate retaining which could help knee function and feel more like a non-replaced knee, but in most TKR surgeries, the ACL is resected for the issue of precisely placing implant component. In order to imitate the tibial rotation, ball-in-socket component was proposed by MicroPort® as EVOLUTION Medial-Pivot Knee System [38], to allow the lateral condylar rotation and in the meantime, allow the medial socket to replicate the stability of ACL, PCL and meniscus.

According to the function of tibial components, the designs can be divided into two groups: fixed and mobile bearing prostheses. These two designs have exactly the same components of the above designs except that the tibial insert of mobile bearing prostheses (see Figure 2. 11) can rotate inside the metal tibial tray. This is designed to allow a few greater degrees of rotation to the medial and lateral sides of patients' knee. Due to the better mobility, the knee joint motion requires the support and help of surrounding ligaments to maintain the joint stability, otherwise, the joint is more likely to dislocate. Although the mobile bearing prostheses were developed or evolved from the fixed counterpart, it was proved through clinical study [39] that there was no advantage of mobile bearing over fixed bearing. In addition, Lu et al. [40] concluded there was more wear in the bottom surface of the mobile bearing which interfaces with the tibial tray.

Figure 2. 11 Mobile-bearing tibial insert prostheses design [41]
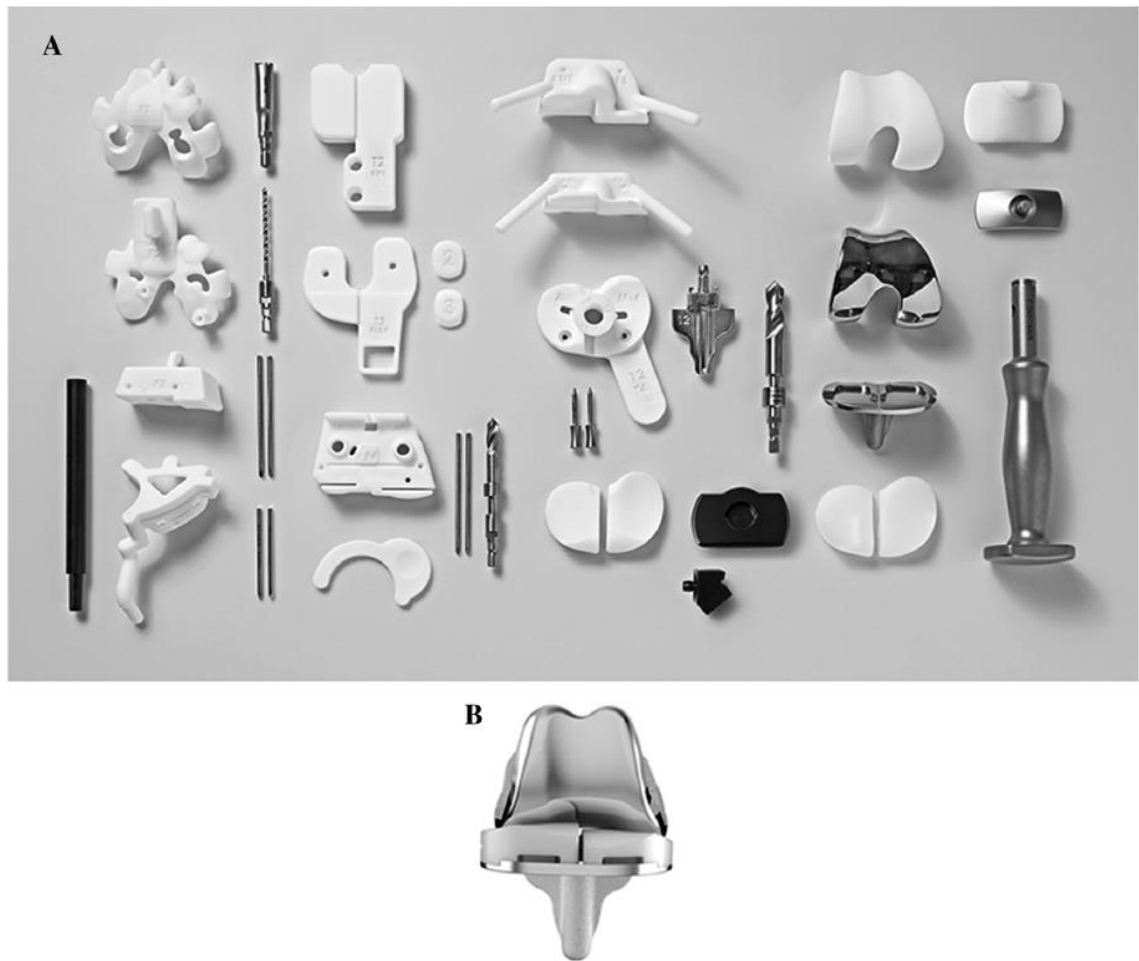
Figure 2. 12 A: Photograph of patient-specific cutting guides. B: Photograph of patient-specific implant [12]

Patil et al. [12] introduced a customised design of TKI shown in Figure 2. 12. Its femoral component was generated from three patient-specific J-curves that were extracted from medial condyle, lateral condyle and trochlear groove in the sagittal plane. Its tibial counterpart was then created based on the three J-curves of the patient's femoral condyles. The goal of this design is to maximise bony coverage and restore patient's knee kinematics by closely approximating patient's natural anatomy.

2.4 Mechanical and kinematic alignments of TKA

Total knee implants were placed on patients' knees based on two accepted principles: mechanical alignment and kinematic alignment. [42] In the mechanical alignment, the femoral and tibial components were installed in alignment with the femoral and tibial mechanical axes respectively. The femoral mechanical axis was defined by connecting

the femoral head centre and the intercondylar notch centre, while the tibial counterpart was determined by connecting the talus bone centre with the proximal tibial centre. Regarding the kinematic alignment, it was based on three fixed functional kinematic axes which were intended to dynamically describe the relative relationships between the femur and tibia and between the femur and patella. The primary axis was a transverse axis in the femur about which the tibia flexed and extended. It passed through the centre of a circle fit to the posterior femoral condyles. There was a second transverse axis in the femur about which the patella flexed and extended. It was parallel, proximal, and anterior to the primary transverse axis. The third axis was a longitudinal axis in the tibia about which the tibia internally and externally rotated on the femur. It was perpendicular to each of the two transverse axes in the femur. The mechanical alignment of TKA was used to make the knee joint loads evenly distributed on two femoral condyles through changing the knee joint line orientation angle which was defined by the angle between the knee joint line and the line parallel to the ground. By contrast, the kinematic alignment was implemented to keep patient's knee joint line orientation angle before the TKA surgery. Ji et al. [43] reported Kinematic alignment of TKA could align the knee joint line to horizontal line by investigating the standing subject knee joints. But its influence on the dynamic knee loading was unknown.

2.5 The Oxford knee rig and other knee testing systems

The Oxford knee rig (OKR) was designed for biomechanical testing of post-mortem human knee-joint specimens during simulated flexed-knee stance, such as riding a bicycle, rising from a chair, or climbing stairs. Zavatsky [44] demonstrated that the OKR allowed full spatial degrees of freedom (DOFs) of knee joints by using a mathematical analytic method and a criterion of general mobility for spatial linkages. But the further detailed knee joint motion trajectories were not calculated.

The first version of the OKR was built by O'Connor et al. [45] and used to study various knee implants. Refinements of the original OKR were made later to study the tibial rotation, contact force distribution between the medial and lateral compartments of the tibiofemoral joint, and the relationships between quadriceps force and other externally applied loads.[44] Several following knee simulator rigs were mainly developed based on the OKR.

The main components of the OKR are an 'ankle' assembly and a 'hip' assembly, as shown in Figure 2. 13. The ankle assembly has three sets of rotary bearings whose axes intersect at a fixed point which can be regarded as the centre of ankle joint. This assembly allows spherical movement of the tibia about the ankle centre. To be specific, the spherical movement is composed of flexion-extension (F-E), abduction-adduction (A-A), and internal-external (I-E) tibial rotations. The hip assembly has two sets of rotary bearings which allow femoral F-E and A-A rotations in relation to 'pelvis' component.

Varadarajan et al. [46] reviewed the commonly used the OKR and the robotic knee testing system in Figure 2. 13 validating that both experiments could replicate the femoral rollback and 'screw home' tibial rotation in healthy subjects, and the reduced femoral rollback and absence of 'screw home' motion in TKR patients. For the robotic knee testing system, the cadaver knee was mounted in an inverted position with the tibia attached to the robot arm through a six-axis load cell.
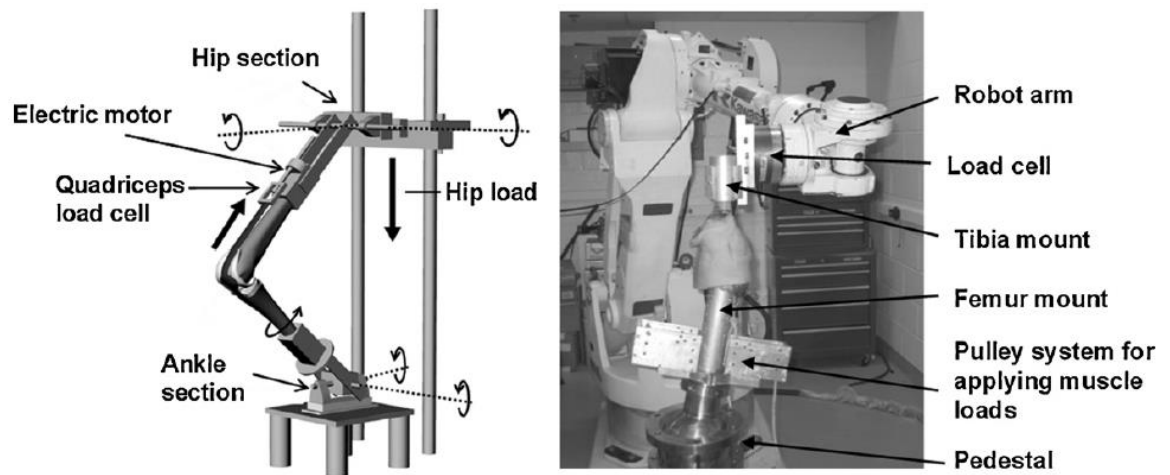
Figure 2. 13 Oxford knee rig and robotic knee testing system [46]
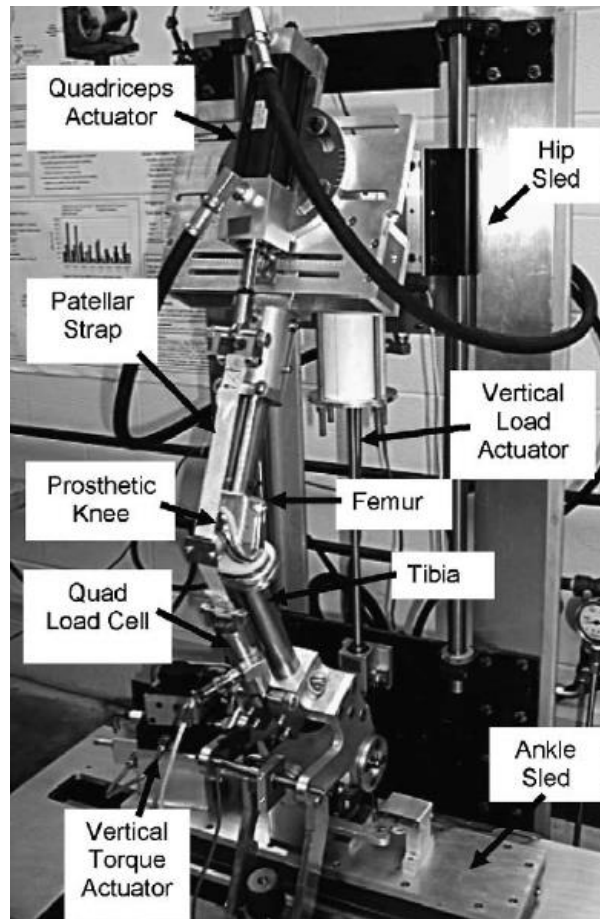
Figure 2. 14 Kansas Knee Simulator [47]

Based on the Purdue knee simulator [45, 46], the Kansas knee simulator (KKS) in Figure 2. 14 was built and studied in literature [50–54]. The KKS allowed different simulations of daily dynamic loading activities on either cadaveric knee specimens or total knee implants. The KKS was characterised of five axes of control that consisted of three loads (quadriceps load, vertical hip load and adduction-abduction translational ankle load) and two torques (ankle flexion moment and internal rotation moment), but the flexor muscles of the knee such as hamstring and gastrocnemius were neglected. The PID-control was integrated into the simulator to drive the quadriceps actuator and calculate the instantaneous quadriceps displacement in order to match the target hip flexion motion profile.

Baldwin et al. [53] used ABAQUS/Explicit to build a finite element (FE) model of the KKS that considered not only the specimen-specific bone and implanted components but also the quadriceps tendon and ligaments around the knee. The PID-control was implemented the way as the experimental KKS simulator. The simulation kinematic results were compared with the ones measured from the experiment, which showed good

agreement in both trends and magnitudes.
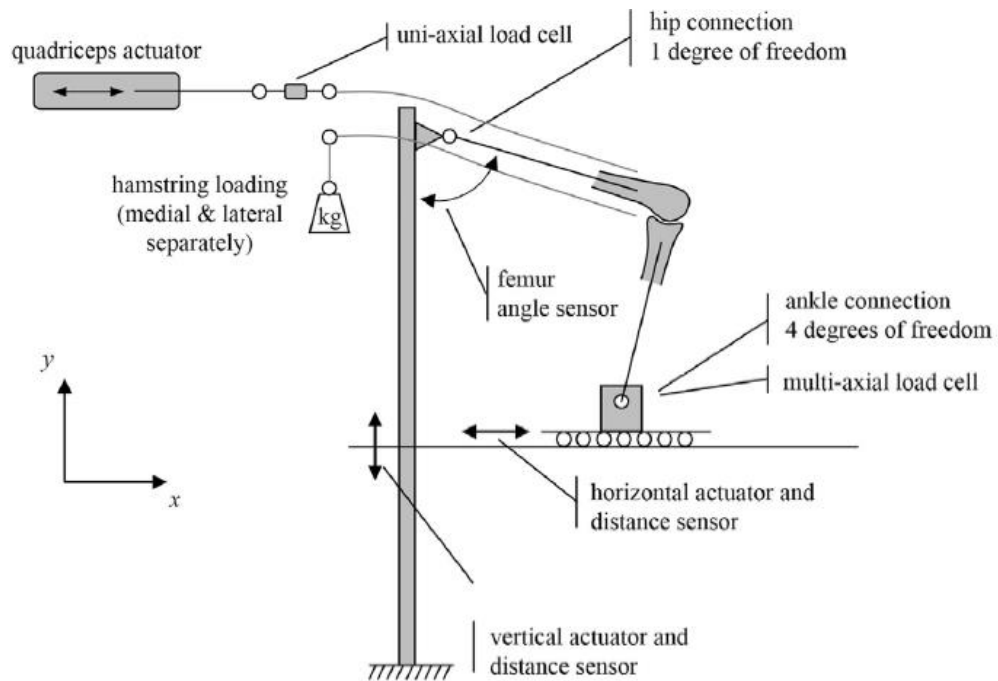
Figure 2. 15 Schematic representation of robotic knee simulator[55]

Verstraete [55] proposed an improved knee simulator shown in Figure 2. 15, which allowed the ankle joint to be controlled vertically and horizontally. Apart from the controllable ankle position, a continuously variable quadriceps force was applied by using a servomotor, while a constant hamstring force was adopted by attaching a constant mass to a pulley system. To simulate and control the knee simulator's motion and loading independently, two linear position sensors were installed near two actuators in the sagittal plane, while one multi-axial load cell was mounted at the 4-DOF ankle joint to give feedback of ankle force to the target quadriceps force. The actual quadriceps force could be also directly matched with its target value by using PID controllers.

Walker et al. [56] designed the Stanmore knee simulator for kinematics and wear testing of total knee replacements which is shown in Figure 2. 16. The simulator had five axes of controls which allowed inferior-superior translation, valgus-varus rotation and flexion-extension rotation of femoral component, and anterior-posterior translation, internal-external rotation of tibial component. Godest et al. [57] built an explicit FE model based on the Stanmore knee simulator to predict the kinematics and the internal stresses of total knee implants.
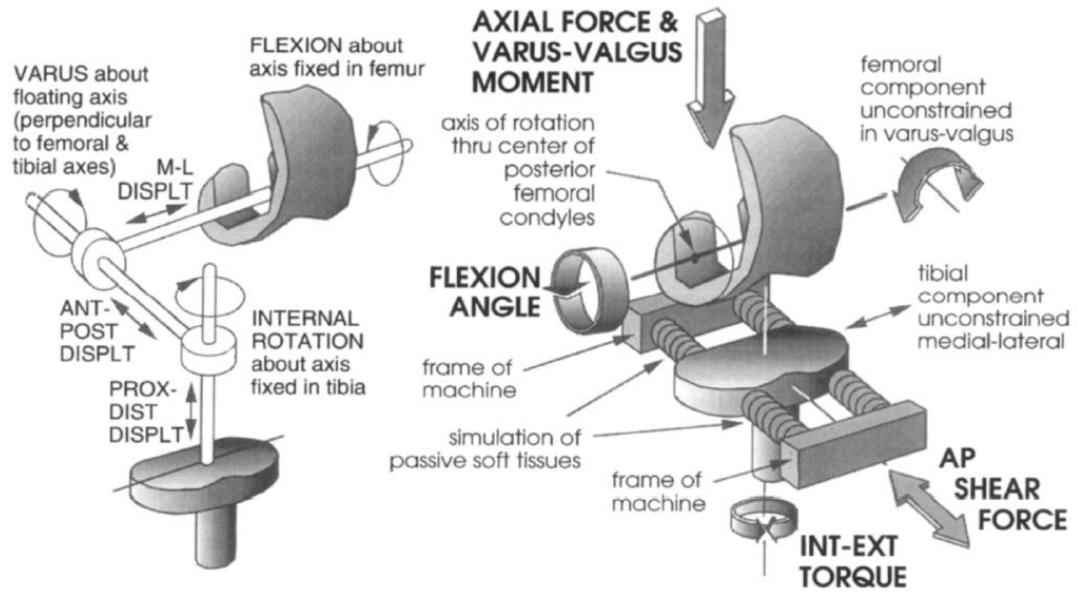
Figure 2. 16 The mechanical arrangement for the Stanmore knee simulator [56]
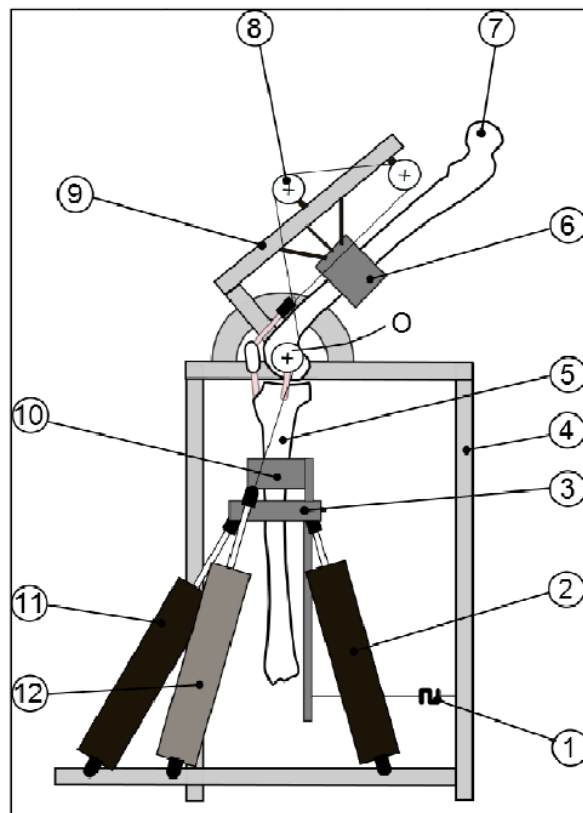
Figure 2. 17 Schematic representation of the test rig: (1) load cell; (2) and (11) actuators of the 6-6 Gough-Stewart manipulator for loading system; (3) platform of the 6-6 Gough-Stewart manipulator for loading system; (4) base; (5) tibia; (6) femur fixation system; (7) femur; (8) pulley of the system for extensor muscle simulation; (9) portal; (10) tibia fixation system; (12) actuator for extensor muscle simulation [58]

Forlani [58] designed a test rig shown in Figure 2. 17 for in-vitro evaluation of the knee joint behaviour. The femur was fixed on the portal (Figure 2. 17 (9)) which could only rotate about a fixed revolute axis. The revolute axis was chosen to be approximately coincident with the transepicondylar axis of the femur distal. The longitudinal axis of tibia was kept perpendicular to the portal revolute axis for calculating the femoral flexion angle. The quadriceps muscle force was adjusted by a control system to keep the joint balanced. The actuators of the 6-6 Gough-Stewart manipulator were used to apply external loads to the tibia bone for simulating the ground reaction forces, however, those loads were not applied on the distal of tibia but on its middle segment through the platform of actuators manipulator.

2.6 Boundary conditions used on knee joint simulations

Fitzpatrick et al. [59] predicted the internal-external (I-E) and anterior-posterior (A-P) joint loads by applying I-E and A-P joint motions that were measured from fluoroscopy to the FE model, and meanwhile, holding the tibiofemoral compressive forces constant at three different values respectively. The femoral component was fully constrained, while tibial counterpart was applied with 5-DOF loads and one F-E kinematics. In their another study [60], the femoral component was allowed to flex around the tibial counterpart by applying a combination of vertical hip force and hamstring muscle force. The quadriceps force was applied to extend the knee. In 2016, Fitzpatrick et al. [61] developed a computational model of a new 6-DOF joint simulator which allowed to apply loads or motions in any combination for all six DOFs of tibiofemoral joint. In that model, the F-E motion was applied in a kinematic function while the remaining five DOFs were load-driven, which was more complicated than the Stanmore simulator.

Bersini et al. [62] created a lower extremity dynamic model by modelling patella as a cylinder in contact with the femoral trochlear groove. An inextensible cord was used to connect patella with tibia. On the other side of patella, the quadriceps force was applied on a chain of three short cylinders which could get into contact with trochlear groove during squatting motion. The expression of quadriceps force was written as a sigmoid function of the knee joint angle from 200 to 900 N.

Guess et al. [47] built a computational model of the KKS with a structure representing a

prosthetic knee installed inside. A constant vertical load was applied at hip sled to push the hip joint downward to simulate squat motion, while the ankle joint was applied a sinusoidal vertical torque to test tibia A-A and I-E laxities. The ankle joint was allowed to translate mediolaterally by applying M-L ankle forces. The quadriceps muscle was represented by a patellar strap. An axial actuator connecting the patellar strap was used to control the hip flexion angle.

In the knee simulator proposed by Verstraete et al. [55], the hip joint was only allowed to flex, while the ankle joint was allowed to move in all six DOFs. Among these DOFs of ankle joint, the S-I and A-P translations were under the control of two linear electric servo actuators. All six DOFs of knee joint was considered, however, the knee flexion was also actively controlled by the above two actuators.

Shu et al. [63] combined the patient-specific musculoskeletal model with its FE models for predicting the TKR loads and stress distributions of one single gait after the TKR surgery. The muscle forces, ground reaction forces and lower extremity kinematics were imported into the FE model with supplement of the collateral ligaments and posterior cruciate ligament to calculate the dynamic tibiofemoral compressive forces.

2.7 Influence of knee joint geometry on the performance of TKR

Comparing to traditional knee implants mentioned in above sections, customised knee implant designs of which are closer to human's natural anatomical shape were much less studied, though extensive literature demonstrated the asymmetric nature of knee morphology, stability and motion.[10] Walker et al. [64] measured the motions of four PS designs and one experimental asymmetric PS design by using a Desktop Knee Machine which could apply combinations of forces representing a range of daily activities, and concluded that asymmetric design was able to produce the asymmetries in the motion of the anatomic knee.

Patil et al. [12] compared a customised knee implant from ConforMIS with a standard off-the-shelf CR knee implant from DePuy based on Oxford knee rig and found that patient-specific designed knee implant could produce kinematics that more closely resemble normal knee kinematics than standard off-the-shelf implants. The experiment result

showed that the difference from normal kinematics was lower for the customised design than the traditional one by comparing active femoral rollback, active tibiofemoral adduction, and passive varus–valgus laxity.

Zeller et al. [5] conducted an in-vivo kinematic analysis between the ConforMIS implant and a traditional design TKI by using fluoroscopic method. Same conclusion was drawn that the customised TKI could produce a kinematics more similar to a normal knee. It was also found that the customised design had better stability due to minimal condylar lift-off than the traditional design.

Willing and Kim [65] combined a rigid body TKR kinematics simulation model in software MSC ADAMS and a numerical optimization algorithm of sequential quadratic programming for designing optimum shapes of the femoral component and UHMWPE tibial insert. An objective function based on joint constraint and flexion range of motion was established with consideration of 14 design variables, which allowed the optimizer to search a large design space. The optimization iteration started from a symmetrically designed implant. Large improvement in the Anterior-posterior constraint at 0° flexion was obtained, as well as an increase in the flexion range of motion to 143 degree. The final design was asymmetric condyles which implied the necessity of customised asymmetric design.

Gerus et al. [66] investigated the influence of subject-specific geometry and knee joint kinematics on the tibiofemoral contact forces prediction utilising a calibrated EMG-driven neuromusculoskeletal model of the knee joint. They found using the subject-specific knee geometry could improve the accuracy of predicted medial contact forces, though using the subject-specific kinematics did not improve estimates of medial and lateral contact forces. Meanwhile, they also suggested that the EMG-driven approach could be used to predict muscle and joint forces without optimization after completing an optimization-based calibration process.

Pandit et al. [67] investigated the influence of component geometry and the adoption of PS cam-post mechanism via comparing the kinematics of a polyradial femur implant with that of a single radius design. Both designs are considered with and without a cam-post mechanism. It was found that neither of the TKR design kinematics were influenced by

cam-post mechanism, however, the surface geometry did determine the joint kinematics. Single-axis, single-radius femoral component performed much closer to normal knee patterns than polyradial femoral one in both tests of extension against gravity and set-up, even though both kinds of implants kinematics were still abnormal.

Clary et al. [68] studied the influence of TKR geometry on mid-flexion stability. The amplitude of anterior-posterior translation was found to be attenuated by replacing traditional dual-radius femoral components with a gradually reducing radius femur design. The dual-radius femoral component had an instantaneous transition from the distal to posterior radius. Additionally, it was demonstrated that the overall magnitude of the anterior slide was affected by the tibial conformity, with the greatest anterior slide occurring for the least conforming tibial insert.

Fitzpatrick et al. [69] evaluated the mechanics of the unresurfaced patella and compared with the natural and resurfaced patella conditions through building finite element models of the patellofemoral joint. The result showed that the compressive patellar bone strain in the unresurfaced conditions was higher than that in the resurfaced conditions in the knee flexion over 40°. The unresurfaced patella with the natural-shaped femoral implant showed smaller contact pressures than the same patella model with the off-the-shelf femoral components, but still it is much larger than that of the natural knee due to the harder femoral component surface.

Simpson et al. [70] studied the effect of tibial bearing congruency, thickness and alignment on the stresses in the unicompartmental knee replacements by inserting four different unicompartmental knee replacement implant designs into a validated finite element model of a proximal tibia. The four implants include the fully-congruent model with a spherical femoral component articulating on a spherical and mobile tibial bearing, the partially-congruent model with a poly-radial femoral component articulating on a fixed concave tibial bearing, the non-congruent-metal-backed model and the non-congruent-all-polyethylene model. The results showed only the fully-congruent model experienced the peak von Mises and contact stresses below the lower fatigue limit for the polyethylene during the step-up activity. The highest polyethylene contact stresses were observed in the partially-congruent and non-congruent-metal-backed models. These two models experienced approximately three times the lower fatigue limit [70] (17 MPa) of the

polyethylene. The fully-congruent design could be markedly thinner without approaching the material failure limit. It has a greater potential to preserve bone stock and is less likely to fail mechanically.

Rawlinson and Bartel [71] analysed three tibial two-dimensional configurations of flat-on-flat, curved-on-flat, and curved-on-curved geometries by using the FE method with nonlinear material properties. Although the conformity of the articular surfaces has a large effect on the resultant stresses, the perfect conformity arising from flat contact did not reduce the contact stresses in the UHMWPE component. The curved-on-curved geometry was found to produce the lowest von Mises stress and strain among the three configurations, which, to some extent, implied the significance of conformity between femoral and tibial bearing surfaces. However, allowing for the relative motions between those two components, tibial bearing geometry should be designed based on the kinematic relationship between the articular bones.

Walker [72] proposed a design method for TKI which could generate a range of total knee implant surfaces, and potentially helped restore the arthritic knee to more normal function. The method was to build the tibial bearing surface by smoothening the lower position surfaces of multiple rotating positions of the femoral component. To provide motion guidance for the femoral component on the tibial bearing in the absence of the cruciate ligaments, two types of design were generated. One was created with a post-cam mechanism by reducing the depth of the patella groove on the distal and posterior parts of the femoral component, while another design used the femoral condylar surfaces by moving the dwell point of the lateral femoral surface on the tibial surface inwards or outwards with the knee flexions.

2.8 Customised modelling by feature identification of bone contour

Harrysson et al. [73] customised both the articulating surface and the bone-implant interface based on a computed tomography (CT) scan of the patient's joint. After obtaining 3D model from Mimics (Materialise, Leuven, Belgium), a software named Geomagic Studio V7.0 (Raindrop Geomagic, Triangle Park, NC) was used to convert the stl-file format into a NURBS (Non-Uniform Rational B-Spline) format whose surfaces can be exported as a solid CAD model using a STEP-file format. Finally, the

proposed customised implant design was done using Pro/ENGINEER (PTC, Needham, MA) creating a set of spline curves along the interface surface in a radial pattern, and a single spline to connect all curves in a central plane between the condyles. A swept-blend command was used to create the smooth articulating surface. Additional cuts and fillets were added to provide an implant with smooth surfaces and edges. Through applying FE analysis, a customised implant with a free-form bone interface could provide a more even stress distribution on the bone interface than the traditional femoral components.

Li et al. [74] developed a computational framework including pattern recognition algorithm for sectioning the sagittal view condyle profiles, a least-squares algorithm for fitting and analysing the profiles, and an optimisation algorithm for establishing a unified sagittal plane. For the least-squares algorithm, they chose to use a parametric-form ellipse to fit the identified articulating portion of a condyle profile. However, their work was limited by only using the sagittal contours of the distal femur.

Sholukha et al. [75] used multiple regression method based on quadric surface fitting to approximate the position of its morphological joint centres and the shape morphology. Their study results showed that this type of approximation was enough to reconstruct typical bone convex and concave forms with good accuracy for most anatomical features.

Cerveri et al. [76] developed a computer algorithm which could automatically compute the proximal femur morphological parameters by processing the mesh surface of the femur. Numerical methods such as least-squares cylinder fitting, least-squares sphere fitting and minimal area of the cross section by evolutionary optimization were utilised to identify the axis of the shaft of femur, head surface and centre and femur neck axis and radius respectively. The final results of computed parameters were validated in well agreement with the manually identified parameters in the original CT images by medical experts.

For automating the design of resection guides specific to patient anatomy in knee replacement surgery, Cerveri et al. [77] extracted the inter-condylar fossa or trochlear groove from the distal femur surface, synthesized the inter-condylar fossa with a hyperbolic paraboloid by exploiting an algorithm of curvature mean-shifted, and finally identified the whiteside line as the main saddle direction. The whiteside line is defined

as the line connecting the deepest part of the anterior patellar groove to the centre of the posterior intercondylar notch and is commonly adopted as a reference line to determinate the knee flexion–extension axis and help position the femoral component.

2.9 Modelling of human knee joint ligaments

Human ligaments are the important soft tissue to stabilise joints. They are also essential elements for FE dynamic analysis. The ligament mathematic model was often established as elastic spring for the purpose of saving computational cost. And it was also regarded as the most efficient computational method. The most popular spring model for ligaments is the force-displacement curve which was first introduced by Wismans [78] and Blankevoort et al. [76, 77]. In that model, the ligament was thought to have a non-linear toe region of the relationship between its force and displacement. It is caused by the initial crimping of the ligament fibres, and once all the fibres become taut, it will behave as a linear spring.

In some studies, ligaments were modelled as three-dimensional constitutive elements [81]. Through this method, the wrapping effect of ligaments over the bones can be included. However, it highly demands the computational resource and cost. Besides, the mathematical description of the material properties in the continuum material is still difficult to know. Beidokhti et al. [82] studied the effect of two ways of ligament modelling on the accuracy, and concluded that the continuum two-dimensional (2D) fibre-reinforced membrane model could produce more accurate contact outcomes. However, when the joint kinematics is the major concern, the spring ligament model could provide not only faster solution but also acceptable result. Baldwin et al. [49, 50] built the ligaments of knee joint as capsular soft tissue structures for the knee simulations. The penalty-based contact was defined between all the soft tissue structures and bones or articular surfaces for wrapping. Fitzpatrick et al. [60] also used to build soft-tissue such as medial and lateral collateral ligaments as 2D membrane model with ligament pre-strain and stiffness.

2.10 OpenSim applications in knee joint biomechanics

In the aforementioned in-vitro knee test rigs, there is a common issue that neither close-to-physiological muscle forces nor hip and ankle joint forces corresponding to the

practical ground reaction forces were applied. However, in reality, muscle forces do play important role in joint motion and joint stability. Medium to high quadriceps, hamstrings, and gastrocnemius activities were reported during squatting.[83] Although recruiting only quadriceps or hamstrings in the aforementioned in-vitro experiments or simulations could reduce the complexity of operation and save cost of computation, it doesn't mean that other leg muscles such as gastrocnemius and anterior tibialis are not or less important. Gastrocnemius muscle is an important flexor muscle of knee joint, and anterior tibialis is an important flexor muscle of ankle joint. Both effectively influence not only the rotations but also the translation of knee joint. Neglecting the effect of these muscles or the effect of muscle coordination could result in the knee joint simulations less consistent with that in a realistic physiological and physical conditions. Therefore, it is very necessary to apply the muscle forces for the analysis of kinematics and kinetics of skeletal and numerical models.
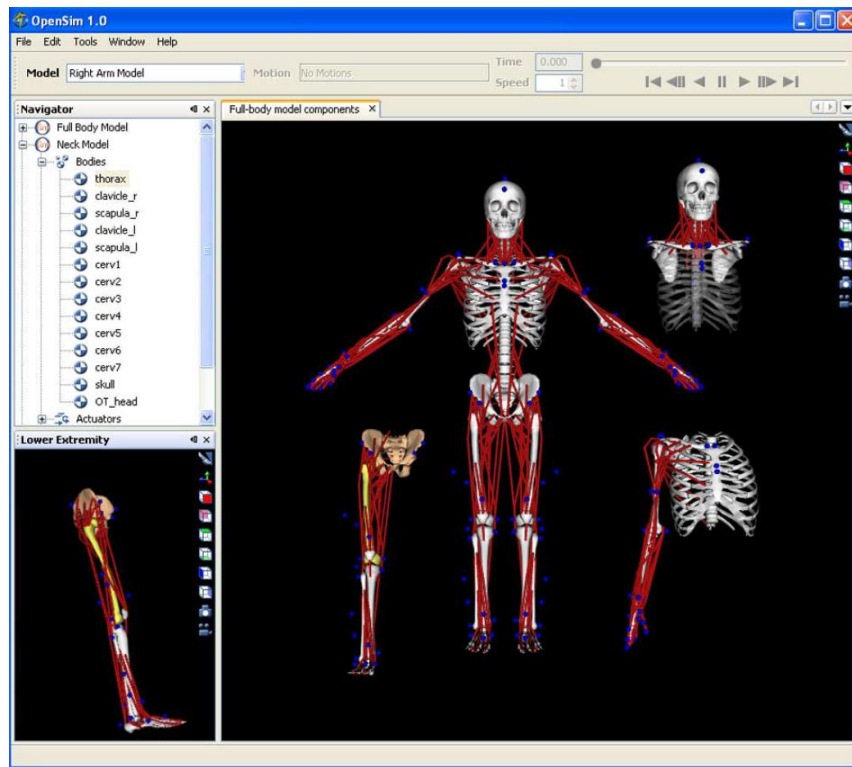
Figure 2. 18 OpenSim Graphic User Interface [84]

To solve muscle and skeleton coupled problems, Delp et al. [85–87] firstly introduced the software package SIMM which enabled users to create or edit musculoskeletal models and even simulate movements such as walking, cycling, running and stair climbing. Later in 2007, Delp et al. [84] introduced the biomechanical simulation software OpenSim

which allowed calculation of muscle excitation for helping produce coordinated movement. Through the user-friendly graphic user interface shown in Figure 2. 18, users are allowed to edit muscles shown in red lines and plot muscle variables of interest such as muscle activation, lengths, and active or passive forces. Models of various musculoskeletal structures, including the lower extremity, upper extremity and neck, can be loaded, viewed and analysed. The blue spheres are the virtual markers which are the reference points. Each body segment's kinematic results such as displacement, velocity and acceleration can be calculated based on the imported marker data which are collected through motion capture experiment. The experimental markers can be attached to a specific subject of interest for joint motion and load analyses.

As can be seen in Figure 2. 19, for a typical simulation process of OpenSim, a generic musculoskeletal model is normally loaded from the OpenSim musculoskeletal model database into the software interface. In the first step, the measured experimental kinematic data, i.e., x-y-z trajectories of marker data are used to scale the musculoskeletal model to best match the dimensions of the subject. In the second step, an inverse kinematics (IK) problem is solved to find the model joint angles that best reproduce the experimental kinematic data. Subsequently, the residual reduction algorithm (RRA) is implemented to refine the model kinematics so that they are more dynamically consistent with the experimental reaction forces and moments. Lastly, the computed muscle control (CMC) algorithm is applied to find a set of muscle excitations. As an input, those muscle excitations can be further imported into the same scaled musculoskeletal model to generate a forward dynamic simulation that closely tracks and reproduces the subject motion.
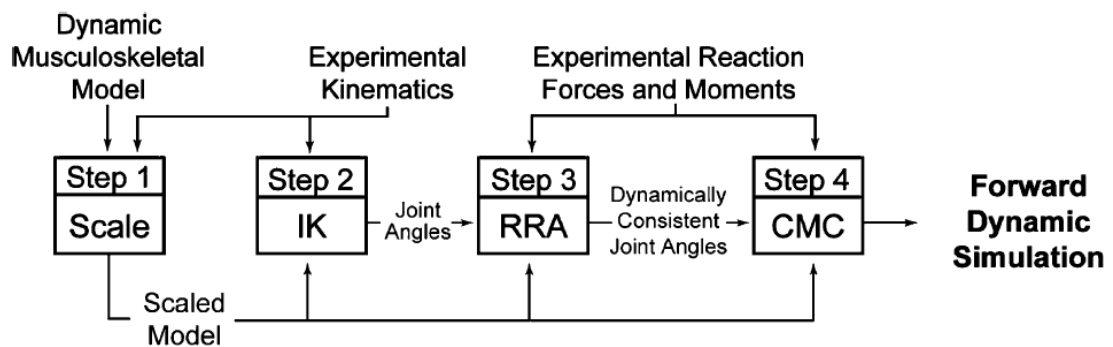
Figure 2. 19 Processes of generating a patient-specific muscle-driven simulation of motion using OpenSim [84]

As an example, in the same paper [84], dynamic simulations of individuals with pathological gait were performed to examine the causes of their abnormal walking pattern and explore the biomechanical effects of treatment of botulinum toxin injection and Rectus femoris transfer.

Sherman et al. [88] presented the advantages of OpenSim over other mechanical software. They pointed out that the analogy between engineering mechanical systems and evolved biomechanical systems was imprecise, and the multibody mechanics tools designed for engineered systems could be difficult to be applied to the dynamics studies of complex biological structures. For example, biomechanical joints typically do not perform simple rotations about fixed axes and may comprise several moving parts; contact between soft deformable biomaterials may involve significant deformation; redundant actuation of joints is common; data needed for parameterisation are not directly measurable; and available measurements tend to contain large errors and inconsistencies. In the context of whole-body musculoskeletal mechanics, segment mass properties and muscle path geometry are hard to measure, while body segment kinematics (i.e., joint angles) estimated from surface markers are inconsistent with accelerations determined from external force measurements (i.e., ground reaction forces). Because of these issues, concepts that are simple to apply to engineered systems, such as "generalized coordinate" or "moment arm", become difficult to define precisely in a biomechanical context.

OpenSim is conceived primarily as a reliable tool for use in biomedical research, rather than as a vehicle for multibody dynamics research.[88] Its muscle-actuated dynamic simulations can complement experimental and physical approaches allowing us to establish important variables or identify cause-and-effect relationships and then give insights into muscle function and its contributions to movement.

In recent years, OpenSim has been widely used in hundreds of biomechanics laboratories around the world to study movement due to its free and widely accessible resources. Besides, the OpenSim online community (simtk.org) allows developers to access or contribute new features or tools which were developed in previous studies. The wide range of studies with OpenSim includes the analysis of walking dynamics, studies of sports performance, simulations of surgical procedures, analysis of joint loads,

evaluation of medical devices, and animation of animal movement.

Reinbolt et al. [89] utilized the computed muscle control, one functional module tool of OpenSim, to identify new movements as an athletic training tool to reduce injury risk, and establish relationships among posture, muscle forces, and ground reaction forces.

Mansouri and Misagh [90] combined the OpenSim with the MATLAB/Simulink . By taking the advantage of OpenSim in the cost-effective dynamic musculoskeletal simulation, and MATLAB/Simulink in the rapid model-based design control systems and powerful numerical method, a new interface was developed between the two software tools to successfully simulate the pole balancing on an upper extremity model hand.

Gerus et al. [66] established four different OpenSim models combining generic and healthy subject-specific knee joint geometries and kinematics. A conclusion was drawn that using the subject-specific knee geometry could improve the accuracy of predicted medial contact forces on the knee joint.
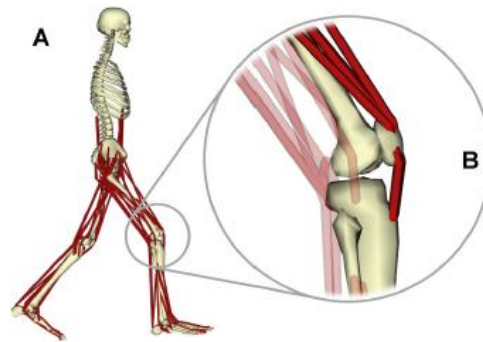
Figure 2. 20 Musculoskeletal model of the human legs and torso [91]

DeMers et al. [91] developed a subject-specific musculoskeletal model simulating the subject walking with an instrumented knee implant to study the effect of varied muscle coordination on the tibiofemoral contact forces. An optimisation framework was developed to calculate individual muscle forces and tibiofemoral forces for each trial. The coordination of muscles was varied to determine its influence on tibiofemoral force. They found that peak tibiofemoral forces during late stance could be reduced by increasing the activation of the gluteus medius, uniarticular hip flexors, and soleus, and

decreasing the activation of the gastrocnemius and rectus femoris. These results validated that the tibiofemoral forces were sensitive to activations of some lower limb muscles such as gluteus medius, gastrocnemius, and rectus femoris. In his model, the ligaments were all neglected, and the quadriceps forces were transmitted through the patella to the tibia bone without defining patellofemoral or tibiofemoral contact pairs.

Steele et al. [92] used OpenSim to examine the relationship between muscle forces and compressive tibiofemoral force with the increasing change of knee flexion in the crouch gait among three unimpaired children and nine children with cerebral palsy who walked with varying degrees of knee flexion. Their research found mild crouch gait (minimum knee flexion 20–35 degree) did not produce too much different peak compressive tibiofemoral forces between two groups, while severe crouch gait (minimum knee flexion > 50 degree) increased the peak force to greater than 6 times body-weight, more than double the load experienced during the unimpaired gait. It was explained that that increase in compressive tibiofemoral force was primarily due to increases in quadriceps force during crouch gait, which increased quadratically with average stance phase knee flexion. Therefore, it was concluded that the increased quadriceps force contributed to larger tibiofemoral and patellofemoral loading which might contribute to knee pain in individuals with crouch gait.

Kim et al. [93] predicted knee muscle forces during walking movement by comparing computed tibiofemoral contact forces with the in-vivo measurements obtained from an instrumented knee implant. Subsequently, the predicted knee muscle forces were input into a 3D knee implant contact model to calculate tibial contact forces. The calculation results of the model medial, lateral, and total tibial contact forces were found to be in close agreement with experimental measurements for walking at slow, normal, and fast speeds. Additionally, the muscle coordination predicted by the model was well consistent with EMG measurements reported for normal walking.

Fregly et al. [94] designed a modified gait motion for a specific patient with knee osteoarthritis. A dynamic optimisation of a patient-specific, full-body gait model was used. Through the optimization, a "medial thrust" gait pattern was predicted, which could reduce the first adduction torque peak between 32% and 54% and the second peak between 34% and 56%. The magnitude of the first adduction torque peak in particular

was strongly associated with knee osteoarthritis progression. At the same time, the new motion could also help slightly increase leg flexion and pelvis axial rotation, and decrease pelvis obliquity.

Schache et al. [95] studied the effect of five reference frames on the interpretation of how gait modification altered the external knee adduction moment. The research found that both gait modification and selected reference frame could influence the calculated knee adduction moment. Furthermore, these two effects were interactive. The magnitude of the changes in the knee adduction moment was produced by toe out and medial thrust gait which highly depended on the selected reference frame.

Walter et al. [96] studied whether reducing knee adduction moment could accurately predict corresponding decreases in medial contact force. The simulation was based on the in-vivo gait data collected from a specific subject with an instrumented knee implant. The external knee adduction moment has been identified as a surrogate measure for medial contact force during gait. An abnormally large peak value is linked to the increased pain and rate of disease progression. It was found that reductions in the second peak and angular impulse of the knee adduction moment corresponded to reductions in the second peak and impulse of medial contact force. Calculated reductions in both knee adduction moment peaks were highly sensitive to rotation of the shank reference frame about the superior-inferior axis of the shank.

All these three papers [94–96] showed that the patient-specific gait modification is effective in reducing peak frontal plane knee moment and also indicated that different motion pattern could affect or determine the internal loads in the joints and vice versa.

2.11 Conclusion

The customised total knee implant has been reported to enable patient to have a larger range of motion than the traditional design. However, the current customised design still cannot fully restore kinematics of patient's knee joint. Therefore, a new customised design that is closer to the natural anatomy of knee joint will be attempted and simulated for investigating the possibility of fully restoring knee kinematics.

To assess the total knee implant, the commonly used knee simulators usually simplified the effect of muscle forces by merely applying an experimental quadriceps muscle force in order to meet the prescribed hip joint flexion angles. The effects of body weight and inertial motion of the lower limb were also ignored. Because many other muscle forces and practical ground reaction forces were neglected in those knee simulators, the hip and ankle joint were usually applied with smaller reaction forces than the physiological ones.

OpenSim is a widely-used biomechanical simulation software which allows researchers to analyse muscle forces and joint reaction forces under particular movement scenarios by using the captured motion of a subject. Therefore, OpenSim will be used to obtain lower limb muscle forces and ankle joint reaction forces that are closer-to-physiological than the previously applied counterparts. Lastly, those muscle forces and ankle joint loads will be considered for their effect on the kinematics and kinetics of total knee implants, which will hopefully make the simulation much closer to the physiological and physical circumstance.

Chapter 3

Design of customised total knee implants using ANSYS Mechanical APDL

3.1 Introduction

Total knee replacement (TKR) or total knee arthroplasty (TKA) has been implemented with various implants of different designs for several decades. Most knee implants were standardised with limited size types and two parallel arc-shaped condylar surfaces. The condylar guidance tracks in sagittal plane were normally simplified with single, dual or gradually changing multi-radii arcs. Due to the limitation of available standardised TKR types and sizes, the retained bone of patients' knee joints could not completely match the TKR implants. When the femoral component overhang exceeds 3 mm over the femoral bone, it will double the odds of clinically important knee residual pain two years after TKR surgery.[8] It was reported in studies [4, 6, 94, 95] that the residual pain was one of the two leading reasons for patients' dissatisfaction after treatments. Another reason was the functional limitation which might be caused by the geometric shapes of traditional implants. Reviewing the functionality of total knee implants which were traditionally designed, Bonnefoy-Mazure et al. [99] and Rahman et al. [100] studied the knee kinematics after 3 and 12 months of TKR respectively and concluded that the knee function was not fully restored in terms of knee range of motions despite some improvements. The same conclusions were drawn by other researchers [101–103].

Comparing to traditional knee implants, designs of customised total knee implants (CTKIs) were much less studied, though extensive literature demonstrated the asymmetric nature of knee morphology, stability and motion.[10] Walker et al. [64] measured the motions of four posterior-stabilised (PS) designs and one experimental asymmetric PS design by using a desktop knee machine, and concluded that asymmetric design was able to produce the asymmetries in the motion of the anatomic knee. Patil et al. [12] compared a CTKI designed by the joint implant company ConforMIS with a standard off-the-shelf cruciate-retaining (CR) design by DePuy based on Oxford knee rig and found that patient-specific designed knee implant could produce kinematics that is much closer to normal knee kinematics than the standard off-the-shelf implants.

Considering the potential advantage of the customised asymmetric knee implants and the lack of detailed design method for customised implants in current studies, in this chapter, a design method for the customised TKR was proposed using ANSYS Mechanical APDL (ANSYS Programming Design Language). It could reduce the sizing compromise and address the component overhang issue [8] , and on the other hand, we hypothesized that mimicking the natural shape of knee could help a patient move more naturally.

Three-dimensional (3D) knee joint model was firstly built from computed tomography (CT) images of the subject model JW (mass: 66.7 kg, height 1.68 m) which was made available for the 4th Grand Challenge Competition to Predict In Vivo Knee Loads [13, 14]. The 3D modelling was performed using 3D Slicer [104] (available from http://www.slicer.org) which is an open source software platform for medical image processing and 3D visualization. After smoothening, surface simplifying and solidifying the model using MeshLab [105] (ISTI - CNR, Italy), a customised TKR that is analogous to natural geometric knee joint was created through methods such as key feature point recognitions, least-squares curve fitting algorithms and surface regeneration in ANSYS Mechanical APDL 18.2 (ANSYS, Inc., Pennsylvania, USA).

3.2 Building 3D models from CT images

A number of 3D geometric models (femur cortical bone, femur cancellous bone, tibia cortical bone, tibia cancellous bone and patella bone) were built from a set of accessible CT images by using 3D Slicer shown in Figure 3. 1. However, some problems occurred during further model processing. Firstly, these models can only be saved in the STL file format which describes only the surface geometry of an object. Secondly, many small surface elements were produced, which may cause problems when geometric Boolean operation is required on the solid models, for example, cutting femur and tibia bones for fitting the corresponding implants. Thirdly, some surfaces might either intersect with or separate from other ones as shown in Figure 3. 2. The areas in the red ellipses show the open gaps caused by the error of filling voids in each layer of CT images, and those gaps are not appropriate for the conversion into a solid body. Therefore, surface remeshing, simplification and reconstruction need to be done before conversion into the solid body.

Figure 3. 1 Graphical user interface of 3D Slicer

(a) the superior-inferior CT section; (b) 3D model built from a series of CT images in the rest of windows; (c) the medial-lateral CT section; (d) the anterior-posterior CT section; different colours in the CT images denote different segments (e.g. femur and tibia) or types (e.g. cancellous and cortical) of bones
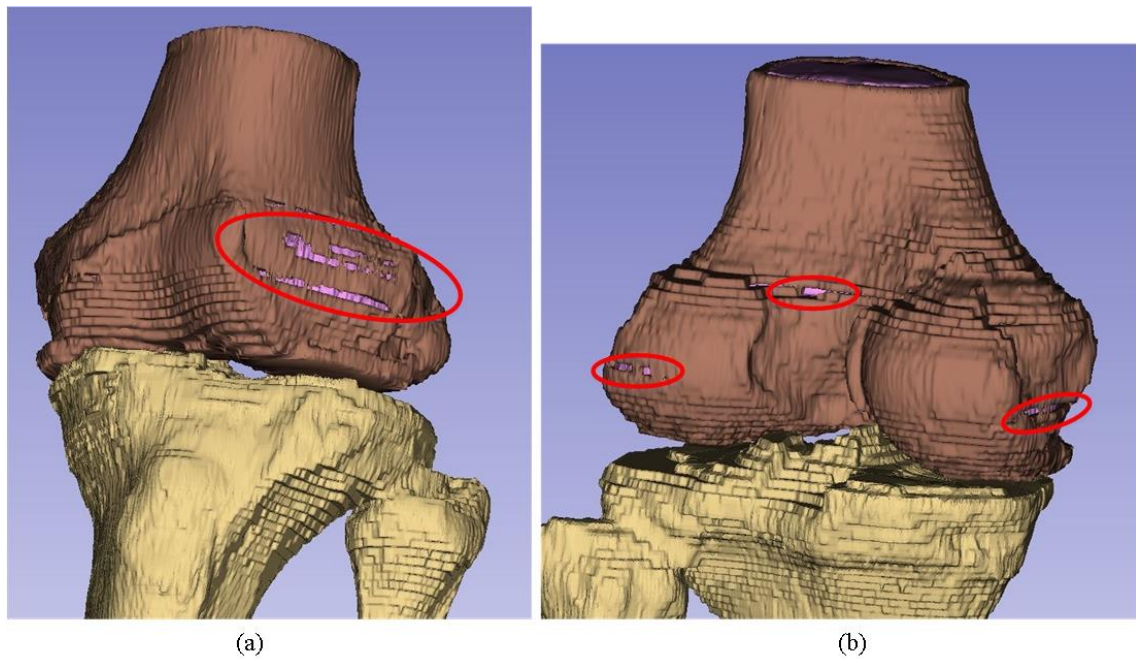
Figure 3. 2 Gaps in the 3D Slicer femur model in the (a) anterior view and (b) posterior view of knee joint

3.3 Repairing 3D Slicer model
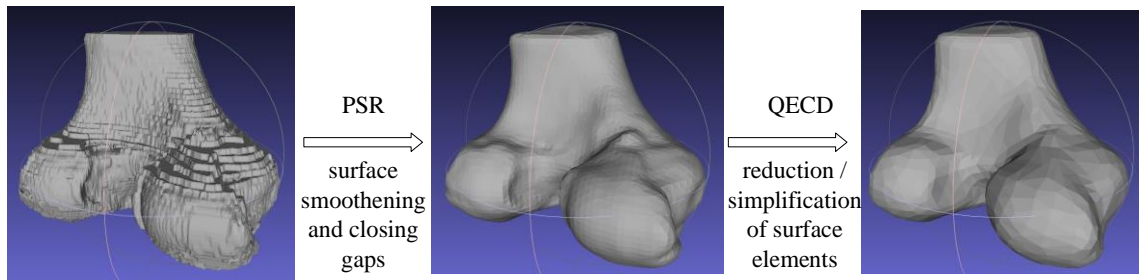
Figure 3. 3 Reconstruction and simplification of 3D Slicer femur model in MeshLab

The 3D mesh processing software MeshLab [105] (ISTI - CNR, Italy) was used to make body surface smooth, surface closed and simplified. Among various remeshing, simplification and reconstruction methods, the Poisson surface reconstruction (PSR) was used for smoothening the original slicer models, while the quadric edge collapse decimation (QECD) helped to reduce the amount of surface elements allowing for finite element meshes and calculations (see Figure 3. 3). Subsequently, a solid 3D model with several segments was obtained and saved in IGES file format using the open source software FreeCAD [106] (available from https://www.freecadweb.org/).

3.4 Creating a customised knee implant

3.4.1 Creating the femoral component

Based on the fact that normally the patients' knee condyle surfaces have been worn out, and the natural condylar surfaces lack easy-to-recognize characteristics but consist of many random irregular and rough small surfaces as shown in the post-processed femur model in Figure 3. 3, several steps have been performed to acquire smooth-surfaced, close-to-anatomy TKR components. As can be seen in Figure 3. 4, the cortical bones of the femur and tibia were imported into ANSYS for implant design. The ANSYS Mechanical APDL component was used to facilitate the parametric identification and articulation reconstruction.
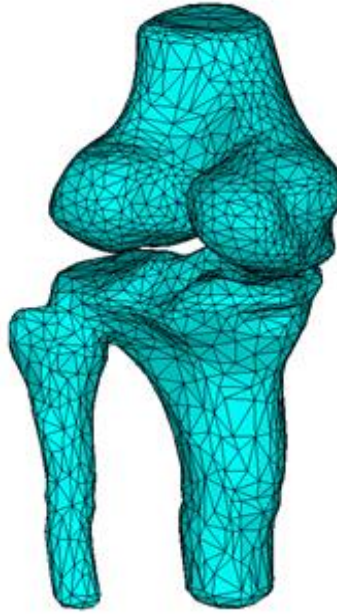
Figure 3. 4 Three-dimensional solid model of the femur and tibia bones
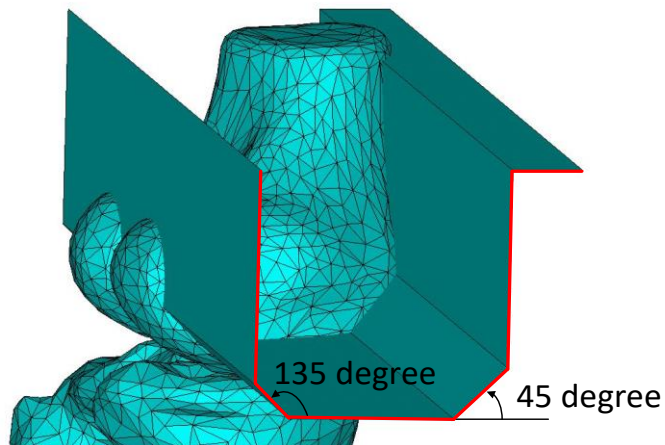
Figure 3. 5 Resection surfaces for removing unwanted bones

Step 1

The resection surfaces were defined in Figure 3. 5 to remove unwanted parts on the distal femur that required replacement.

Step 2

Surface meshing was applied on the surfaces of the removed distal femoral bone. The purpose of surface meshing is to facilitate the identification and selection of the geometric information of the condyles and the patellar groove which are essential for the customised design of implant. Through the node cloud which was produced by the

surface mesh tool and displayed in Figure 3. 6, the coordinates of each node could be easily extracted to create geometric features of interest.

Figure 3. 6 Node cloud of resected femoral distal bone

Step 3
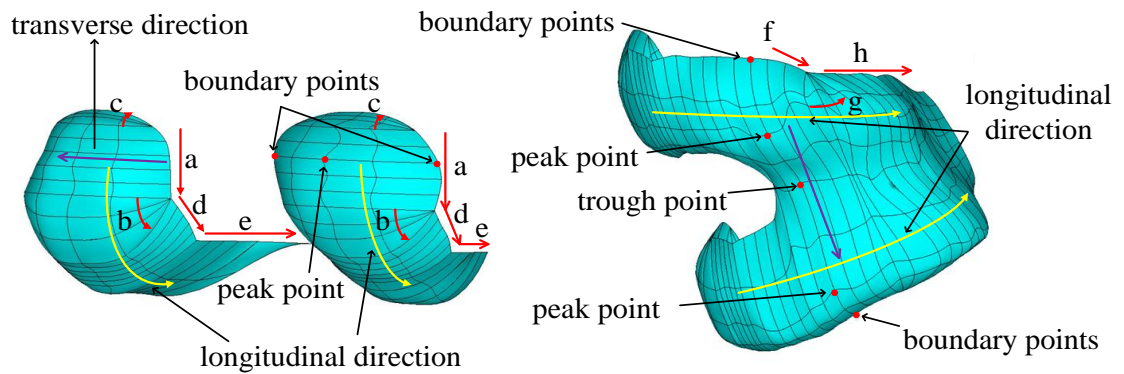
Figure 3. 7 Sequence of layer scanning

a, d, e, f and h: translational scanning; b, c and g: rotational scanning

Layer scanning was adopted to capture the features of two condyles and one patellar groove. It was performed in the sequence shown in Figure 3. 7. The scanning layer was always perpendicular to the edges at the two ends of the resection surfaces in Figure 3. 5. For the posterior part of the condyles, the layer scanning started horizontally from the location near the tip of the condyles down to the first corner of the resection edges. Then the scanning layer rotated 90 degrees around the two end points on this corner to the vertical position. Similarly, a rotation motion was performed from the starting layer on the top to the vertical position which is coincident with the component installation surface. Subsequently the cross sections in the scanning segment *d* were vertically scanned to the next corner point, then continue to the point where two separated condyles meet the

trochlear groove. Five layers were selected in the first segment, three in the following two rotation transition segments (*b* and *c*), and five in the last two segments respectively. Two boundary nodes, one peak node and two mid-nodes between the peak and the boundary nodes were selected in each scanned layer of each condyle and then these nodes' coordinates were further used to create key points (KPs) which are the most fundamental entity for building lines, areas and volumes in ANSYS mechanical APDL. The same method was applied to the remaining part of the distal femur with two boundary nodes, two peak nodes, one trough node and four mid-nodes in each layer.

Step 4

As can be seen in Figure 3. 7, the created KPs had been connected in the transverse (purple line, scanning layer) and longitudinal (yellow curve, scanning motion) directions with the method of cubic spline interpolation to ensure the continuity and smoothness of curves. However, the changing rate of surface curvatures of the two adjacent areas was not continuous, which resulted in rough surfaces. Therefore, a least-squares method of curve fittings was used to address the issue of irregular changing of curvatures of longitudinal curves (the ones in the longitudinal direction in Figure 3. 7).
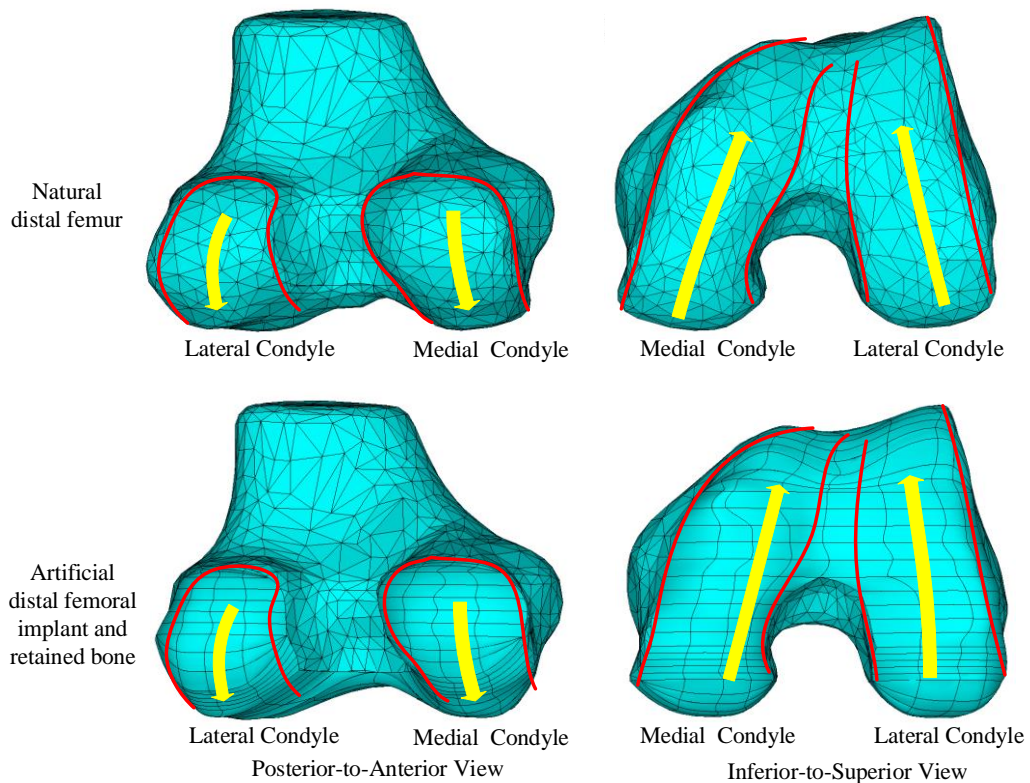
Figure 3. 8 Changing trend of two condyles in both natural distal femur and femoral implant

Since the changing pattern of each condyle which can be seen in Figure 3. 8 is different in the Posterior-to-Anterior View and the Inferior-to-Superior View, it is difficult to fit each column of KPs in the longitudinal direction into one plane. Then, the curve fitting was applied to each segment in each condyle respectively. For the continuity and smooth transition between two segments, the tangential direction at end KP of the first fitted curve segment (the part in the Posterior-to-Anterior View) was calculated and used for the next curve fitting function.

Several fitting curves (circle, sphere, quadratic curve, cubic curve) have been explored, but the ellipse curve fitting [107] was found to be the best to envelop the nodes on a particular cross section of the condyle in the longitudinal direction. The nodes were those produced by the previous surface meshing on the natural distal femur in Step 2. The least-squares equation is given in Eq. 3-1 to solve the expression function of a certain ellipse shape, and then input the two coordinates of each KP into the function to get the precise particular location on the fitted ellipse curve. The reason why the rest of the KP coordinate values (z_i) were not taken into account in Eq. 3-1 is that those KPs were first projected onto a fitted plane which was determined by three points averaged from the segmented KPs.

$$\mathcal{E} = \sum_{i=0}^{n}(x_i^2 + \mathrm{B}x_iy_i + Cy_i^2 + Dx_i + Ey_i + F)^2 \qquad (3\text{-}1)$$

$\mathcal{E}$ is the sum of the squares of the distance error from the point (x_i, y_i) to the curve: $x^2 + Bxy + Cy^2 + Dx + Ey + F = 0$ in a plane which is determined by the KPs that need curve fitting in the longitudinal direction. In order to make $\mathcal{E}$ the least, based on the extremum principle, the condition Eq. 3-5 needs to be satisfied. Then a system of linear algebraic equations can be obtained. Combining the boundary conditions and the Gaussian elimination method, the unknown parameter vector (B C D E F) can be solved and simultaneously, the expression function of the fitted ellipse can be determined as well.

$$x_0^2 + \mathrm{B}x_0y_0 + Cy_0^2 + Dx_0 + Ey_0 + F = 0 \qquad (3\text{-}2)$$

$$2x_0 + \mathrm{B}(y_0 + x_0y_0') + 2Cy_0y_0' + D + Ey_0' = 0 \qquad (3\text{-}3)$$

$$x_n^2 + \mathrm{B}x_ny_n + Cy_n^2 + Dx_n + Ey_n + F = 0 \qquad (3\text{-}4)$$

$$\partial\mathcal{E}/\partial\mathrm{B} = \partial\mathcal{E}/\partial\mathrm{C} = \partial\mathcal{E}/\partial\mathrm{D} = \partial\mathcal{E}/\partial\mathrm{E} = \partial\mathcal{E}/\partial\mathrm{F} = 0 \qquad (3\text{-}5)$$

Eqs. 3-2 ~ 3-4 are the boundary conditions. (x_0, y_0) is the coordinate of the start KP in the fitted plane created by the KPs in the first segment, (x_n, y_n) is the coordinate of the end KP in the same fitted plane. y_0' is the slope of the start KP in the newly fitted curve. Depending on the boundary condition, the three equations can be combined in two different ways. For the KP set in the first segment to be calculated, the boundary conditions on two end KPs, Eq. 3-2 and Eq. 3-4 will be incorporated into the linear algebraic equations. For the second segment, besides Eq. 3-2 and Eq. 3-4, Eq. 3-3 will also be substituted into the linear algebraic equations for the continuous and smooth connection between two fitted curves. Due to the number of boundary condition equations being different, the number reduction of the unknown parameters in the vector would be different. For the first segment being fitted, the two boundary condition equations mean that two random unknown parameters can be expressed by other three unknown parameters. An example below was given on the second segment. Three random parameters (e.g. D, E and F) were chosen and could be expressed by other two parameters (B and C in this case), written in Matrix as below:

$$
\begin{pmatrix} x_0 & y_0 & 1 \\ 1 & y_0' & 0 \\ x_1 & y_1 & 1 \end{pmatrix} \begin{pmatrix} D \\ E \\ F \end{pmatrix} = \begin{pmatrix} -x_0{}^2 - \mathrm{B}x_0 y_0 - C y_0^2 \\ -2x_0 - \mathrm{B}(y_0 + x_0 y_0') - 2C y_0 y_0' \\ -x_n{}^2 - \mathrm{B}x_n y_n - C y_n^2 \end{pmatrix} \tag{3-6}
$$

Through the Gaussian elimination method, $(\mathrm{D\ E\ F})'$ could be substituted into the $\mathcal{E}$ function. Solving the extremum conditions could then help calculate the results of $(\mathrm{D\ E\ F})'$. Once the three parameters were obtained, the other two parameters B and C could also be easily obtained through solving the boundary condition equations. Figure 3. 9 is the fitting result of the first column of curves in the longitudinal direction from the medial side of knee joint.

With the same method being applied on each longitudinal curve, new KPs were created through projecting the KPs on each irregular longitudinal curve into the corresponding ellipse fitting curve which was optimized from these KPs. Since the KPs were obtained, the cubic spline was applied to connect each KP in each row or the transverse direction (see Figure 3. 7). Subsequently, the surfaces and the volumes were generated in turn until the final model of the femoral implant component was created. In Figure 3. 10, the femoral implant component is shown in different views with an assembly of the femoral

implant component and the retained femur bone.
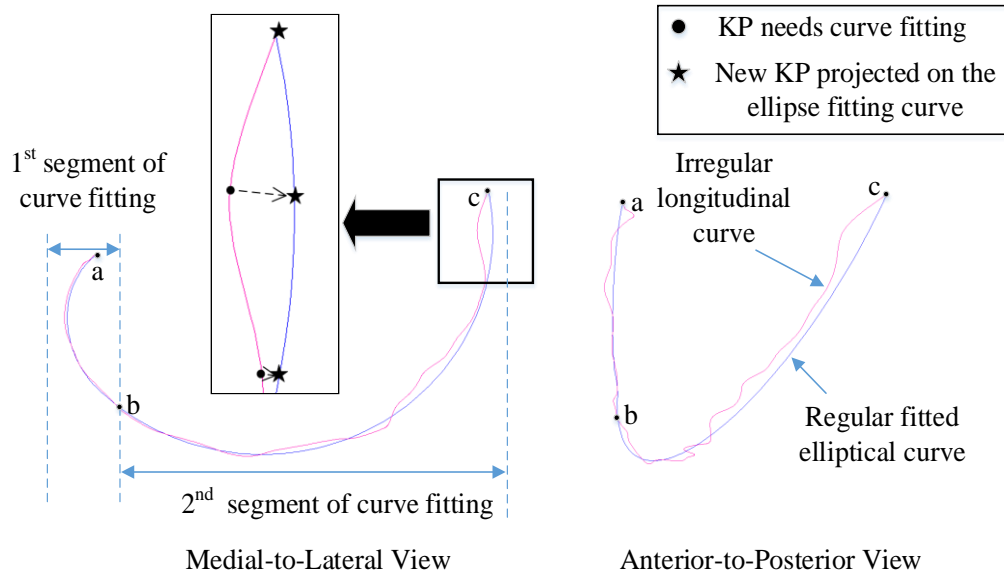
Figure 3. 9 Least squares elliptic fitting

a: the start point of the first segment curve that needs to be fitted; b: the end point of the first segment curve / the start point of the second segment curve; c: the end point of the second segment curve
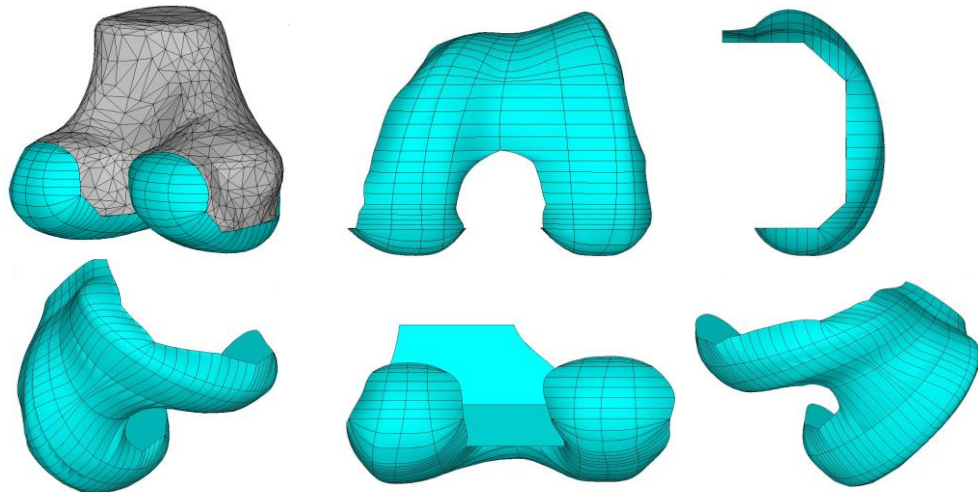
Figure 3. 10 Femoral component in different views and its assembly

Additionally, an off-the-shelf DePuy femoral component [108] is also shown in Figure 3. 11 for dynamic performance comparisons in Chapters 6 and 7. It is a standard size and not made specially to fit a specific patient bone. It has two symmetric arc-shaped condyles with dual femoral radii in the sagittal plane. According to the study of Dai et al. [109], it was installed by aligning the component AP dimension with that of the patient's

distal femur. Meanwhile, the component revolute centre was placed coincident with the femur distal centre which was determined by selecting the middle point between two epicondyle points.

(a)   (b)
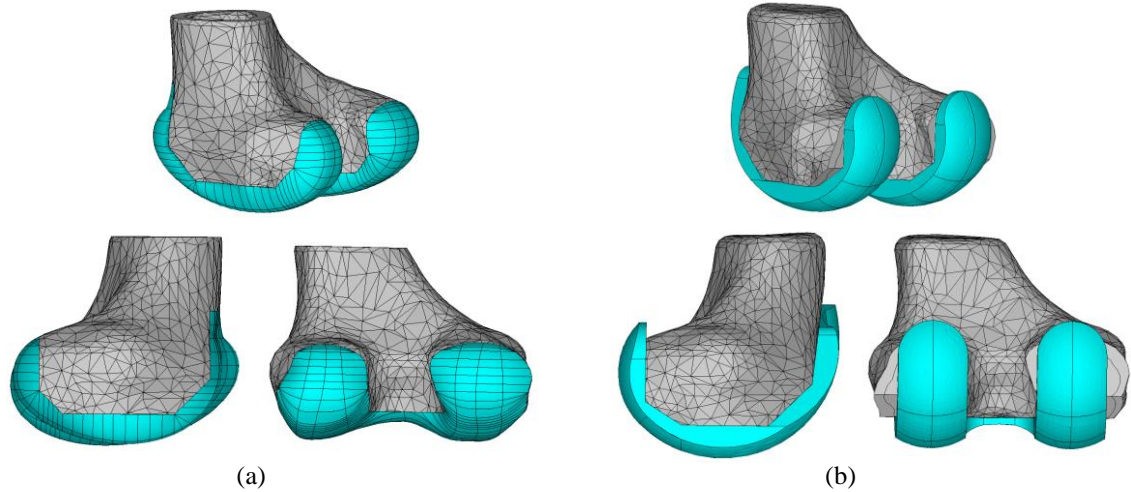
Figure 3. 11 Comparison between (a) the customised femoral component and (b) the femoral component of the DePuy PFC Sigma system [108]

3.4.2 Creating the tibia component

In human's natural tibia plateau, there are two crescent-shaped cartilages: medial meniscus and lateral meniscus, being connected to the tibia bone. The detailed shapes are shown in Figure 2. 2 and Figure 2. 3 in Chapter 2. One of their major functions is to transfer the load from the upper leg to the lower leg and stabilize the knee during the movements of flexion-extension (F-E) rotation, internal-external (I-E) rotation and adduction-abduction (A-A) rotation.[110] However, for our design of tibial replacement, due to the lack of cartilage imaging in CT scans, the tibial bearing surfaces were initially assumed to have two different concave surfaces. Their radii of curvatures were designed to be larger than those of the femoral component, which could enable the femoral component to move smoothly in relation to the tibial counterpart. The relative motions of tibiofemoral joint consist of the F-E rotation, A-A rotation, I-E rotation, superior-inferior (S-I) translation, medial-lateral (M-L) translation and anterior-posterior (A-P) translation between femur and tibia.

When the femoral implant is built, the shapes of its two are utilized to create tibial bearing surfaces. Before that, a block is first used to cut subject's tibia plateau, and then

the edge contour of retained bone is selected to build the circumferential profile of the initial tibial implant component so that the bottom of the implant could best match the after-resection tibia bone.
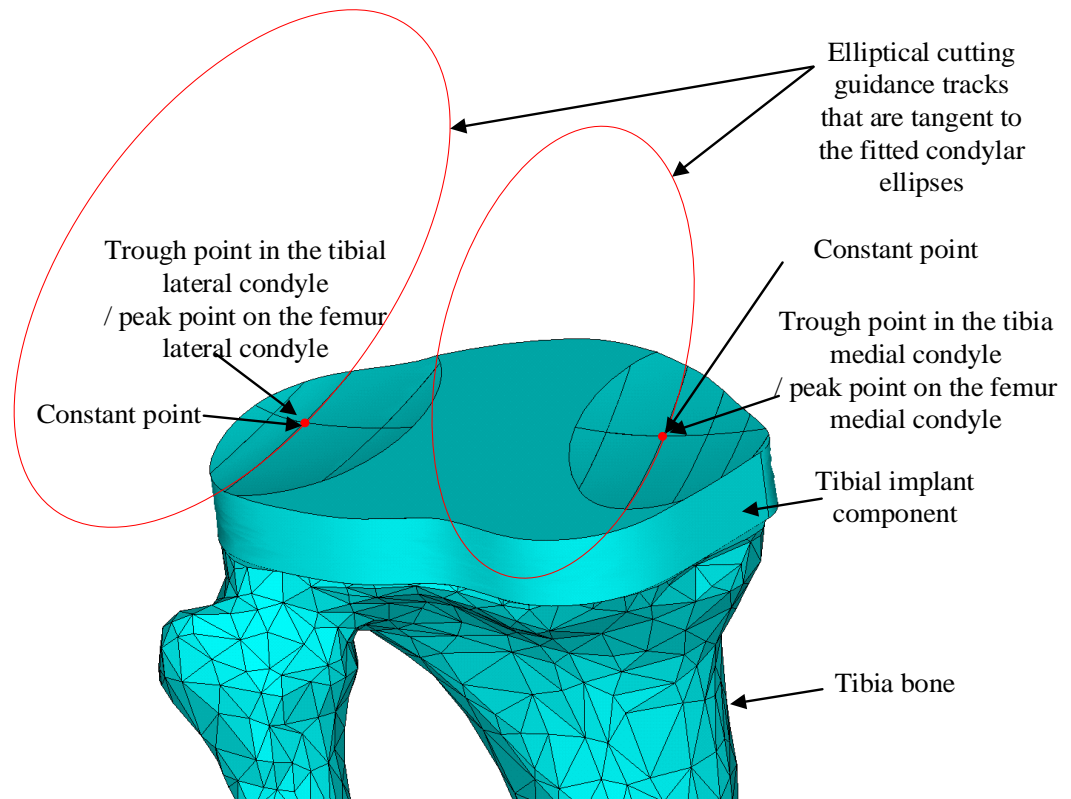
Figure 3. 12 Tibial implant component and tibia
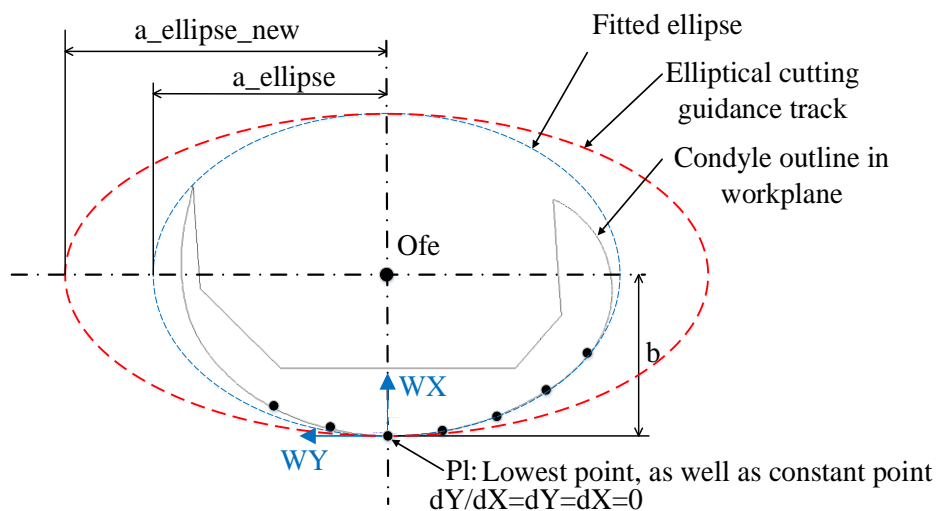
Figure 3. 13 Cutting guidance curve for building tibial bearing surface

Subsequently, for each condyle of the femoral implant, the maximum KPs on the transverse condylar contours were re-selected to determine the orientation of the cutting

guidance curves for building two tibial bearing surfaces. The least squares elliptical curve fitting was applied on these KPs to obtain the long and short axes radii for each condyle. Among these selected maximum KPs, the one located in the most distal in the vertical direction of each condyle would be defined as a constant point which is shown in Figure 3. 12. It is also the lowest point in Figure 3. 13. It acts as an extreme point where both cutting guide curve and profile curve intersect. Via adjusting the long axis radius of each fitted ellipse, different curvature of tibial bearing surface in its sagittal plane could be created. Meanwhile, the newly adjusted ellipse is definitely tangential to the fitted one in the constant point.

The lowest point on each condyle is always located on the middle contour curve of each condylar in the longitudinal direction. The middle contour curve is also the longest contour curve in each condyle of the femoral component in Figure 3. 10. Because the aforementioned condylar curve consisted of several spline curves with discrete KPs on two oblique planes in Figure 3. 9, only the KPs on the posterior and distal condyles were selected to be projected onto a fitting plane. This plane was determined by three average points of those selected KPs. Lastly, a least squares elliptical fitting equation in Eq. 3-7 was used to obtain an ellipse which would be the closest to those projected KPs shown in Figure 3. 13.

$$\mathcal{E} = \sum_{i=0}^{n} (x_i^2 + By_i^2 + Cx_i + Dy_i + E)^2 \tag{3-7}$$

Since the boundary conditions $x_0 = y_0 = y_0' = 0$ are known, they are substituted into Eq. 3-7 and its corresponding derivative equations shown in Eq. 3-8:

$$\begin{cases} 2x_0 + 2By_0y_0' + C + Dy_0' = 0 \\ x_0^2 + By_0^2 + Cx_0 + Dy_0 + E = 0 \end{cases} \tag{3-8}$$

$C = E = 0$ was then obtained. The Eq. 3-7 is transformed:

$$\mathcal{E} = \sum_{i=1}^{n} (x_i^2 + By_i^2 + Cx_i + Dy_i + E)^2 = \sum_{i=1}^{n} (x_i^2 + By_i^2 + Dy_i)^2 \tag{3-9}$$

$$\partial\mathcal{E}/\partial B = 2\sum_{i=1}^{n} (x_i^2 + By_i^2 + Dy_i) \cdot y_i^2 = 0 \tag{3-10}$$

$$\partial\mathcal{E}/\partial D = 2\sum_{i=1}^{n} (x_i^2 + By_i^2 + Dy_i) \cdot y_i = 0 \tag{3-11}$$

Once the coefficients B and D were solved through the Eq. 3-10 and Eq. 3-11 with substituting the coefficient C and E, the fitting elliptical equation could be obtained as Eq. 3-12:

$$x^2/(D^2/4B) + (y + D/2B)^2/(D^2/4B^2) = 1 \qquad (3-12)$$

Its long axis radius of elliptical curve is $a_{ellipse} = \sqrt{D^2/4B}$. While keeping the short axis radius constant, increasing $a_{ellipse}$ to a new value $a_{ellipse\_new}$ would increase the radius of curvature of the ellipse, it would make the cutting guidance track and its counterpart tibial bearing flatter. In the following chapter of dynamic analysis, the relation of $a_{ellipse\_new} = 4 \cdot a_{ellipse}$ was assumed.
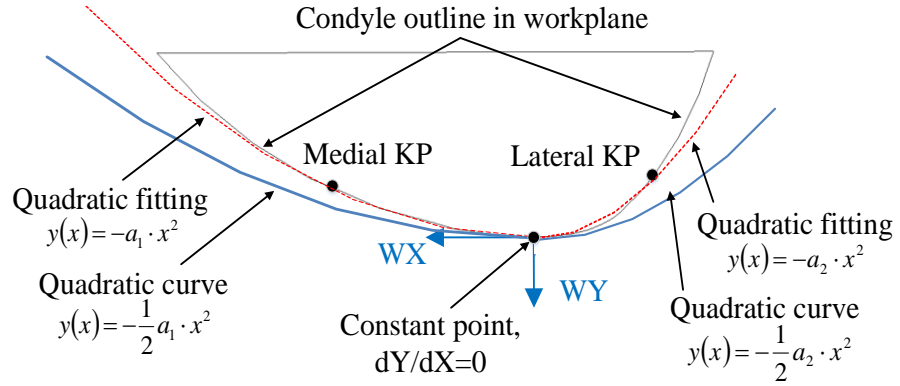
Figure 3. 14 Transverse contour for building tibial bearing

In terms of defining the profile shape of each tibial bearing in the transverse direction, which is shown in Figure 3. 14, the least squares quadratic fittings were implemented on the points that were located on the cross-section curve perpendicular to the plane of cutting guidance curve for each condyle. The cross-section curve also simultaneously passed through the constant point in Figure 3. 12 or the lowest point in Figure 3. 13.

Since the curvatures of each condyle on the medial and lateral sides are quite different, the transverse condylar curve is divided into two segments in Figure 3. 14. Medial and lateral KPs on the condylar curve were selected along with the lowest KP for the least squares quadratic fittings on two sides respectively. The fitted curves are indicated in the red dash curve in Figure 3. 14. The tangent values of two fitting curves at the lowest KP have to be zero in order to guarantee the tangential continuity of two curves. Through adjusting the quadratic coefficients, two quadratic curves with larger radius of curvature

can be created and are indicated in the blue solid curves in Figure 3. 14. The KP in the origin of working plane also coincides with the lowest KP on the femur condyle. Through controlling the quadratic coefficients, the quadratic curves could determine the width and contour shape of the tibial bearing surface in the transverse direction. Consequently, each tibial bearing surface could be created using two quadratic curves as the transverse contour and one elliptical curve as the cutting guidance track, as shown in the Figure 3. 12. In the following chapter of dynamic analysis, the relations of medial quadratic coefficients: $a_{1\_new} = a_1/4$, lateral: $a_{2\_new} = a_2/6$, were assumed in both condyles.
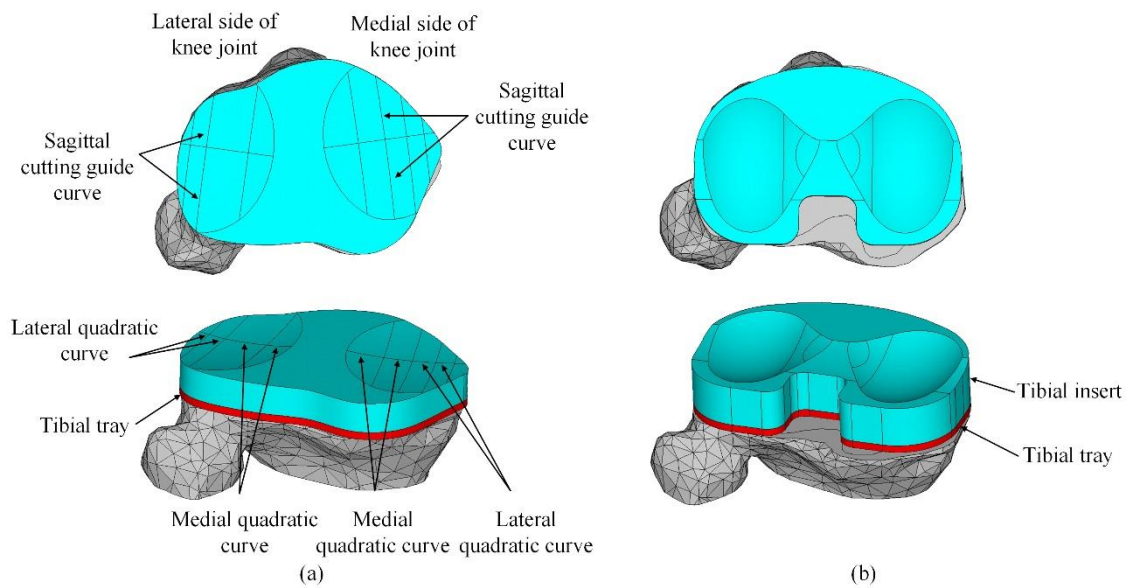
Figure 3. 15 (a) Tibial insert model of CTKI and the tibial tray of 3 mm thickness [108] (red); (b) DePuy PFC Sigma system tibial implant [108]

In contrast with the asymmetric structure of customised tibial implant in the Figure 3. 15(a), the traditional tibial implant is usually designed with two symmetric arc-shaped bearing surfaces, which can be seen in the Figure 3. 15(b). Although the simple and regular shapes provide good conformity between the traditional femoral and tibial component, which is beneficial for reducing contact stresses and material wear, the symmetric structure could also restrain the function of the tibial I-E rotation and other DOF motions. This makes the patients' knee function difficult to be restored to the normal even after TKR surgeries. Its detailed dynamic performances will be assessed under the same computer simulation conditions as applied on the CTKI model for comparisons in Chapters 6 and 7.

3.5 Conclusion

A method of creating a customised femoral component has been proposed based on the geometric shape of patient specific distal femur. The 3D distal femur is created by using 3D Slicer and surface-repaired by using MeshLab. Because it is not initially smooth due to the natural knee anatomic shape, the femur model is then imported into ANSYS mechanical APDL for creating surface-smoothened implant through the proposed methods such as the key feature points identification, least squares elliptical curve fitting and surface regeneration. In terms of the tibial implant modelling, because the information about this patient's menisci is neither available nor usable due to cartilage wear, the tibial bearing surface is created based on the shapes of femoral component condyles by defining an elliptical cutting guidance track in the longitudinal direction and two quadratic curves in the transverse direction on each condyle. The curvatures of these curves are smaller than those of the femoral component contour, so the femoral implant can move in relation to the tibial counterpart in all six DOFs with certain ranges.

The CTKI can effectively solve the problem of femoral component overhang/underhang over the femur bone, and further alleviate the residual pain on the knee joint. But whether the knee function could be restored or not by placing the CTKI on the patient's knee is still unknown. It has to be validated through the dynamic simulations in the following chapters.

Developed in ANSYS Mechanical APDL which is a built-in programming language for parametric design, the CTKI can be easily and quickly modelled and modified under different parameters, for instance, the tibial bearing surface curvatures in both longitudinal and transverse directions. Besides, ANSYS Mechanical APDL itself is a very powerful finite element (FE) simulation software. The established CTKI model can be directly applied different boundary conditions for the contact stress/force calculations and motion analysis without being exported into another FE software.

Chapter 4

OpenSim subject-specific musculoskeletal modelling

4.1 Introduction

To test the total knee replacement (TKR) or cadaveric knee joint specimens, loads that the human knee is subjected were usually applied in the experimental rigs or simulation models. Depending on the test mechanism, some applied loads or motions on the jigs that directly held the knee implants, while some applied them on the motion rods which accommodated the TKR and acted as the lower extremity. For instance, the Stanmore knee simulator was used for the wear test of TKR. Its input loads are standard data for testing, and it only recruited the loads applied on the femoral and tibial components but excluded the effect of patella and ligaments around the joint. In other knee test rigs or simulators such as the Oxford knee rig (OKR) and the Kansas knee simulator (KKS), loads were applied on the virtual hip and ankle joints and quadriceps muscles, but those loads were only experimentally combined to duplicate the desired tibiofemoral compressive force, which in reality is dependent on all of the muscles across the knee joint as well as the moving upper body mass. Therefore, before testing the performance of customised TKR design, a patient-specific musculoskeletal model needed to be built for acquiring closer-to-physiological muscle and joint reaction forces that a specific subject could produce during a daily activity.

Human biomechanical models are complex and comprised of skeletal models, joint structures, soft tissues such as muscles and ligaments and a contact mechanics model. In order to build such complicated systematic model, OpenSim was developed by the national centre for simulation in rehabilitation research at Stanford University. It is a freely available musculoskeletal modelling software that enables users to develop models of musculoskeletal structures and create dynamic simulations of movement based on subject-specific experiment data such as motion trajectories and ground reaction forces.[84] Additionally, a muscle model [111] that acts more physiologically is included in the musculoskeletal model by considering an active actuator element and a passive spring element. The active muscle actuator is controlled by optimization algorithm that minimizing the sum of squared muscle activations, while the passive

spring element is a nonlinear spring with a function of force-length deflection.

The main tools in the OpenSim include the model scaling tool, for fitting generic models to subject-specific data; inverse kinematics (IK), for resolving internal coordinates from available spatial marker positions corresponding to known landmarks on rigid segments; inverse dynamics (ID) for determining the set of generalized forces necessary to match estimated accelerations; residual reduction algorithm (RRA) for minimizing the effects of modelling and marker data processing errors that aggregate and lead to large nonphysical compensatory forces called residuals [112,113]; static optimization (SO) for decomposing net generalized forces amongst redundant actuators (muscles); forward dynamics (FD) for generating trajectories of states by integrating system dynamical equations in response to input controls and external forces; and computed muscle control (CMC) for calculating muscle forces and activations by using motion feedback control algorithm based on SO and FD [114,115].

It is worth noting that the FD tool enables users to calculate the joint forces by inputting calculated or measured muscle forces. However, since the natural knee articulation shape of the subject has been changed through the TKR surgery by being replaced with a traditional design implant or a customised one, the relative motions between femoral and tibial component would be different from that before the surgery. If applying mesh geometries (obj. file) of implant components in the FD analysis, the analysis would diverge due to the over-interpenetration between two contact surfaces. Decided by the elastic foundation contact algorithm [88] used in OpenSim, this over-interpenetration depth will produce extra-large contact forces that other forces such as joint loads and muscle forces cannot balance against. If applying mesh geometries from the beginning of the IK analysis to the SO or CMC muscle analysis, the knee joint reaction forces and muscle forces will become exaggeratedly high, because these analyses are performed by tracking the patient-specific joint motion trajectories generated by IK [116]. In other words, incorporating detailed joint geometry and its effect on the contact forces into the musculoskeletal model is only applicable for the inverse analyses, motion dependent force analyses where the motions are known beforehand. Although in the CMC [114], a FD analysis is built inside in order to calculate the joint motions for feedback controls, the joint motions produced by IK are still the objective that this optimisation algorithm tracks. Importing mesh geometries of implant components can also make the simulation

fail with divergence.

Accordingly, in this chapter, a patient-specific musculoskeletal model is built from the generic model 2392 (23 DOFs and 92 muscles) to calculate the left lower limb muscle forces and joint loads without consideration of the effect of knee contact forces. By using the patient-specific test data such as marker trajectories through motion captures, and the ground reaction forces (from 4th Grand Challenge Competition to Predict In Vivo Knee Loads [117]) through the force plate measurements, the patient-specific loads such as muscle forces and joint reaction forces can be calculated by using the tools of SO and the joint reaction analysis respectively. In Figure 4. 1, the process for calculating the patient-specific loads during a squatting motion is presented. The reason why the squatting motion is studied is because of its large range of knee flexion compared to other daily activities such as walking, stair-ascending and descending. Additionally, due to the limitations of OpenSim aforementioned, the patient-specific loads such as muscle forces and angular displacement of hip flexion will be exported into the next stage multibody dynamic analysis for evaluating the biomechanical performances of the total knee implants.
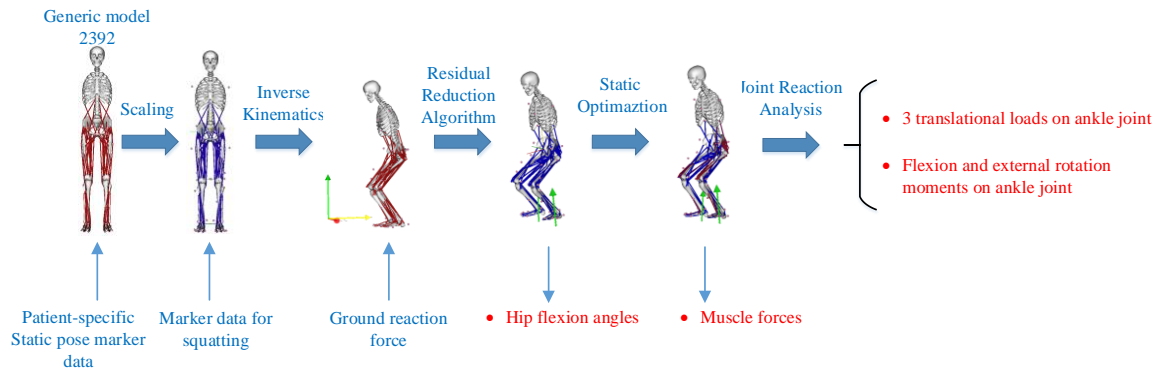
Figure 4. 1 Process of patient-specific loads calculation for a squatting motion

4.2 Model scaling

A generic model (Gait2392_Simbody) from the Examples and Tutorials of OpenSim documentation [118] is used to create a subject-specific musculoskeletal model in conjunction with the experimental marker data in the static standing pose. The Gait2392 model is a 23-degree-of-freedom computer model of the human musculoskeletal system with 92 musculotendon actuators, and represents a subject of 1.8 m height and 75.16 kg

weight. By inputting a weight of 66.7 kg and a height of 1.68 m of a specific subject JW [14], and the marker data of the static standing pose, the JW musculoskeletal model was created and shown in Figure 4. 2. The information of femur and tibia's masses and mass centres is shown in Table 4. 1. The reason of only the subject's left leg masses being listed is because the implant components were built based on the CT medical images of that subject's left knee joint, and the dynamic simulations on the left leg needed to be conducted.

Table 4. 1 Subject-specific left leg masses and mass centres scaled from the generic model

	Mass (Kg)	Mass centre (m)	Inertia xx (kg·m²)	Inertia yy (kg·m²)	Inertia zz (kg·m²)
Femur	8.25	(0 -0.173507 0) in Hip joint coordinate system	0.1237	0.0324	0.1305
Tibia	3.29	(0 -0.188756 0) in Knee joint coordinate system	0.0457	0.0046	0.0463
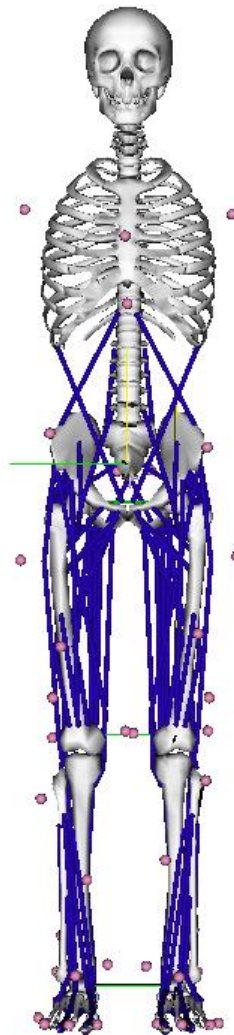
Figure 4. 2 Subject-specific musculoskeletal model scaled from the generic model, pink sphere represents motion capture marker and blue lines represent muscles

The hip joints and lumbar joint were defined as ball joints that have three DOFs, flexion-extension (F-E) rotation, adduction-abduction (A-A) rotation, and internal-external (IE) rotation. The knee joint was only allowed to have F-E movement as a pin joint. The ankle joint was also a pin joint which only allowed the foot to have dorsiflexion and plantar flexion.

4.3 Inverse kinematics analysis

By inputting the motion capture data (marker trajectories) in the module of IK, joint angles (see Figure 4. 3) were obtained by best matching experimental markers attached to the specific subject with the virtual markers defined in the musculoskeletal model. The algorithm of inverse kinematics (IK) utilised here is the weighted least squares equation solution which aims to minimize both marker and coordinate errors. The marker weights and coordinate weights are specified respectively. The kinematic result of subject left leg was shown for the next stage dynamic test on the CTKI which was built from the subject left leg. The results of the right leg, pelvis and torso were also obtained. Those segments are indispensable in the musculoskeletal model simulation for considering the dynamic balance of body weight with the ground reaction force in the following ID analysis.
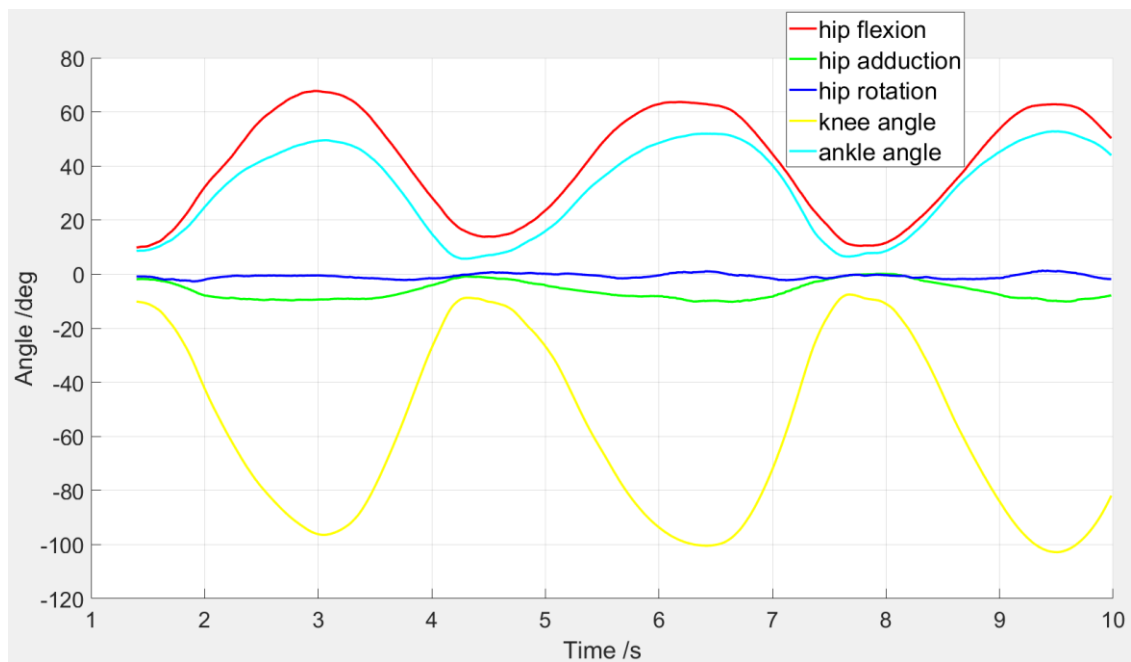
Figure 4. 3 Kinematics results of the hip, knee and ankle joints of the subject's left leg

4.4 Inverse dynamics analysis

In the ID analysis, the ground reaction forces and torques were applied to two feet (calcaneus bones) respectively. By solving Newton second law equations, each joint's generalized forces could be obtained. In Figure 4. 4, the joint loads of the subject's left leg were plotted. These values can be used to estimate the joint actuator values in the next RRA analysis.
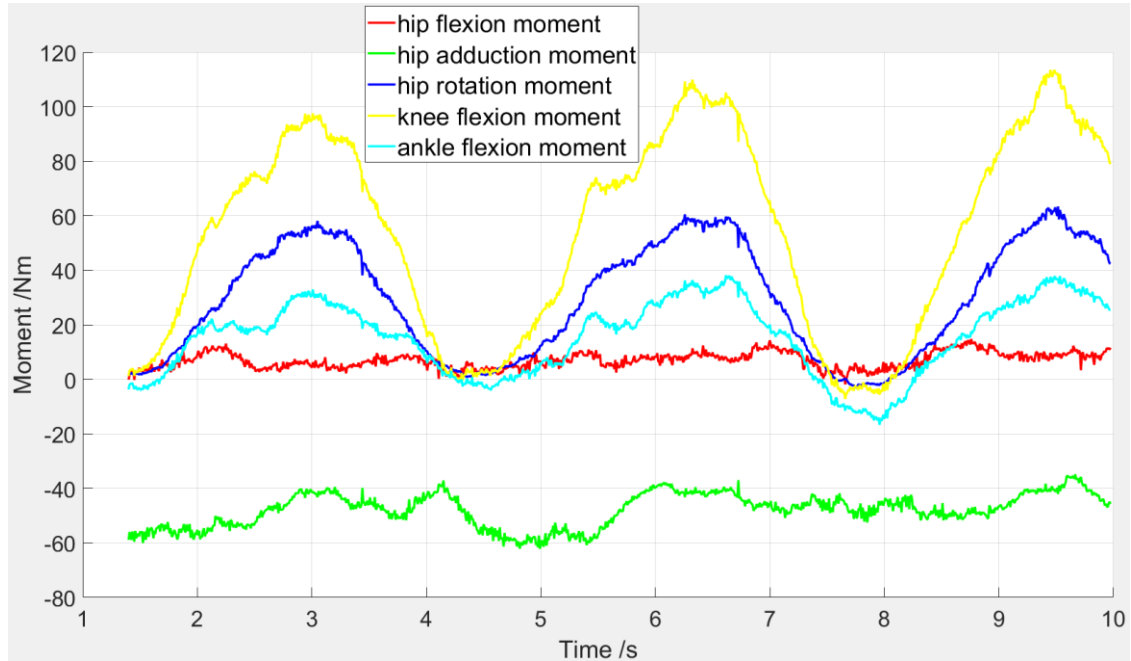
Figure 4. 4 Dynamic moment results of the hip, knee and ankle joints of the subject's left leg

4.5 Residual reduction algorithm analysis

The purpose of using this tool is to minimize nonphysical compensatory forces called residuals which are applied on the mass centre of pelvis in order to make joint kinematics more dynamically consistent with the ground reaction force data. Different from the former two inverse simulation analyses, the residual reduction algorithm (RRA) is a form of forward dynamics simulation that use tracking controller to follow the model kinematics results from the IK. The joint controllers or actuators rather than muscle forces are used to drive joints of the model to move from one configuration (generalized coordinates) to the desired one in the next time step. The actuator forces and their corresponding activations are computed by minimizing an objective function in Eq. 4-1 which is the sum of squared actuator controls (x_i) plus the weighted sum of desired

acceleration ($\ddot{q}_j{}^*$) errors.

$$J = \sum_{i=1}^{nx} x_i^2 + \sum_{j=1}^{nq} w_j\left(\ddot{q}_j{}^* - \ddot{q}_j\right)^2 \tag{4-1}$$

The first summation minimizes and distributes loads across actuators and the second drives the model accelerations ($\ddot{q}_j$) toward the desired accelerations ($\ddot{q}_j{}^*$).

Each actuator controls each DOF of joint. Instead of applying residuals applied on pelvis mass centre arbitrarily large, they are also controlled by actuators: point actuators for translational DOFs and torque actuators for rotational DOFs. By this way, the motion is ensured to be predominately generated by the internal joint moments rather than the unrealistic supplementary loads which, on one hand, are necessary to satisfy the Newton's Second Law, but on the other hand, would inevitably alter the model's motion from the IK analysis.
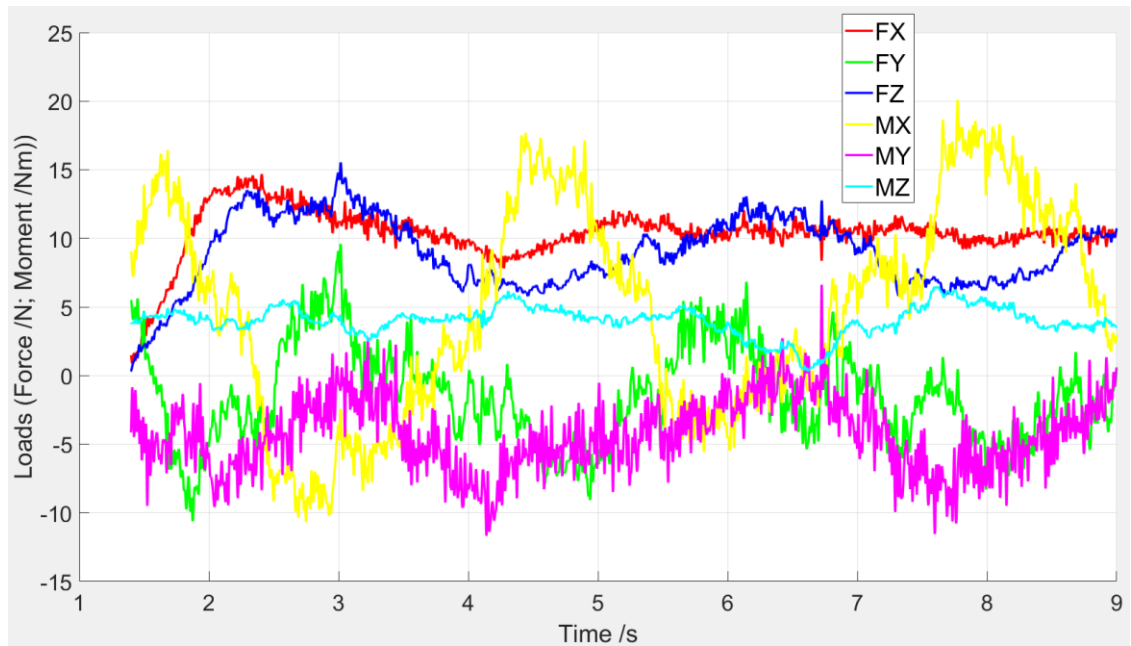
Figure 4. 5 Residual forces (FX, FY and FZ) and moments (MX, MY and MZ) applied on the pelvis mass centre

The pelvis residual forces and moments which are nonphysical compensatory loads are shown in Figure 4. 5, representing the simulation loading error for making the measured ground reaction forces dynamically consistent with the inverse kinematic result obtained through the motion capture markers (pink spheres) in Figure 4. 2. To verify that the simulation errors are small enough, both the maximum and root mean square of residual

loads are required to be within the ranges of evaluation thresholds in Table 4. 2. The residual results in this study are found to be within those ranges.

Table 4. 2 Threshold values for evaluating RRA results [119]

Thresholds:	GOOD	OKAY	BAD
MAX Residual Force (N)	0-10 N	10-25N	> 25 N
RMS Residual Force (N)	0-5 N	5-10 N	> 10 N
MAX Residual Moment (Nm)	0-50 Nm	50-75 Nm	>75 Nm
RMS Residual Moment (Nm)	0-30 Nm	30-50 Nm	>50 Nm
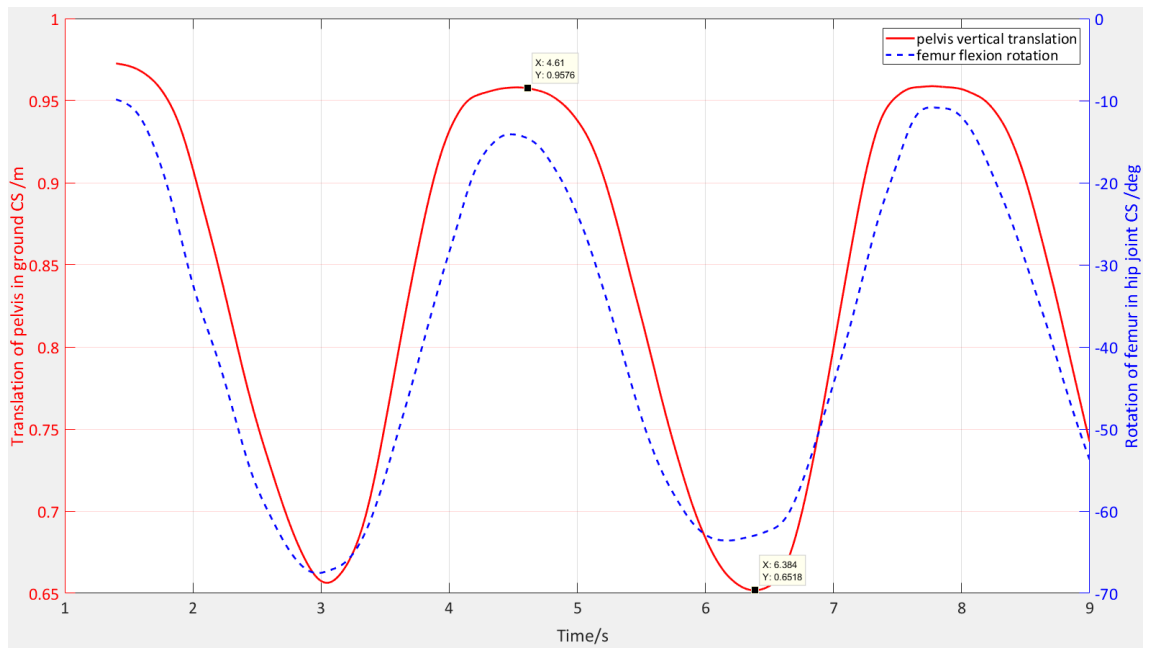
Figure 4. 6 Kinematics results of pelvis vertical translation and hip flexion rotation from SO

The motion of model has been changed due to the application of residual loads. In order to apply customised forces such as muscle and joint reaction forces calculated from OpenSim onto the FE simulation in the following chapters, the forces or displacement loads need to be expressed in the same range of time. In Figure 4. 6, both pelvis translation in vertical direction and hip joint flexion rotation are plotted. The vertical movement of pelvis indicates the process of subject squatting from the standing posture to the maximum knee flexion posture that the subject JW could perform. The motion results in the time range between 4.61 seconds and 6.384 seconds are extracted, which represents the motion from the upright standing posture to the lowest posture that the subject could squat to. But at 6.384 seconds, which is the ending time we choose for dynamic analysis, it does not necessarily mean the maximum flexion angle that this subject hip joint has to reach. In fact, as can be seen from the blue curve, the hip joint

has already extended to some angles, while the upper body just reaches its lowest posture in this cycle of motion. Because much more muscle forces are needed for resisting gravity and inertial effects so as to push up the upper body, maximum knee contact force is expected to occur at this selected ending point of time.
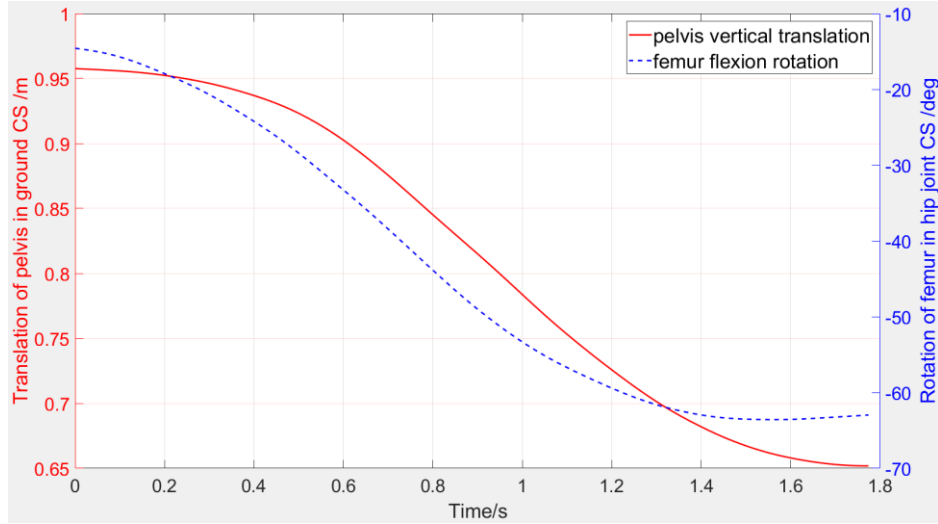
Figure 4. 7 Normalized femur flexion angles

The hip flexion rotation in Figure 4. 7 will be imported into the FE dynamic analysis with its time normalized to the range from 0 to 1.774 seconds. Besides, the muscle forces which will be calculated in SO and the joint reaction forces calculated in the following will all be extracted in the time range between 4.61 seconds and 6.384 seconds and re-expressed in the time from 0 to 1.774 seconds.

4.6 Static optimization analysis

The SO analysis was performed by tracking the motion angles calculated through the IK analysis. The muscle forces were solved by minimizing the sum of squared muscle activations through the OpenSim inbuilt solver. The active muscle force was modelled in relation to muscle length and its contraction velocity, while the passive element of muscle was in tension only with its force dependent on muscle length [85–87]. In Figure 4. 8, the muscles across the knee and ankle joints were plotted and will be imported into the dynamic FE model in the following chapters. The reason why muscles across hip joint were excluded for FE dynamic analysis was to save computational cost and meanwhile, and the effect of these muscles could be substituted by the function of hip flexion angles versus time which was calculated through the RRA. The adduction-abduction (A-A) effect of hip joint muscles was also neglected by leaving the A-A DOF

of hip joint free adjusting itself to the forces and moments produced by the two tibiofemoral condyles in contact.

(a)

(b)
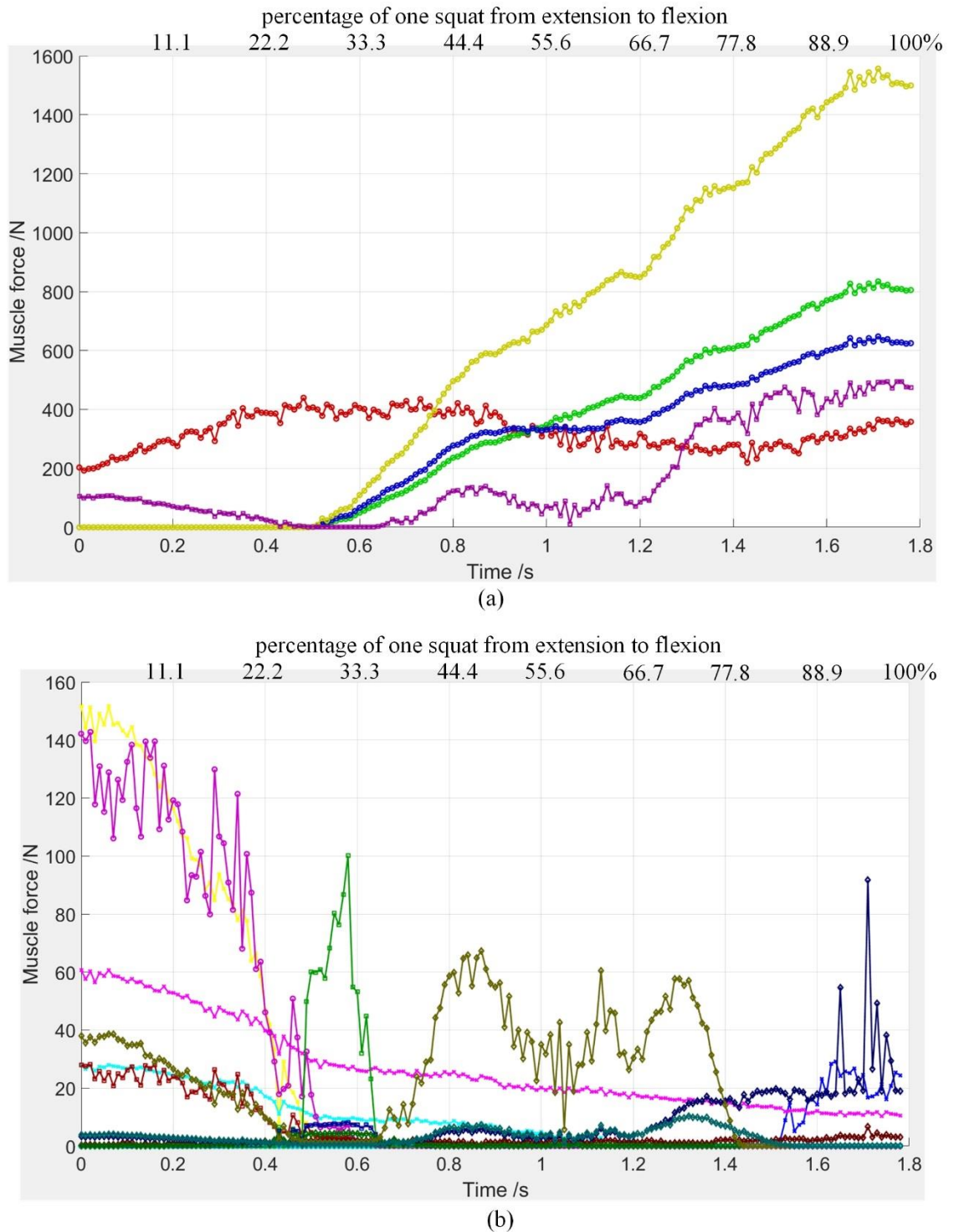
Figure 4. 8 Forces of muscles across knee and ankle joint of the subject left leg in both time and percentage of one squat from extension to flexion, (a) quadriceps muscle bundles and tibialis anterior; (b) remaining left leg muscles

Table 4. 3 Representations of line results in Figure 4. 8 and Figure 4. 9

Line in Figure 4. 8	Abbreviation	Full name of muscle
	rect fem	rectus femoris
	vas med	vastus medialis
	vas int	vastus intermedius
	vas lat	vastus lateralis
	tib ant	tibialis anterior
	semimem	semimembranosus
	semiten	semitendinosus
	bifemlh	biceps femoris long head
	bifemsh	biceps femoris short head
	sar	sartorius
	tfl	tensor fasciae latae
	grac	gracilis
	med gas	medial gastrocnemius
	lat gas	lateral gastrocnemius
	soleous	soleous
	tib post	tibialis posterior
	flex dig	flexor digitorum
	flex hal	flexor hallucis
	per brev	peroneus brevis
	per long	peroneus longus
	per tert	peroneus tertius
	ext dig	extensor digitorum
	ext hal	extensor hallucis

As the primary movers during squat motion, quadriceps provided much larger forces than any other muscles across the hip and ankle joints shown in Figure 4. 8. The rectus femoris (RF) force increased from 200 N to 400 N in the beginning 0.5 seconds of normalized squatting time, when hip joint began to flex and upper body began to move downward. Subsequently, the force remained relatively constant for the whole squatting motion. However, different from the changing pattern of rectus femoris force, the other three bundles showed similar patterns but different magnitudes. The vastus lateralis (VL) produced much larger forces than the other two bundles. The maximum force of VL could reach about 1600 N, equivalent to 2.35 times BW. All of these three bundle forces remained small in the beginning of hip flexion and then sharply increased to their maximum values at about 1.7 seconds which corresponded to the lowest posture of upper body in the SO motion result in Figure 4. 6. It is consistent with the study of Escamilla [83] that vasti muscles showed significantly higher activity than the rectus femoris, and peak quadriceps activity occurred at 80-90 degrees of a squat, with no further increases with greater knee flexion.

(a)

(b)
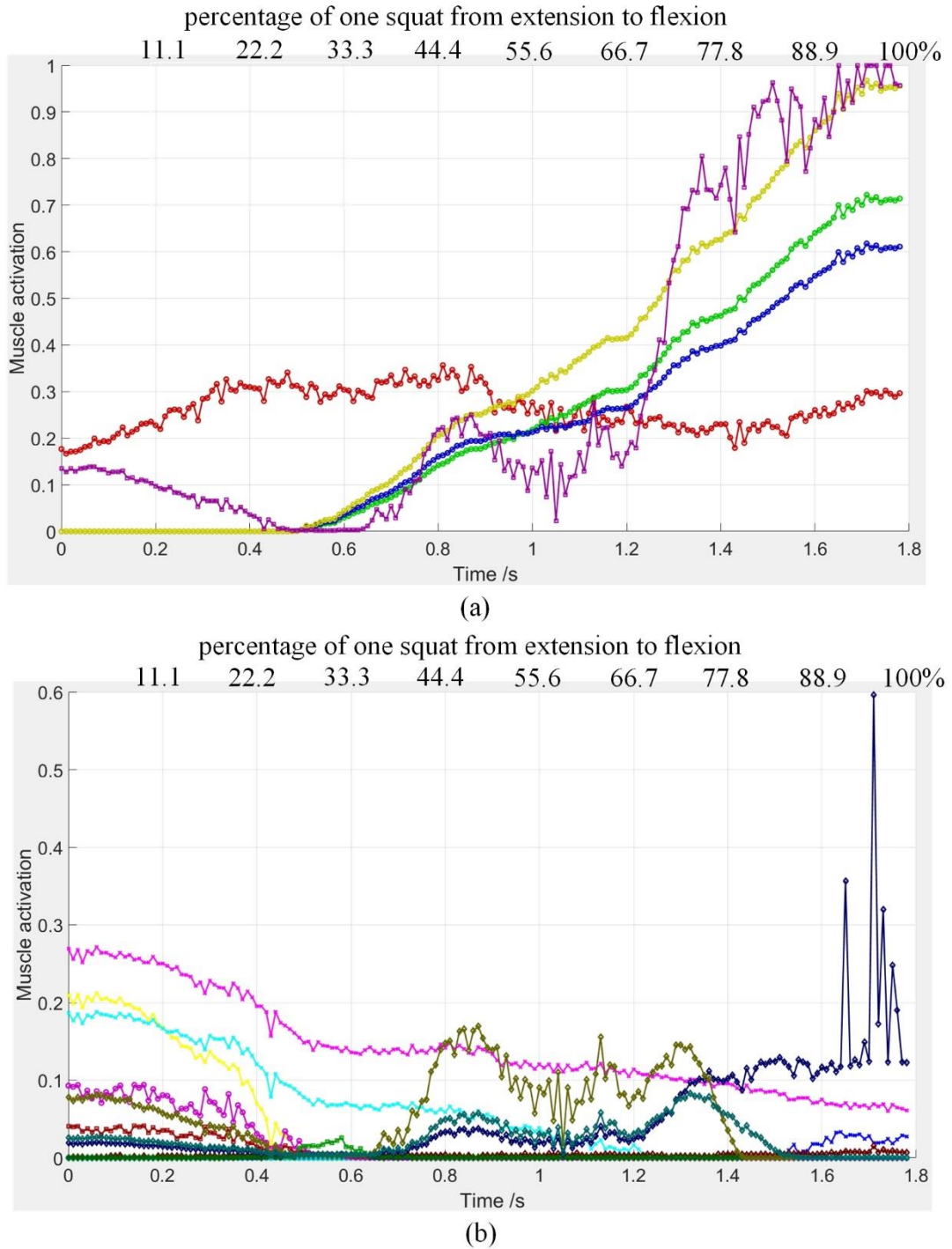
Figure 4. 9 Activations of muscles across knee and ankle joint of the subject left leg in both time and percentage of one squat from extension to flexion, (a) quadriceps muscle bundles and tibialis anterior; (b) remaining left leg muscles

The muscle activations were also calculated as independent variables in the SO analysis. As can be seen in Figure 4. 9, quadriceps activities were much higher than the hamstrings and calf muscles, which was in good agreement with the study of Marchetti et al. [120]. Besides, the tibialis anterior (TA) was also highly activated with the knee flexion, while

the gastrocnemius, sartorius, biceps femoris and tensor fasciae latae (TFL) became less active during the process.
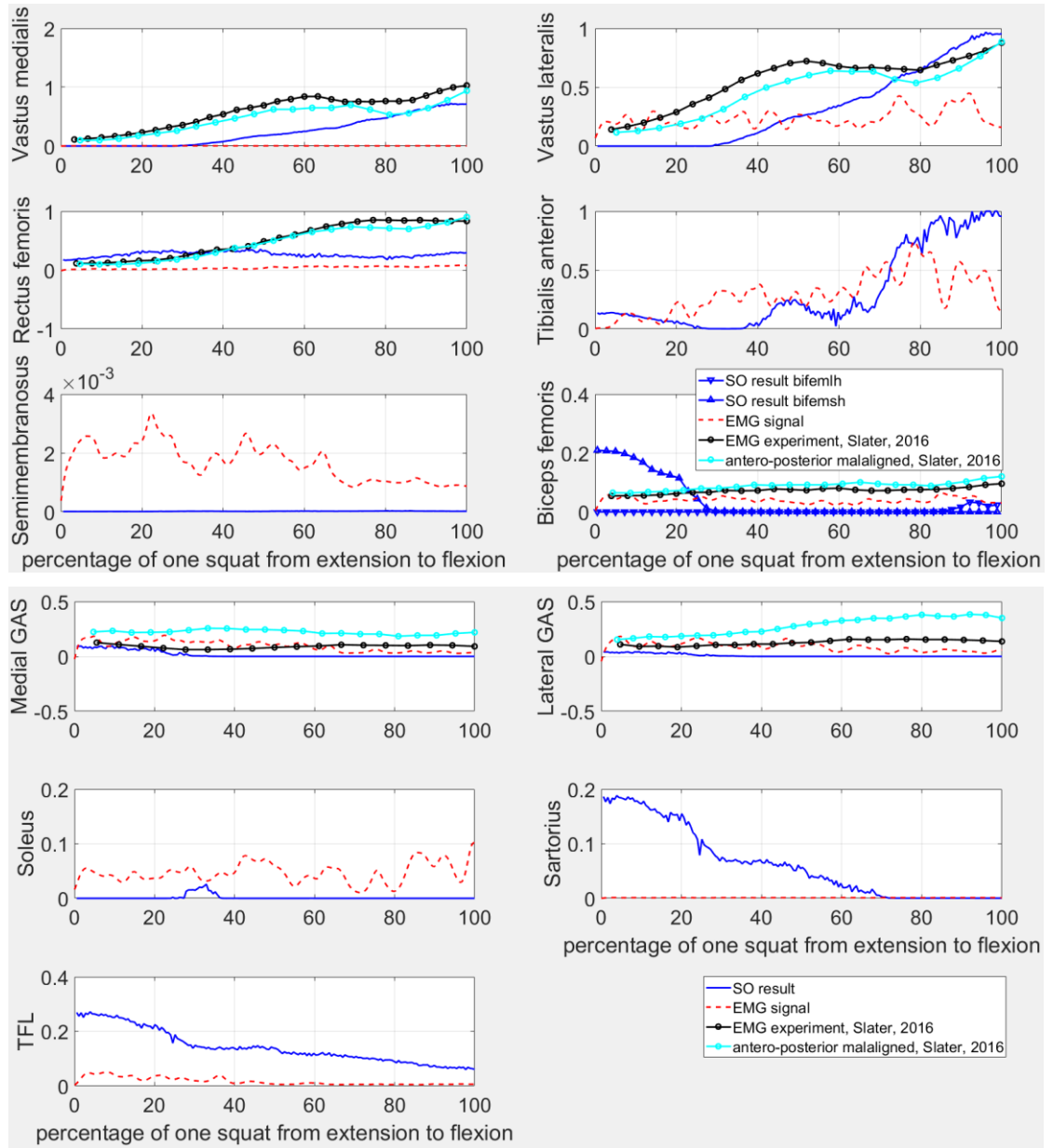
Figure 4. 10 comparison between the simulated SO muscle activations in blue lines and the referenced EMGs [14,117] in red dash lines, black and cyan circle lines represent the experiment results measured by Slater et al. [121]

Through the processes of removing DC offsets, band pass filtering, rectification and low pass filtering, the experimental results [14,117] of electromyography (EMG) were used to compare with simulation results in Figure 4. 10. EMG is an electrodiagnostic medicine technique for evaluating and recording the electrical activity, activation level produced by skeletal muscles. In this study, closer-to-physiological muscle forces are expected to obtain in a reasonable numerical range and then applied on the next-stage

dynamic TKI FE models. However, the exact muscle force values are very difficult to measure or validate in reality. Therefore, the experimentally measured EMG signals are used to compare with the simulated muscle activations in order to ensure the simulated muscle activities generally consistent with realistic muscle physiology.

It is noticeable that only some parts of the simulated muscles in this study responded like the EMG counterparts. In Figure 4. 10, the activations of vastus medialis (VM), RF, sartorius (SAR), TFL were much larger than EMG values, while that of semimembranosus (SMM) and soleus (SOL) were smaller than EMG values. Especially for SMM, both estimated activation and EMG were smaller than 4×10^{-3}, which indicated that it was inactive. In addition to SMM, small activations were also observed in the biceps femoris (BF) that also comprises the hamstring muscles, so it can be concluded that the hamstring muscles did not contribute significantly to the squat motion as the quadriceps. This is mainly because during the knee flexed, the hip joint also flexed resulting in minimal change to the hamstring length.

For the quadriceps, both simulated VL and VM muscles were in good agreement with the experimental results conducted by Slater et al. [121] but different from the EMG results provided by Fregly [14] in terms of magnitude and trend. Although the simulated RF did not increase as the result presented by Slater et al. [121], it was consistent with the result collected by McCaw et al. [122], which also showed relative constant activation during the descent phase of squat motion.

In order to compare the trend of the simulated muscle activations with the EMGs, all of them were normalized by their respective maximum magnitudes. In Figure 4. 11, the TA and TFL showed good agreement with their corresponding EMG results. However, both gastrocnemius muscles (MGAS and LGAS) were only activated in the first twenty percent of simulated motion for providing stability to the knee joint, while the EMG showed gradually decreasing trends of activation. In contrast, the corresponding EMG results got by Slater showed slight increase in the lateral bundle and relative constant in the medial bundle. This can be explained that the length of GAS shortened during the knee flexion due to the reducing distance between two muscle insertions or less muscle wrapping in the musculoskeletal model. The muscle wrapping effect decides the changing rate of muscle length between two muscle insertion points. The more muscle

tissues are wrapped around the posterior femoral condyles, the slower the muscle length will shorten and the longer the muscle will stay in activation state. Additionally, the activation of GAS also depends on how much the foot toes point forward or heel lift off the ground.[121] As can be seen in Figure 4. 10 and Figure 4. 11, the BF and GAS measured by Slater et al. [121] were more active during the anteroposterior mal-aligned squat than that during the control group squat where the heels were kept on the floor and knees in line with feet.
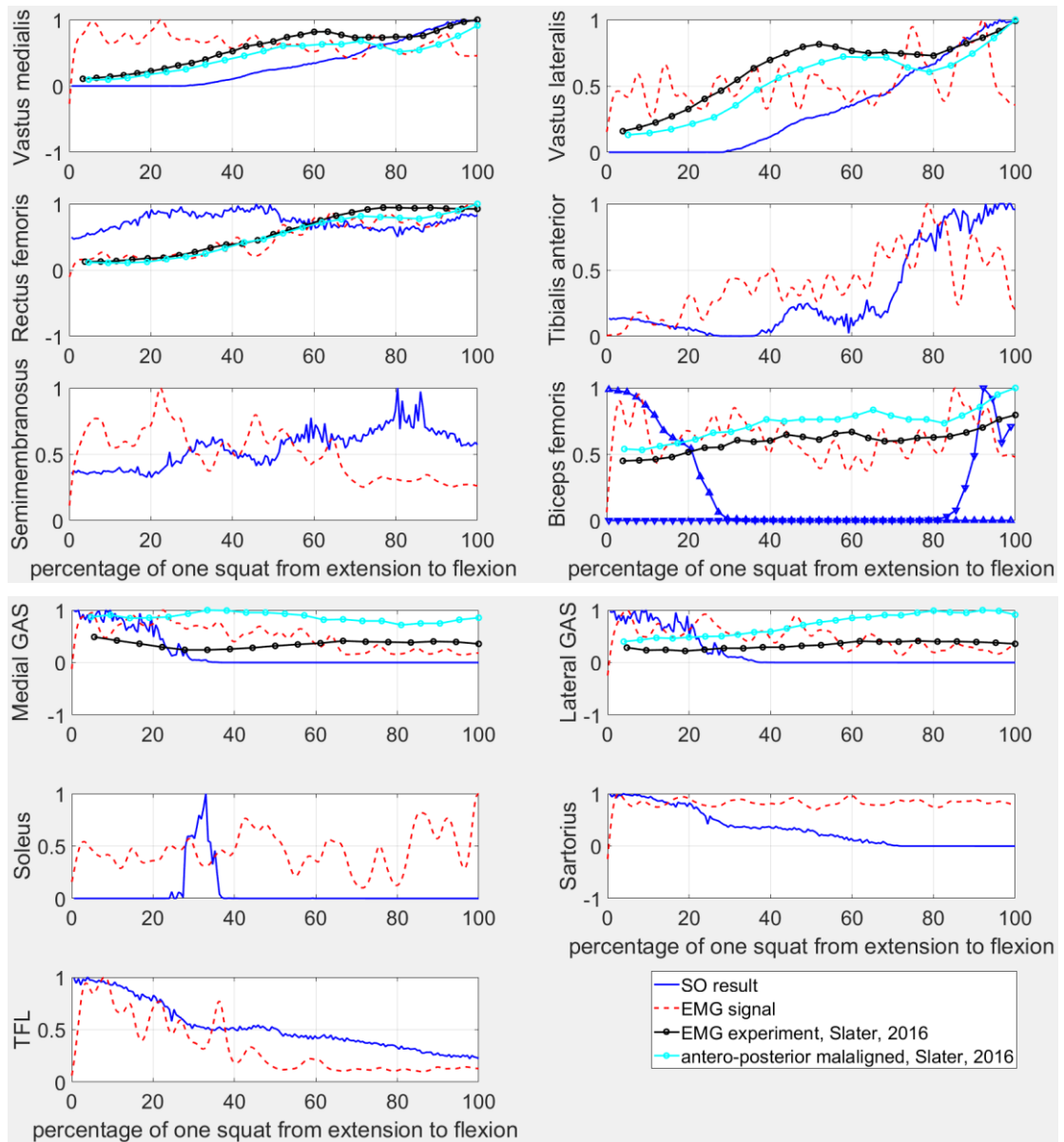
Figure 4. 11 Comparison between normalized SO muscle activations in blue lines and the referenced EMGs [14,117] in red dash lines, black and cyan circle lines represent the experiment results measured by Slater et al. [121]

Although the comparisons in Figure 4. 10 and Figure 4. 11 are not completely consistent, it is worth noting that differences between simulated activations and EMGs were also presented by Wibawa et al. [123], Navacchia et al. [124], Thelen et al. [125], Zheng et al. [126] and Adouni et al. [127]. The disparity between experimental results of EMG and simulated muscle activations might be attributed to the muscle model error, attached-on-skin EMG measurement error and the uncertainty of muscle synergic excitement mechanism. Apart from the above reasons, the errors due to the algorithm would be another important factor for the differences between simulation and EMG or between two simulations. Trinler et al. [128] compared estimated muscle activations of the SO and the CMC with recorded EMG of lower limb muscles in healthy participants walking at different speeds. Neither the SO nor the CMC results were found consistent with the EMGs.

It is still a limitation or challenge to build proper muscle model that could help get sufficient agreement between recorded muscles EMG and estimated values. Although the muscle properties such as pennation angle, maximum isometric force, tendon slack length and optimal fibre length were scaled with the skeleton through the scaling tool, the agreement between patient-specific and scaled ones is still not known so far. Customised muscle properties might help much more accurate results of forces and activations, but in terms of measurement of those parameters it is still challenging and time-consuming, especially for clinical applications.

4.7 Joint reaction analysis

To reduce the computational cost in the next stage of dynamic FE simulations, instead of building the whole lower limb along with applying ground reaction forces on the foot, obtaining the joint reaction loads on the hip and ankle joints from OpenSim are more of our concerns. Therefore, a joint reaction analysis provided by OpenSim was performed by tracking the motion result from the RRA under the effects of muscle forces and controls from the SO. In this study, three translational (S-I, M-L, and A-P) forces and two rotational (dorsi-planar flexion and I-E) torques on the ankle joint are extracted for the dynamic FE simulations and will be applied on the tibia bone. The results of these loads are expressed in the ankle joint CS and shown in Figure 4. 12. The A-A torque will not be included in the following dynamic FE simulations, because it will increase the convergence difficulty in keeping both medial and lateral tibiofemoral condyles in

contact during the squat motion simulations. It will also increase the computational cost, since the adductor muscles across the hips joints will have to be added with the functionality to actively control and balance the adduction-abduction moment on the knee joint.
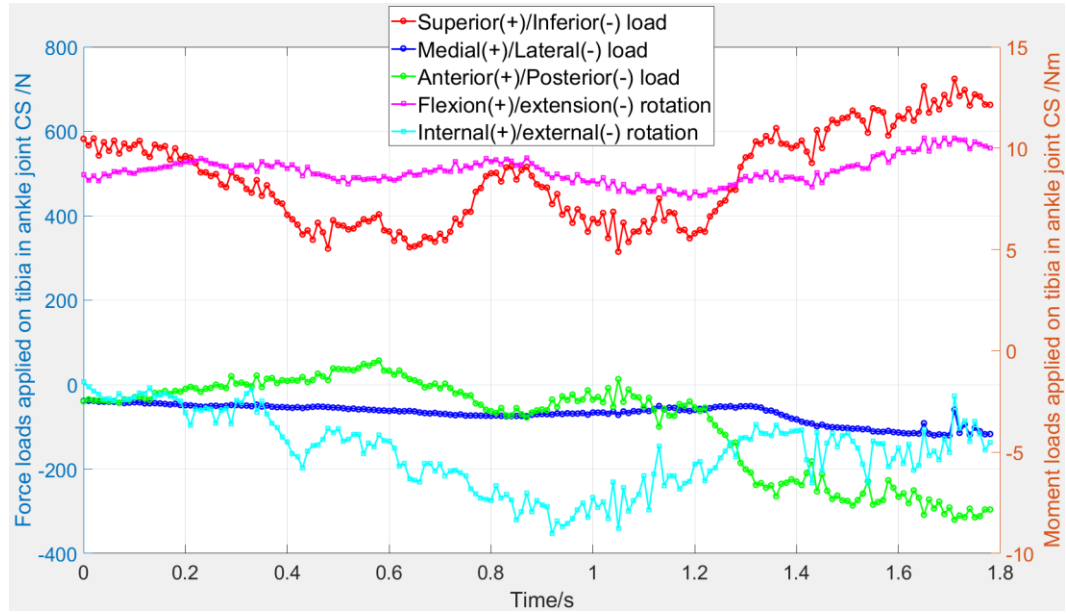
Figure 4. 12 Loads applied on tibia in ankle joint CS (superior-inferior force, medial-lateral force, anterior-posterior force, flexion-extension moment and internal-external moment)

4.8 Discussions and conclusion

In this chapter, the muscle forces of the patient-specific lower limb were obtained through the simulations of the patient-specific musculoskeletal model. Although the accuracy of these muscle forces is still challenging to validate in an experimental way, the muscle activation patterns for performing a daily activity can be compared with the EMG measurement results. This can help find out the approximate contributions or involvements of muscle bundles into the desired activities. Considering the magnitudes and patterns of major muscle activations in this study are generally consistent with either their corresponding EMGs [14,117] or those referenced from literature [121], the muscle forces will be applied on the next-stage dynamic FE analysis in the following chapters as closer-to-physiological internal forces for driving the squatting motion of the lower limb of subject JW.

Neither patellar ligament nor collateral ligaments were considered in the musculoskeletal model, because ligament structure is regarded as an external element in

OpenSim. Its passive stretching during the motion could result in larger calculated joint reaction forces and muscle forces. In order to avoid introducing too many variables and in the context of lack of patient-specific muscle parameters, the generic musculoskeletal model 2392 with default muscle parameter setting was used for scaling. This would inevitably produce a certain amount of error. Therefore, the pattern of muscle forces we calculated are only one of numerous possible solutions rather than absolute result that the subject muscles can produce. Compared to the simplified quadriceps loads and constant hamstring load used in the previous studies [43, 50, 52] of knee simulators, the muscle forces calculated in this study are apparently more patient-specific to investigate the direct dynamic responses of CTKI in much closer-to-physiological condition.

Apart from the patient-specific muscle forces, the patient-specific ankle joint loads were also calculated and will be imported into the FE dynamic model for simulating patient-specific loads rather than the standardised loads commonly used for wear tests [53, 54, 103]. The joint reaction forces are dependent on the lower limb lengths, locations of joint centres and body weight of each individual. Therefore, the patient-specific joint reaction forces rather than standardised experimental loads should be applied to test the dynamic responses of patient-specific TKR implants.

The OpenSim musculoskeletal model could help quickly calculate a set of muscle forces and joint reaction loads which could be further used to investigate their effect on the human natural or implanted joints. Incorporating the effect of active muscles into the performance evaluation of TKR implants could help make simulations or experimental tests much closer to the realistic physical and physiological environment, and assist with the design of TKR implants for further improving the functionality of patient knee joints. Only by taking into account the influence of patient-specific lower limb muscles and joint reaction forces could a customised TKR implant be tested to help recover a specific patient knee to its normal mobility and functions, in the meantime, the reliability and longevity of the artificial components could be guaranteed for alleviating the pain after the TKR surgeries or reducing the need for the revision surgeries.

Chapter 5

ANSYS dynamic finite element modelling for assessing the dynamic performance of the total knee implants

5.1 Introduction

For evaluating or predicting the performance of total knee implant of various designs, many simulations and in-vitro experiments have been conducted. Shi [108] used quasi-static method to test implants under different knee flexion angles, Godest [57] and Fitzpatrick [59] analysed the dynamic responses of knee implant components by applying lower extremity kinematics on the local axes of FE models. In the above studies, the flexion-extension (F-E) axis that tibial implant rotates around femur could be easily determined before motion analysis or performance evaluation, since the traditional off-the-shelf designs of femoral implant [65, 124–126] are usually accompanied with two parallel regular-shaped femoral condyles, and either single distal femoral radius or multiple gradually changing femoral radii in the sagittal plane. However, normally the actual F-E axis of knee joint could not be consistent with the rotation axis set on the artificial components. Many researchers [132–137] have studied the transepicondylar axis and cylindrical axis or compared them as the surrogates of the knee F-E axis based on the magnetic resonance imaging (MRI) technology. Neither transepicondylar axis nor cylindrical axis were found to be in line with the instant flexion-extension axis. Since there is no fixed rotation axis or known kinematic data to help correctly locate tibia relative to femur at each time interval of motion, a knee simulator considering hip and ankle joints needs to be built in order to test the dynamic performance of customised knee implants, which were designed in anatomical way in this study.

Among the knee simulators, the Oxford knee rig (OKI) [41, 42] was used and further improved for not only testing various knee arthroplasties but also cadaveric knee joint. Derived from it, several test rigs [43, 133, 134] with different loadings, boundary conditions were proposed and designed. Verstraete et al. [55] proposed an improved knee simulator which allowed the ankle joint to move vertically and horizontally. A servomotor was used to apply a time-varying quadriceps force on a knee joint, while a hamstring force was represented by attaching a constant mass to a pulley system. Based on the Purdue

Knee [140], Maletsky and Hillberry [45, 46] designed a five-axis simulator named Purdue Knee Simulator: Mark II, from which the Kansas knee simulator (KKS) [47–51, 136] was built for studying the biomechanical performance of knee implants. Baldwin et al. [53] used ABAQUS/Explicit to build a FE model of KKS that considered not only the specimen-specific bone and implanted components but also the quadriceps tendon and ligaments around the knee.

In this study, different from loading conditions of any other knee simulators, three translational and two rotational loads that were calculated based on the squatting ground reaction forces were applied on the ankle joint with all six DOFs, meanwhile, a function of angular displacement versus time was applied on hip joint. The ankle joint was specified to have all six DOFs, while the hip joint was only allowed two rotational DOFs. The translational DOFs of hip joint were fixed to the ground as that in the knee simulator developed by Verstraete et al. [55], but it is different from both OKI [46] and KKS [53] where a constant vertical hip load was applied. In reality, the hamstrings muscle forces vary with time as quadriceps muscle forces do during daily activities instead of being simplified as a constant force [55]. Accordingly, the effect of not only quadriceps forces but also time-varying hamstrings and tibial muscle forces were taken into account in this study. Apart from that, the effect of muscle wrapping when knee flexes to a certain angle, nonlinear mechanical property of ligaments, gravitational and inertial effect were all included in this model.

5.2 Creation of joint coordinate systems in ANSYS FE knee simulation model

Because only the CT images near the subject knee joint are available from the online source [14, 117] for building the 3D knee model, the lower limb model in Figure 5. 1 that is from OpenSim musculoskeletal model in Chapter 4 is used to display the coordinate systems (CSs) of lower limb joints. Those CSs will be correspondingly created in the dynamic FE knee simulation model in this chapter for building muscle insertion points and applying joint reaction loads.
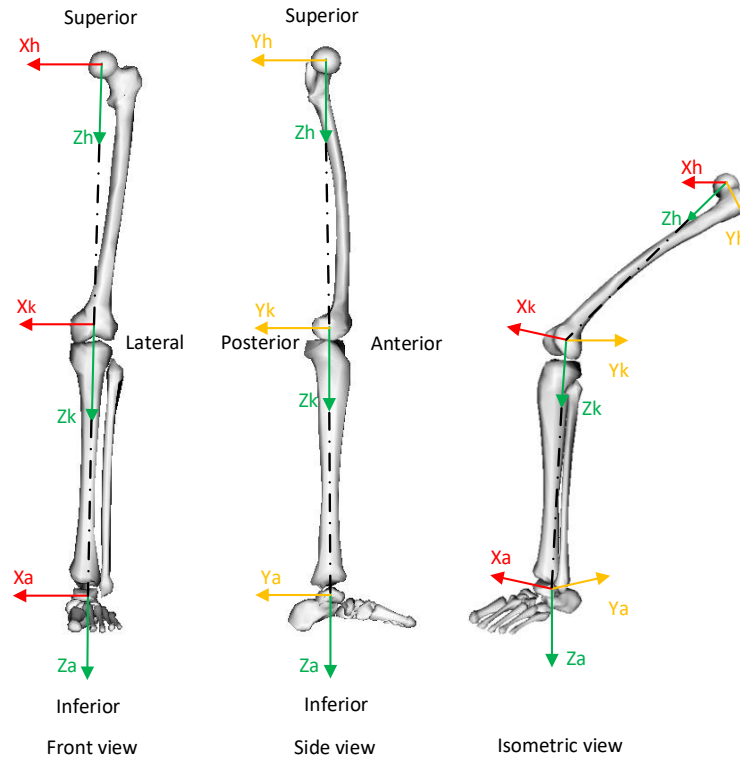
Figure 5. 1 Schematic diagram of coordinate systems of joints in the OpenSim lower limb model that will be created in the ANSYS FE knee simulation model

Those joint CSs in Figure 5. 1 were determined according to the bony landmarks. Firstly, epicondylar points were selected from the medial and lateral prominences of the distal femur. Then, the centre of femur distal could be determined by locating it between medial and lateral epicondylar points. The connecting line between these two points was the X-axis along which the femoral component could move mediolaterally in relation to the tibial component. The hip joint centre point in ANSYS was determined from the relative location between the femur central point and hip joint centre in the femoral CS of the patient-specific musculoskeletal model ([14, 117], subject JW, mass: 66.7 kg, height 1.68m) in OpenSim. Connecting the hip joint centre with the femur centre point was the Z-axis for the femur mechanical axis along which was also the superior-inferior view of femoral component. The Y-axis of femoral component is perpendicular to the X-axis and Z-axis and pointed to the posterior side of femoral component. The X-axis of hip joint which was located in the femur head centre was parallel to the X-axis of femoral implant component. The axis perpendicular to the X-axis and Z-axis was the Y-axis along which the femoral component could move posteriorly in relation to the tibial counterpart. The origin and local coordinate axes for the tibial component were built in coincidence with the ones for the femoral counterpart. In ANSYS FE model, the femoral

origin and points for reference axes were rigidly connected with four points on the femoral component as massless rigid links, which allowed the local frame to move simultaneously with femoral component without any deflection. The connection method was also applied for the tibial local frame. The local CS of ankle joint was also determined from the relative positions between knee and ankle joints in the musculoskeletal model. Its Z-axis was pointed from the ankle joint centre to the knee counterpart.

5.3 Joint definitions and boundary conditions in ANSYS FE knee simulation model
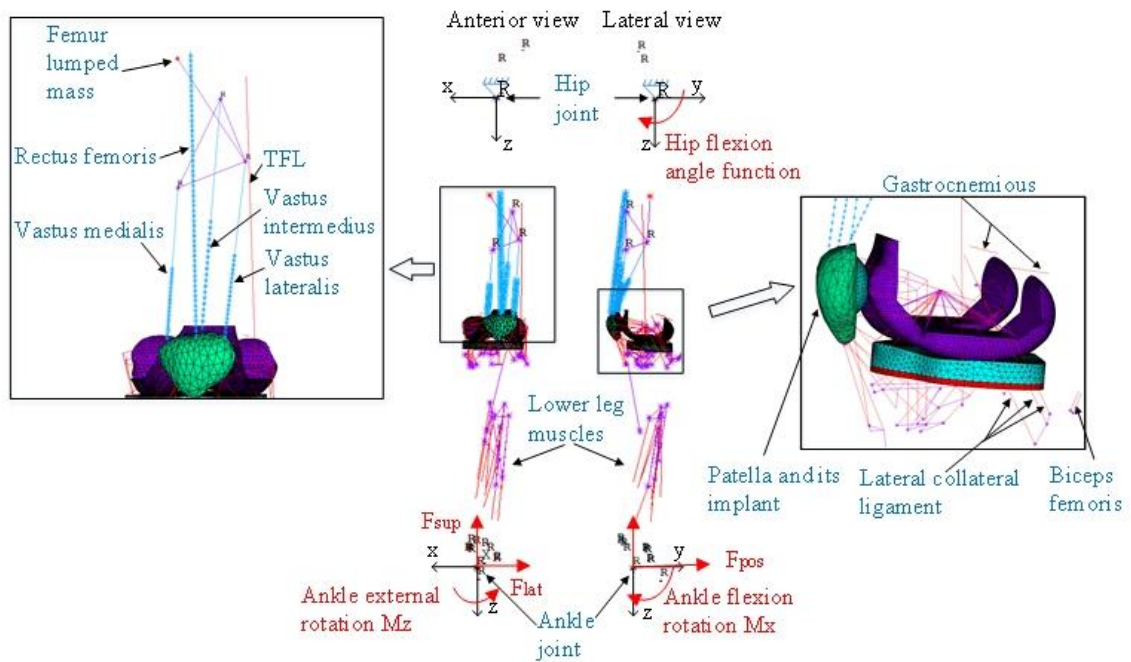
Figure 5. 2 Joints and boundary conditions in the dynamic FE knee simulation model

ANSYS MPC184 Joint elements were used to create hip and ankle joint of the subject lower limb. In Figure 5. 2, the hip joint was specified to have two rotational DOFs which allowed flexion-extension (F-E) and abduction-adduction (A-A) motions, while the ankle joint was created as a ball joint that allowed the tibial F-E, A-A and internal-external (I-E) rotations around the talus bone. All six DOFs of Knee joint were set unconstrained but restricted by the implant geometries and the effect of ligaments, musculotendons and the patella. As shown in Figure 5. 3, apart from the flexion rotation, the tibiofemoral joint has other five motion DOFs which consist of A-A rotation, I-E rotation, medial-lateral (M-L) translation, anterior-posterior (A-P) translation and superior-inferior (S-I) translation.
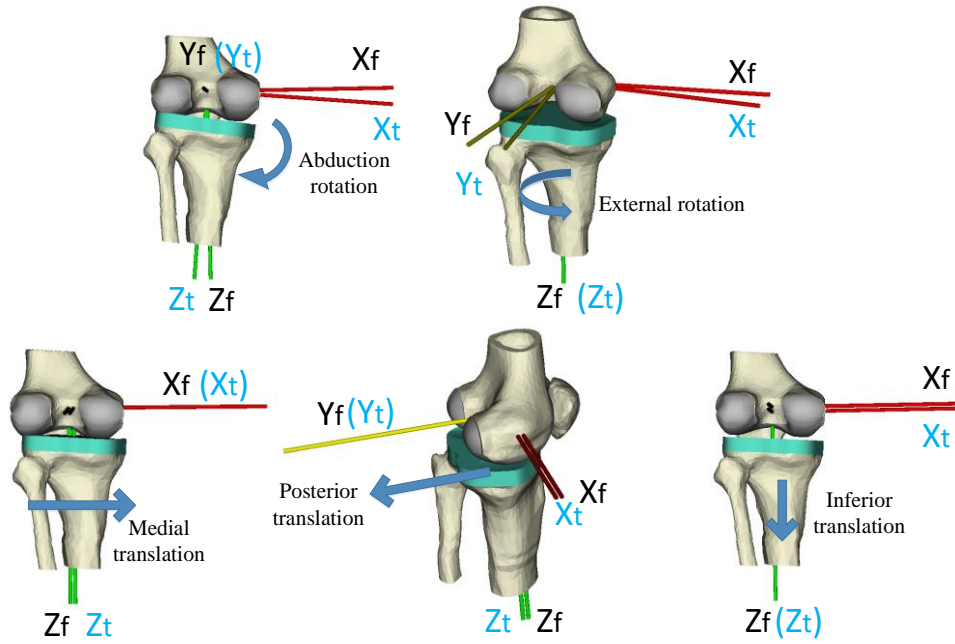
Figure 5. 3 Schematic diagram of tibiofemoral relative motions by using OpenSim model

The hip flexion rotation was controlled by a function of rotation angles versus time obtained from the OpenSim patient-specific musculoskeletal model in Chapter 4, while the ankle joint was applied with three translational forces and two torques which were also calculated from the OpenSim model. The A-A torques on both hip and ankle joints were neglected in case of the system imbalance in the frontal plane. Due to lack of muscle control mechanism in this dynamic FE model, applying A-A torques on both hip and ankle joints could cause single-side-condylar lift-off from contact during the simulation processes.

5.4 Ligament and musculotendon models

To provide stability in the knee joint motions, several knee joint ligaments were created based on knee anatomy, such as patellofemoral ligament in Figure 5. 4(a), retinaculum and patellar ligament in Figure 5. 4(b). Two collateral ligaments (CLLs) in Figure 5. 4(c) and (d): lateral collateral ligament (LCL) and medial collateral ligament (MCL) and two cruciate ligaments (CLs) in Figure 5. 5: anterior cruciate (ACL) and posterior cruciate (PCL) were built as nonlinear springs with insertion points on the femur and tibia respectively, while the patellar ligament (PL) was regarded as three linear springs due to the lack of relevant literatures. Based on the stiffness of PL of 210±66 N/mm in literature [142], the PL was split into three bundles with the same stiffness of 70 N/mm. The ligaments except PL in this model were modelled as nonlinear springs with preloads

as reported in literature [54, 80, 82]. The force-displacement curve for the ligaments was described by Eq. 5-1 and Eq. 5-2. The variable ε is the ligament spring strain. The parameter k is the stiffness parameter, l_0 is the zero-load length and ε_l is the spring parameter assumed to be 0.03 [143]. In order to ensure the model stability in initial state, the preloads or initial strains were added with specific spring stiffness parameters as shown in Table 5. 1. In Chapter 6, three different treatment scenarios of CL including retaining CLs, removing ACL and removing both CLs during surgery were simulated from the knee extension posture to the maximum knee flexion angle during a squat. Forces and elongations of all the ligaments were extracted for analysis.
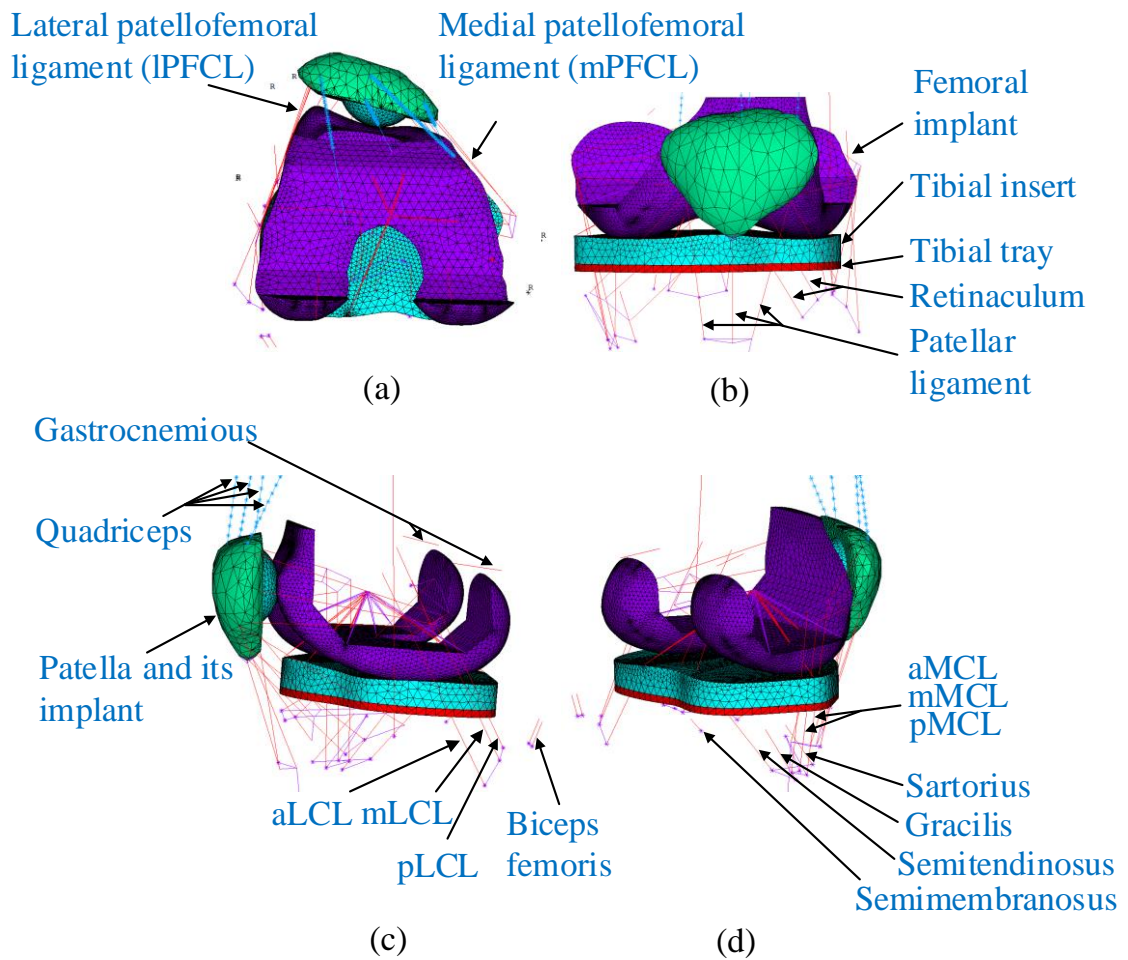
Figure 5. 4 Musculotendons and ligaments in dynamic FE model: (a) top view; (b) front view; (c) lateral side view; (d) medial side view
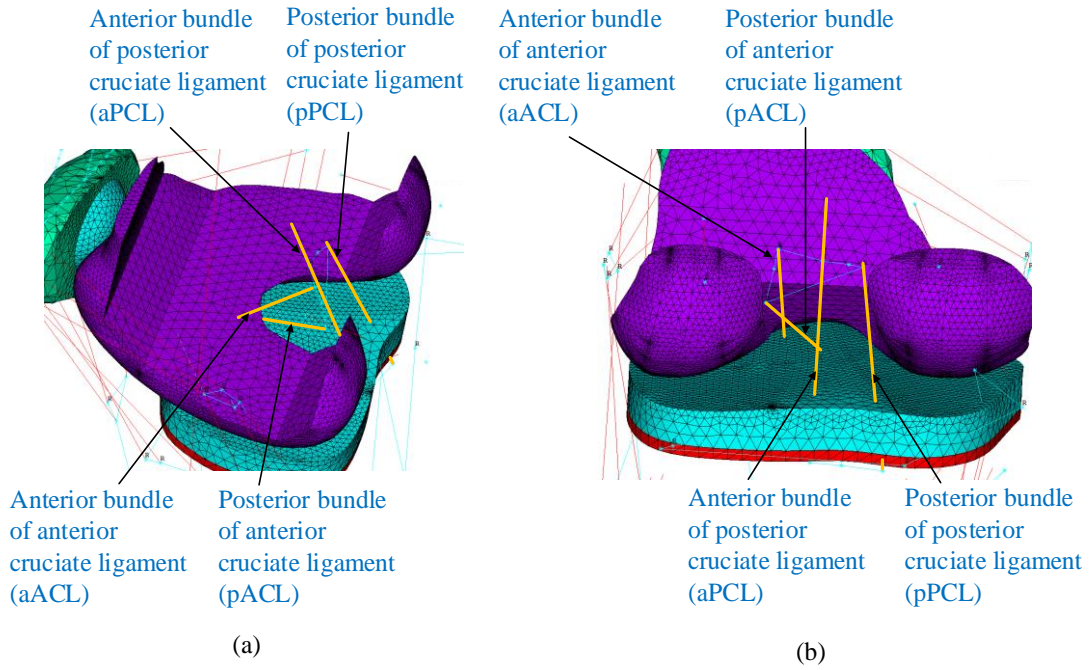
Figure 5. 5 Cruciate ligaments (without corresponding design features such as fenestration in the tibial insert to let cruciate ligaments through) in dynamic FE model: (a) lateral side view; (b) posterior view

$$F = \begin{cases} \dfrac{1}{4}k\varepsilon^2/\varepsilon_l & 0 \leq \varepsilon \leq 2\varepsilon_l \\ k(\varepsilon - \varepsilon_l) & \varepsilon > 2\varepsilon_l \\ 0 & \varepsilon < 0 \end{cases} \tag{5-1}$$

$$\varepsilon = \frac{l - l_0}{l_0} \tag{5-2}$$

Table 5. 1 Collateral ligament stiffness parameters and reference strains [80,82]

Ligament bundle	aLCL	mLCL	pLCL	aMCL	mMCL
Ligament stiffness parameter (N)	2000	2000	2000	2750	2750
Reference strain/ initial spring strain	-0.25	-0.05	0.08	0.04	0.04
Ligament bundle	pMCL	aPCL	pPCL	aACL	pACL
Ligament stiffness parameter (N)	2750	9000	9000	5000	5000
Reference strain/ initial spring strain	0.03	-0.24	-0.03	0.06	0.1

Both the patellofemoral collateral ligaments (PFCLs) and the retinaculum ligaments (RLs) shown in Figure 5. 4(a) and (b) were modelled as nonlinear springs of the same

expression of force-displacement curve as those of the knee collateral ligaments. Their stiffness parameters and initial spring strains are shown in Table 5. 2. In this table, mPFCL, lPFCL denote the medial and lateral side bundles of PFCLs; mRLs, lRLs mean the superior bundles on medial and lateral side of RLs; mRLm, lRLm are the middle bundles in medial and lateral side of RLs; mRLi, lRLi represent the inferior bundles in medial and lateral side of RLs. All these values are assumed due to lack of literature on them. Smaller values of initial spring strains of PFCLs will be simulated in Chapter 8 to investigate the effect of ligament laxities on the kinematics and kinetics of patellofemoral joint.

Table 5. 2 Stiffness parameters and pre-strains of patellar collateral ligaments and retinaculum ligaments

Ligament bundle	mPFCL	lPFCL	mRLs	mRLm
Ligament stiffness parameter (N)	2000	2000	2000	2000
Reference strain/ initial spring strain	0.1	0.1	0.005	0.01
Ligament bundle	mRLi	lRLs	lRLm	lRLi
Ligament stiffness parameter (N)	2000	2000	2000	2000
Reference strain/ initial spring strain	0.01	0.02	0.01	0.01
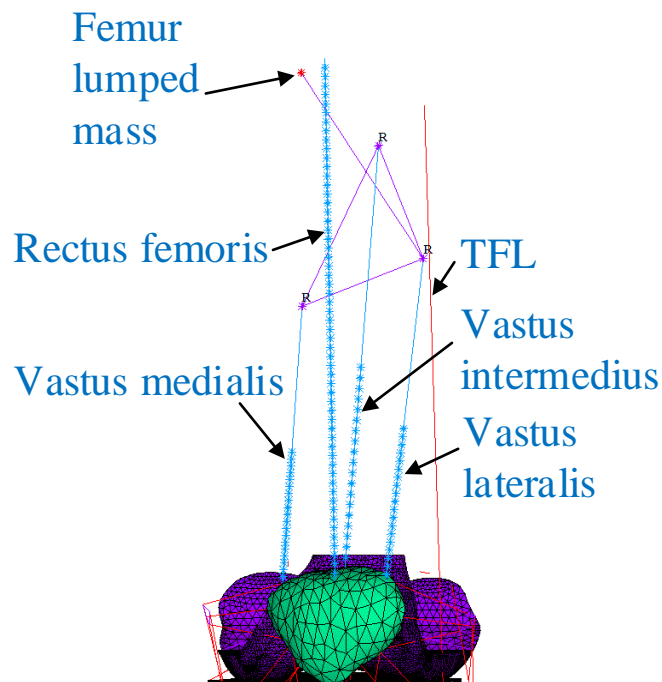
Figure 5. 6 Bundles of Quadriceps and lumped mass of femur bone
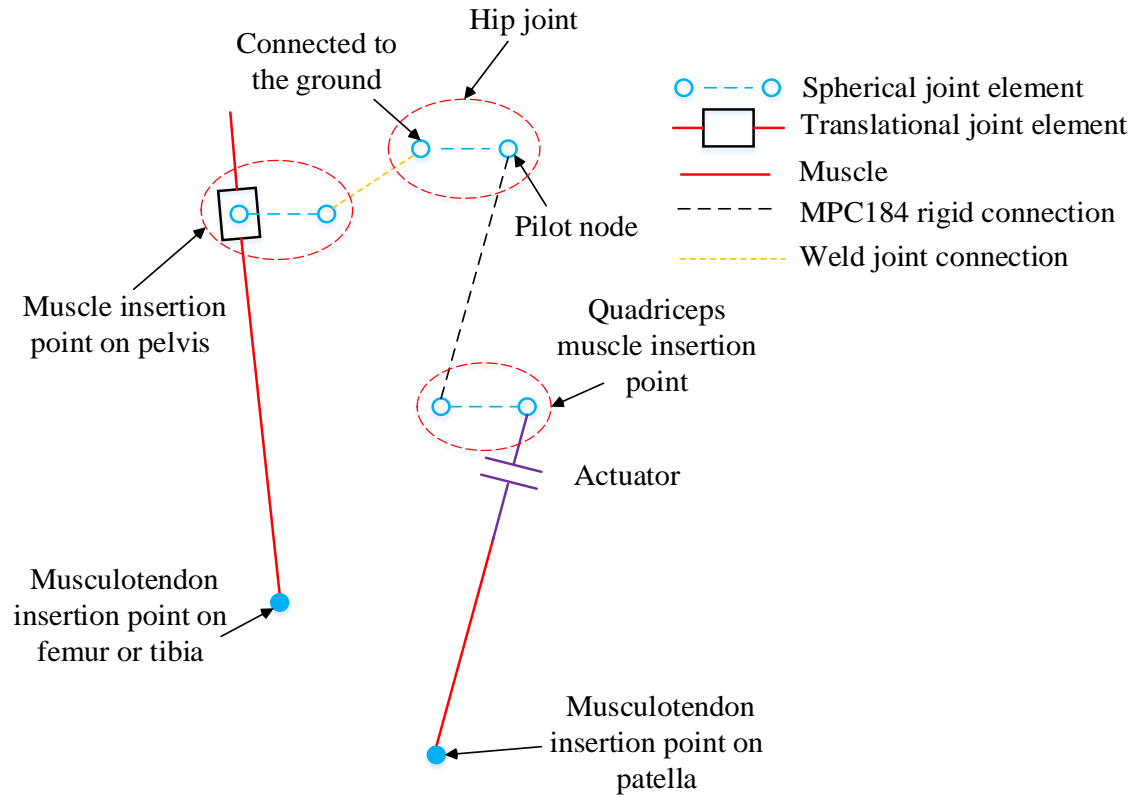
Figure 5. 7 Schematic representation of connection definitions

As shown in Figure 5. 6, the quadriceps muscles were split into four bundles with three muscle insertion points on the femur and one on pelvis. Because only some segments of femur and tibia could be built from the accessible CT data, the locations of the four muscle insertion points on either femur bone or pelvis bone could only be determined from the OpenSim musculoskeletal model ([14], subject JW, mass: 66.7 kg, height 1.68m) in the local coordinate system of hip joint. All the muscle insertion points on femur bone are rigidly connected to the point in the hip joint origin that acts as pilot node through the multipoint constraint (MPC) technology (see Figure 5. 7), while other all muscle insertion points on tibia bone are connected to the pilot node in ankle joint origin. Because some muscles around the knee joint are attached to pelvis or calcaneus which is not built in this FE model, the insertion points on pelvis or calcaneus were built as a translational joint with an ability to rotate around a spherical joint (see Figure 5. 7). This allows the time-varying muscle force to be only loaded on the knee joint components and adjust its spatial vector direction by its own, and at the meantime, go through the insertion points on pelvis or calcaneus without producing extra loads on the hip or ankle joint. Each spherical joint node that is in the location of each muscle insertion point and meanwhile connected with the translational joint is rigidly connected to the pilot node

in either hip joint or ankle joint thorough weld joint (see Figure 5. 7).

For the three quadriceps muscle bundles (vastus medialis (VM), vastus lateralis (VL) and vastus intermedius (VI)) that connect femur bone and patella, in order to make the knee joint under compression state, the patella should be pulled along the direction of quadriceps muscle bundles while the muscle bundles are activated. Therefore, an actuator element in Figure 5. 7, Link11, was applied to the above three quadriceps muscle bundles. This element supports the import of force-time function and applies time-varying load on the axial direction of muscle bundle. On two ends of each actuator are each muscle bundle and spherical joint node. The femur and tibia bones were deleted before the dynamic analysis for the purpose of reducing the computational cost.

Since ANSYS Mechanical APDL 18.2 does not support preload on the nonlinear spring element Combin39 at the moment, the first load step is applied, where the motion of femur and tibia are temporarily constrained, and the ligament could move in a length of deflection depending on the ligament spring initial strain. Notably, when the Combin39 element is in compression state, it is set to be zero force produced. For the mechanism of ligament translation motion, a translation joint rotating around a spherical joint is also applied as can be seen in Figure 5. 7. Through defining the node-to-node contact pair with element Conta178, once the moving end node of spring reach the location of one spherical joint node, these two nodes will be attached without separation in the following load steps. Another node of the spherical joint is rigidly connected to the hip joint node which is the pilot node and will control the former node to rotate with it.

Due to the limited functionality in ANSYS, control loop or feedback was not used to control or adjust either muscle forces or joint loads in the dynamic FE simulations of this whole thesis.

5.5 Muscle wrapping effect

When it comes to deep knee flexion, the quadriceps muscle should normally wrap around the distal femur. In ANSYS, if without any setting, the elements which represent musculotendon will pass through the femur bone dragging the patella upward to the hip joint direction. Hence, the node-to-surface contact (element Conta175) is adopted to

simulate the muscle wrapping effect with considering the effect of friction coefficient in Table 5. 3 in Section 5.7. The muscle attachment points on the femur and pelvis are known and referenced from the OpenSim model (4th grand competition to predict knee joint load). Since the quadriceps muscle is split into four bundles, namely rectus femoris, vastus lateralis, vastus medialis and vastus intermedius, each bundle can be linearly divided into N segments with each spring stiffness (element Combin14) equivalent to Ks*N (Ks: the stiffness of one bundle before discretization). Here we set the spring stiffness of each string of the quadriceps muscle to be 15 N/mm (15-24N/mm for the stiffness of quadriceps in literature [142]).
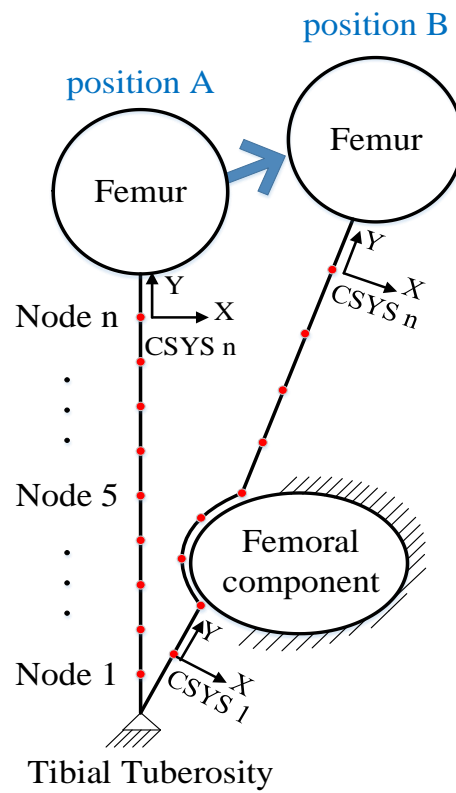
Figure 5. 8 Discretization of quadriceps muscles for contact with femoral component

Since one single muscle string (e.g. rectus femoris) was discretized into (N+1) elastic springs, there would be one node produced on each end of pre-discretized spring and other N node points in between. For instance, in Figure 5. 8, the two objects are assumed to be one tibia with its bone tuberosity fully fixed and one femur moving from position A to position B. Each spring element node is built in its local reference frame. In each local frame, its Y axis is set toward the axial direction of each spring element while X axis perpendicular to it. Z axis is pointed outside from the X-Y plane. Once the spring

node contacts a surface (e.g. femoral component in Figure 5. 8) during its moving course, each spring element could only deflect in the X-Y plane in case nodes of one single muscle string randomly vibrate in Z direction. Therefore, a set of coupling equations are used to constrain those nodes' DOFs in Y and Z directions in Eq. 5-3.

$$\begin{cases} \Delta_{NYi} = \Delta_{NYi-1} = NY(i+1) - NY(i) = NY(i) - NY(i-1) \\ \Delta_{NZi} = \Delta_{NZi-1} = NZ(i+1) - NZ(i) = NZ(i) - NZ(i-1) \end{cases}, i=1,2\sim n \qquad (5\text{-}3)$$

Transformed into the form in Eq. 5-4:

$$\begin{cases} NY(i+1) - 2NY(i) + NY(i-1) = 0 \\ NZ(i+1) - 2NZ(i) + NZ(i-1) = 0 \end{cases}, i=1,2\sim n \qquad (5\text{-}4)$$

As shown in Figure 5. 9, with the relative motion between femur and tibia bones that were replaced with ANSYS MPC184 rigid connection element, the bundles of quadriceps muscle came into contact with the femoral component from low knee flexion angle to a high knee flexion angle. The muscle bundles can be seen wrapping around the external curve surface of femoral component. It is more precise for describing the scenario of muscle wrapping bone than other methods such as cylindrical envelope surface in some OpenSim models. The latter method only considers single DOF of flexion rotation of patellofemoral joint, which cannot comprehensively describe equally complicated patellofemoral motions as the tibiofemoral motions.

(a)

(b)
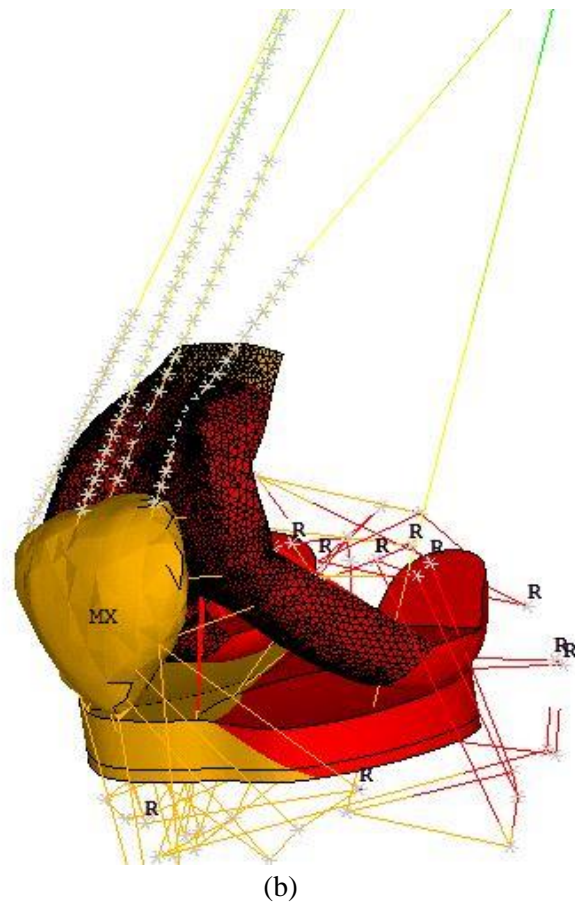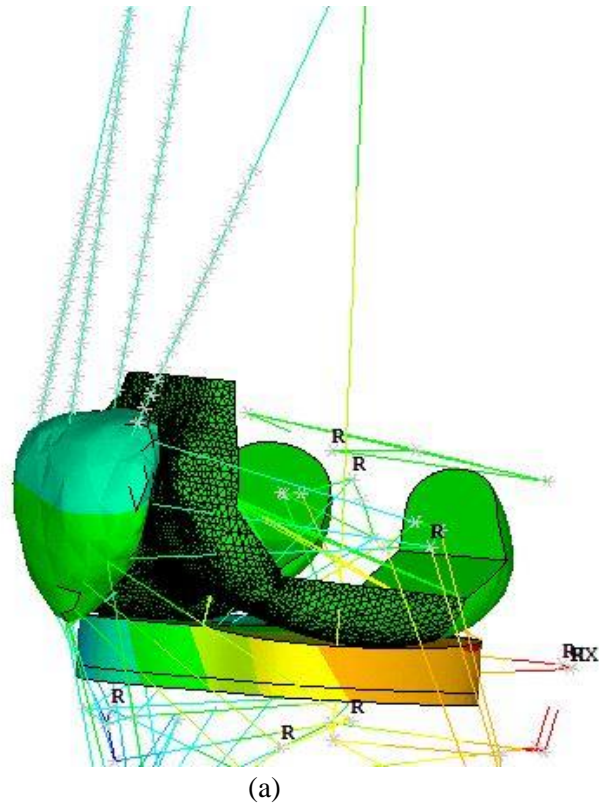
Figure 5. 9 Effect of quadriceps wrapping around femoral component from (a) the low knee

flexion to (b) the high knee flexion

5.6 Measurement of two relative moving objects

(a)

(b)
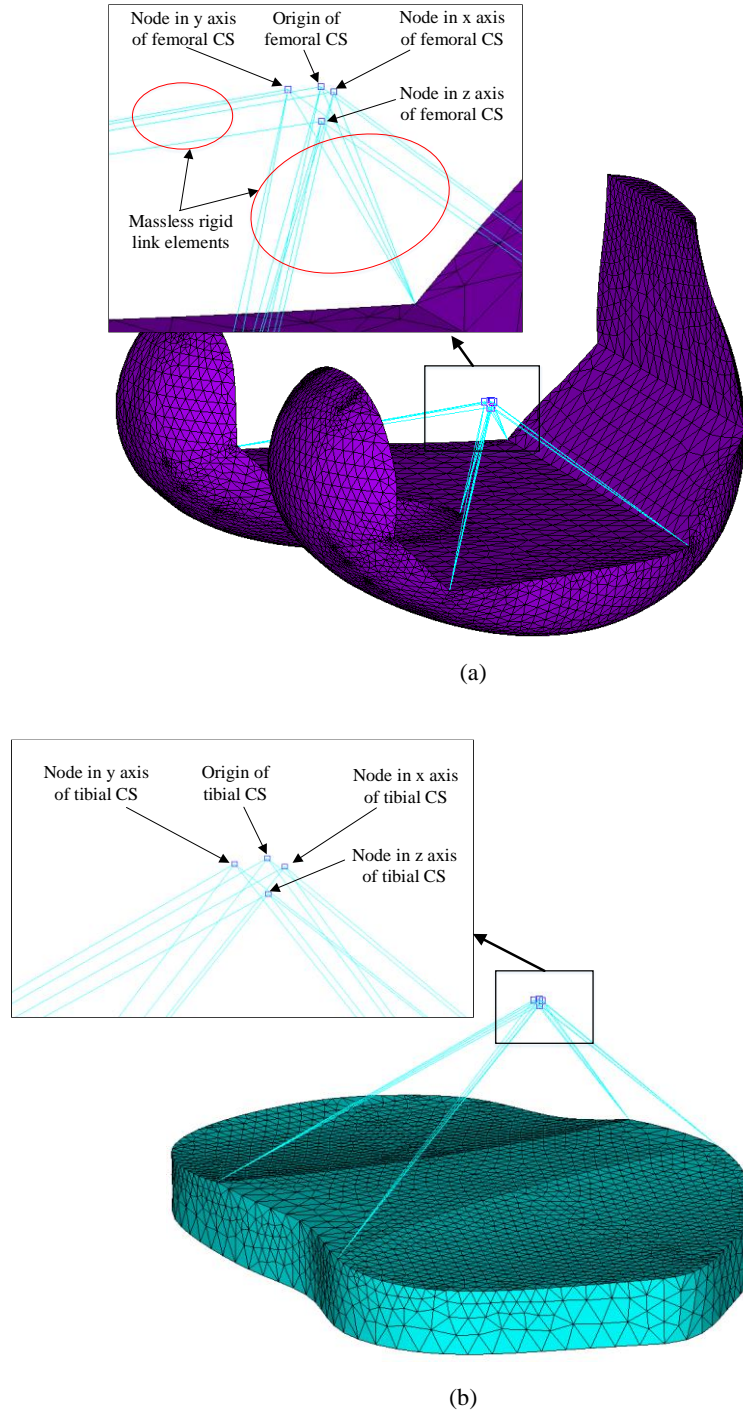
Figure 5. 10 Coordinate systems of (a) femoral component and (b) tibial insert

A rotation matrix [144] was applied to calculate the relative rotations or Euler angles between femoral and tibial local coordinate systems (CS). As shown in Figure 5. 10, each CS was built through creating four nodes and then connecting them with five nodes on the implant installation surface via massless rigid link elements. Relative rigid

translations could be calculated through the distances between femoral and tibial CS origins. Both rotations and translations were expressed in tibial CS as well as two condylar compressive forces in the vertical direction of tibial CS.

5.6.1 Relative rotations of two moving objects

Since the two local reference frames move with two corresponding implants, the relative rigid body rotations can be obtained via solving the Euler angles between two CSs in Eqs. 5-5 and 5-55-55-6. In Figure 5. 11, e_{ti}, e_{fj} (i, j=x, y, z) are the unit vectors in the tibial and femoral local frames respectively. The tibial CS is regarded as the fixed CS, while the femoral CS is rotating in relation with the tibial CS. The matrix in Eq. 5-5 is the transformation matrix made of direction cosines [145].
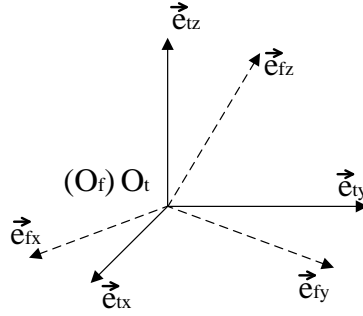
Figure 5. 11 rotation between two coordinate systems

$$\begin{pmatrix} e_{fx} \\ e_{fy} \\ e_{fz} \end{pmatrix} = \begin{Bmatrix} Q_{xx} & Q_{yx} & Q_{zx} \\ Q_{xy} & Q_{yy} & Q_{zy} \\ Q_{xz} & Q_{yz} & Q_{zz} \end{Bmatrix} \begin{pmatrix} e_{tx} \\ e_{ty} \\ e_{tz} \end{pmatrix}, Q_{ij} = \cos(e_{ti}, e_{fj}) = e_{ti} \cdot e_{fj} \qquad (5\text{-}5)$$

$$\begin{cases} \theta_x = \tan^{-1}(Q_{zy}/Q_{zz}) \\ \theta_y = \tan^{-1}\left(-Q_{zx}/\sqrt{Q_{zy}{}^2 + Q_{zz}{}^2}\right) \\ \theta_z = \tan^{-1}(Q_{yx}/Q_{xx}) \end{cases} \qquad (5\text{-}6)$$

Through solving the Eq. 5-6 which was referenced from the literature [144], $(\theta_x, \theta_y, \theta_z)$ are obtained and sequentially present the rotation angle around the tibial x axis that corresponds the knee flexion-extension rotation angle, the rotation angle around the tibial y axis that corresponds the knee abduction-adduction rotation angle and the rotation angle around the tibial z axis that corresponds the knee internal-external rotation angle.

5.6.2 Relative rigid translations of two moving objects

The relative rigid displacements between femoral and tibial components can be obtained from a simple triangulation calculation. In Figure 5. 12, $\vec{V}_{tf}$ is the distance vector between the tibial and femoral origins. As shown in Figure 5. 12, α is the angle between $\vec{V}_{tf}$ and e_{tx}; β is the angle between $\vec{V}_{tf}$ and e_{ty}; γ is the angle between $\vec{V}_{tf}$ and e_{tz}.
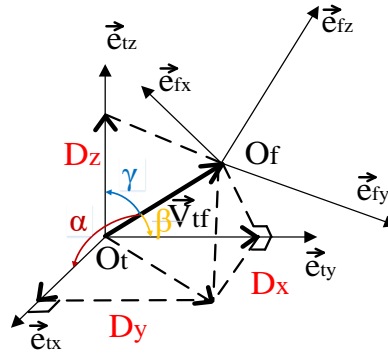
Figure 5. 12 Translation between two coordinate systems

$$\begin{cases} D_x = \left|\vec{V}_{tf}\right| \cdot \cos\alpha = \vec{V}_{tf} \cdot \vec{e}_{tx}/\left|\vec{e}_{tx}\right| \\ D_y = \left|\vec{V}_{tf}\right| \cdot \cos\beta = \vec{V}_{tf} \cdot \vec{e}_{ty}/\left|\vec{e}_{ty}\right| \\ D_z = \left|\vec{V}_{tf}\right| \cdot \cos\gamma = \vec{V}_{tf} \cdot \vec{e}_{tz}/\left|\vec{e}_{tz}\right| \end{cases} \tag{5-7}$$

(D_x, D_y, D_z) are medial-lateral translation, posterior-anterior translation and superior-inferior translation respectively.

5.7 Materials and solution convergence

In the solution of this chapter, all material properties of total knee implant components were set linear. As shown in Table 5. 3, the ultra-high molecular weight polyethylene (UHMWPE) is a common material for tibial inserts. The femoral implant is made of Cobalt-Chrome alloy. A titanium alloy is used for modelling the tibial tray of 3 mm thickness [108] in the simulations. No relative motion was assumed between the tibial insert and tibial tray. The patellar bone was assumed as cortical bone with constant elastic modulus.

Table 5. 3 Material property of total knee implant components [108]

	Elasticity modulus (MPa)	Poisson's ratio	Coefficient of friction	Density (kg/m^3)
UHMWPE	1016	0.46	0.04	0.945×10^3
Cobalt-Chrome alloy	193000	0.29	0.05	8.5×10^3
Titanium alloy	110000	0.33		4.4×10^3
Cortical bone	17580	0.3	0.8	1.85×10^3

In order to apply the initial strains or pretension forces of knee ligaments and make system reach an initial balance, three load steps were used in the simulations. In the first load step, the external-internal rotation of ankle joint was locked, and the patella was only allowed to F-E rotate, M-L tilt and S-I translate in relation to the femoral implant component. Three translational forces and the F-E moment calculated in the musculoskeletal model in Chapter 3 were applied on the ankle joint. The hip joint was applied with the function of flexion angle versus time obtained from the musculoskeletal model in Chapter 3 as well. Meanwhile, the pretension forces were also applied on ligament bundles. When the initial contact stresses were produced on the tibiofemoral and patellofemoral contact pairs and the pretension forces were applied on the knee joints at the simulation time of 0.02 seconds, those constraints on the patella were removed. At 0.04 seconds, a time-dependant function of external-internal torque from the OpenSim simulation in Chapter 4 section 4.7 was applied on the ankle joint.

In terms of the control load steps in the ANSYS iteration solver for the implicit dynamic problem, the maximum time-step was set to be 0.01 seconds and the minimum was 0.001 seconds. The automatic time stepping was also activated. These settings ensured that all the modes and responses of interest would be predicted.

The SOLID185 element was used to mesh the TKI models and patella. The element size of the contact surfaces of the tibiofemoral and patellofemoral joints was 2 mm. The element size for volume mesh was 4 mm. Mesh sensitivity was studied; further mesh refinement resulted in less than 5% change in the predicted peak contact pressures.

5.8 Conclusion

In this Chapter, a transient dynamic model was created based on the squatting mechanism of the OKR and the KKS. The hip joint was specified to only have the DOFs of flexion-extension, abduction-adduction rotations, while the ankle joint was allowed to move in all DOFs. The hip flexion angles were controlled by the rotation displacement result obtained from the OpenSim patient-specific musculoskeletal model, while the ankle joint was applied with three translational forces and two torques which were also calculated from the OpenSim model. It is worth noting that the adduction-abduction loadings on both hip and ankle joints were neglected in case the dynamic simulation loses balance in the frontal plane. Due to lack of muscle force self-adjustment in this dynamic finite element model, the dislocation of tibial component from the femoral counterpart would occur with only one side of condyles of knee joint in contact during the simulation processes.

Twenty-three muscles left lower limb were recruited with the referenced muscle insertion points from the OpenSim musculoskeletal model. The muscles on the upper leg were ignored for saving the computation cost. To provide dynamic balance, knee joint ligaments such as collateral ligaments and cruciate ligaments were also included in this model with their nonlinear spring stiffness and pre-strains referenced from the literatures. Actuator element in ANSYS Mechanical APDL was used to apply time-varying muscle forces to the quadriceps bundles connecting patella and femur, while a rotating-slider mechanism was to apply muscle forces to those muscles that are, only in one end, attached to either femur or tibia. The wrapping effect of the quadriceps bundles around the femoral component was created by discretizing the springs into several even segments of springs with several nodes. And then node-to-surface contact element was used to realize the wrapping effect when the knee joint flexes to a certain degree. Euler angles and rotation matrix were applied to track and record the relative motions between femur and tibia and between femur and patella. The material properties of the femoral component, tibial insert and tibial tray were set as linear for the consideration of computational cost and convergence difficulty.

Chapter 6

Dynamic simulation of knee joint during a subject-specific squatting motion

6.1 Introduction

In order to understand the relationship between knee joint motions and joint loads, many methods including experiments and simulations have been applied. Zhao et al. [146] collected the in-vivo medial and lateral tibial forces of subjects during motions of gait and step through the instrumented tibial tray. Mündermann et al. [147] calculated the maximum compressive loads and maximum medial-lateral load ratios based on in-vivo experimental tibial tray data. Taylor et al. [148] used motion capture markers and instrumented tibial tray to obtain not only the knee joint reaction forces but also the relative motions between femoral and tibial components under the motion trials such as squatting, level walking etc.. Bergman et al. [149] and Kutzner et al. [150] also measured the loads of total knee implants during different daily activities. Bersini et al. [62] built a multibody dynamic model by using a commercially available software (Working Model 3D, MSC) and calculated the forces between natural knee articulations, and the forces and lengths of knee joint ligaments. Stylianou et al. [151] used ADAMS and LifeMOD to perform the dynamic simulations of squatting motion and obtained the tibiofemoral forces and torques.

In addition to knee joint force measurements and calculations, the relative motion of total knee implants is also one of the concerns of many researchers. Wilson et al. [152] built an experiment rig to measure the relative tibiofemoral motions of cadaveric knees under passive knee flexion and coupled all tibiofemoral motions to the flexion rotations. Schmitz et al. [153] used OpenSim and discrete element knee model to conduct passive knee flexion and obtained the relative tibiofemoral motions. Murakami et al. [154] applied fluoroscopy and image-matching techniques to obtain the motion relationships between tibia and femur of healthy people during the motions of squat and golf swing. Later in 2018, Murakami et al. [7] used the same method to measure and compare the relative motions between healthy subjects and control subjects with bi-cruciate stabilized design which is with a traditional tibiofemoral contact surface. Tamaki et al. [155] used computer-

assisted design models to reproduce the spatial positions of femoral and tibial components from single-view fluoroscopic images and analysed an in-vivo kinematic pattern of a weight-bearing, deep-bending activity with a high-flexion, posterior stabilised, mobile bearing knee prosthesis. Bloemker et al. [54] built a 3D experiment rig of Kansas knee simulator by using Adams and calculated the relative motions of natural knee for gait analysis.

In this chapter, the dynamic knee simulation FE model created in Chapter 5 is used with applying patient-specific muscle forces and ankle joint reaction loads that were calculated during a squatting motion in Chapter 4. The tibiofemoral compressive forces and relative motions of both the CTKI and the STKI designs are calculated. For validation of the model, those results are compared with existing published research results. The forces and elongations of cruciate and collateral ligaments are also plotted and analysed under different ligament laxities.

6.2 Results

The relative motions between the femoral and tibial components are presented in Figure 6. 1. It is worth noting that, in Figure 6. 1(a), the results of femoral external rotation in relation to the tibia were in good agreement with that of five healthy males in-vivo measured by Murakami et al. [154] through fluoroscopic study. However, for the anteroposterior translation in Figure 6. 1(b), only the motion of CTKI with both CLs retained was close to that of healthy knees.

The STKI model simulated under the same conditions as the CTKI also showed constant femoral rotation but with a smaller ROM and paradoxical internal rotation. For its posterior translational motion, the femoral component slid 5 mm anteriorly on the tibial component until 30° knee flexion, and then moved posteriorly by 7 mm until the maximum knee flexion angle.
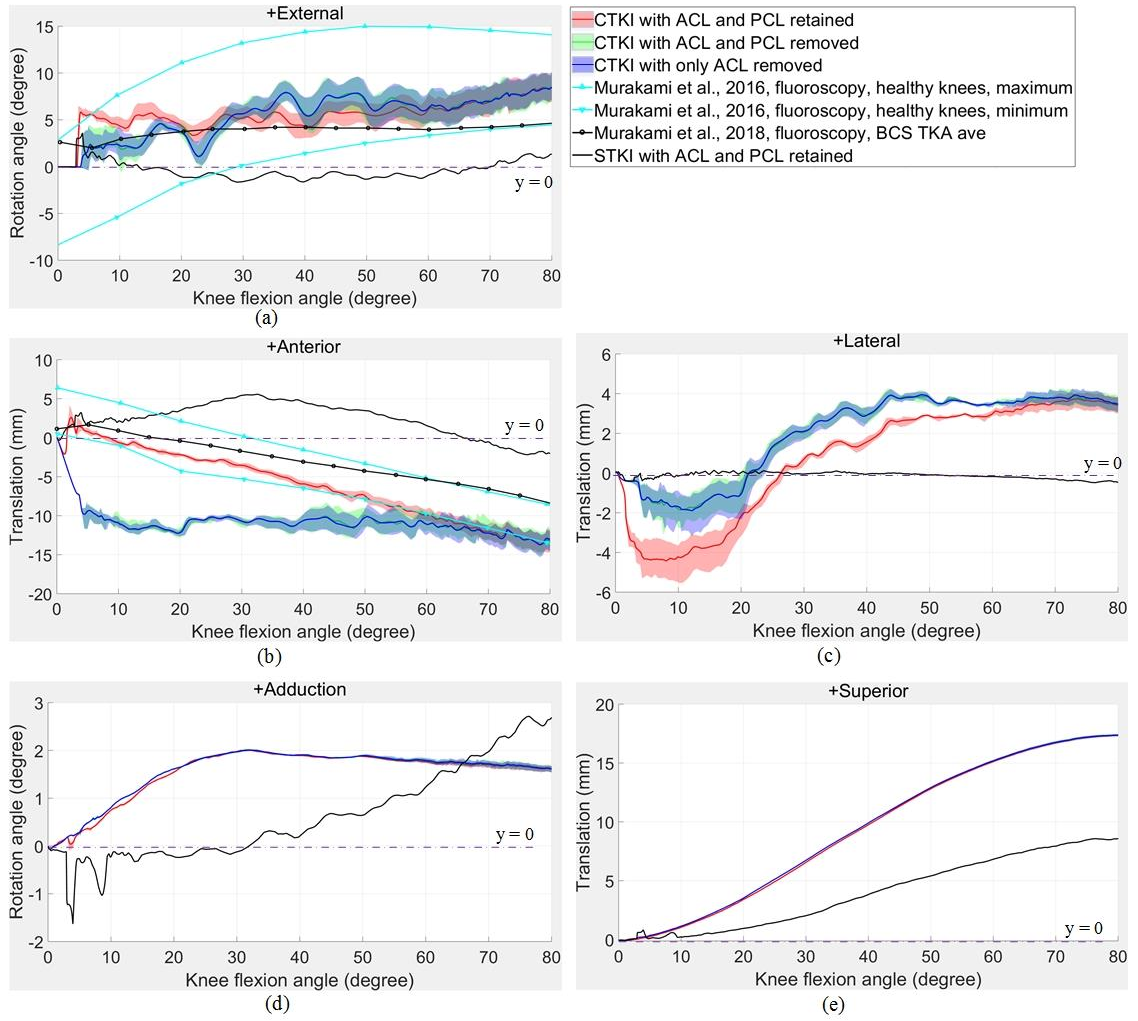
Figure 6. 1 Tibiofemoral relative motions: (a) and (b) comparisons of simulated external rotation and anterior translation with reported five healthy male knees which are shown in cyan triangle lines and implanted knees with bi-cruciate stabilized (BCS) design in black dot line. (c)～(e) medial-lateral translation, adduction-abduction rotation and superior-inferior translation. Shaded areas in red, green and blue are simulated results under different pre-strains of collateral ligaments: -50%, -20%, -10%, 10%, 20%, 50% of the reference strain in Table 5. 1.

As for the rest of the DOFs of the knee joint, the CTKI model did not show significant differences in the adduction-abduction rotation and superior-inferior translation among the three CL treatment scenarios. However, for the medial-lateral translation, the model with both CLs retained showed larger medial but smaller lateral translations. The femoral medial-lateral translation in the STKI in Figure 6. 1(c) remained constant. In Figure 6. 1(d), the STKI model resulted in a different trend for femoral adduction rotation to that of the CTKI. In Figure 6. 1(e), the femoral superior translation in STKI model was smaller than that of the CTKI.
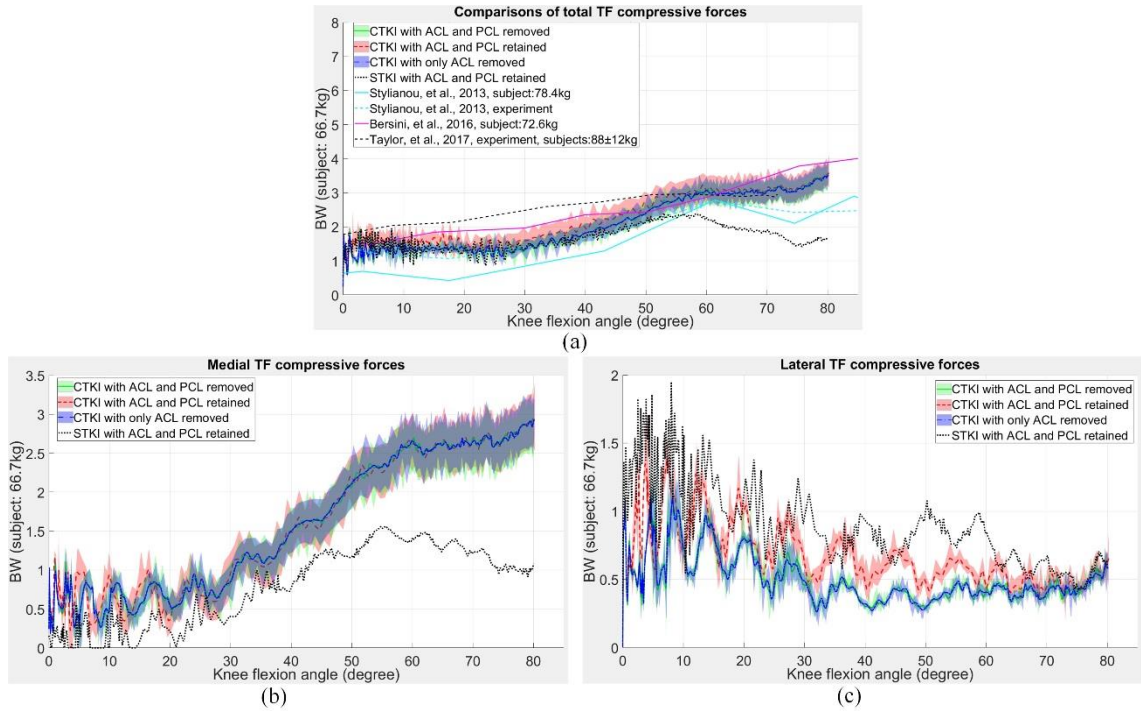
Figure 6. 2 Tibiofemoral (TF) compressive forces: (a) total condylar compressive forces including comparisons with other research findings; (b) medial and (c) lateral tibiofemoral contact forces. Shaded areas in red, green and blue were calculated and plotted under different pre-strains of collateral ligaments: -50%, -20%, -10%, 10%, 20%, 50% relative to the reference strain in Table 5. 1.

In Figure 6. 2(a), there are few differences of total tibiofemoral compressive force among the three CL treatment scenarios, though the joint forces of the model with retained CLs were slightly larger than those of the other two scenarios because the ACL tension force was applied to the tibiofemoral articular surface. The simulated knee forces in this paper were quite close to the experimental results (cyan dash lines) obtained by Stylianou et al. [151] until 60° knee flexion. Above that flexion level, the results tended to be much closer to experimental data (black dash lines) reported by Taylor et al. [148]. The results in this paper were also generally consistent with the results calculated by Bersini et al. [62]. The results for the STKI are shown as black dotted lines in Figure 6. 2. After 50° knee flexion, the STKI resulted in smaller tibiofemoral compressive forces than the CTKI. After 58° knee flexion, the compressive force for the STKI started to reduce till 75° knee flexion.

As for the compressive forces on medial and lateral condyles in Figure 6. 2(b) and (c),

the medial condylar force in the CTKI model was larger than that in the STKI model, while the lateral condylar force in the CTKI model was smaller than that in the STKI model. With the increase of knee flexion angle, the medial condyle in the CTKI model was subjected to larger load than the lateral condyle. For the STKI model, although the medial condylar force was also larger than the lateral side in the late knee flexion (beyond around 40° knee flexion for the STKI model), its medial and lateral loads were more evenly distributed than those of the CTKI.

The results for ligament forces in the CTKI model are shown in Figure 6. 3. The MCLs were subjected to larger loads and longer elongations compared to the LCLs due to the larger initial strains in the MCLs. Both aLCL and mLCL were relaxed for most of time until 50° knee flexion for mLCL and 60° for aLCL. In Figure 6. 3(g) and (h), the ACLs were extended until 3° knee flexion for the pACL and 48° for the aACL and then shortened till 50° and 76° flexion angles respectively. In Figure 6. 3(e) and (f), the patellar ligaments were not susceptible to the different cruciate ligament scenarios. In Figure 6. 3(i) and (j), because of the negative initial strains of the PCL and femoral posterior translation, the PCL bundles were always slack without tensile forces. Compared with the CTKI, the STKI model showed much smaller CLL forces. The patellar ligaments were also less stretched with smaller forces produced. The ACL was only in tension before 10° knee flexion.
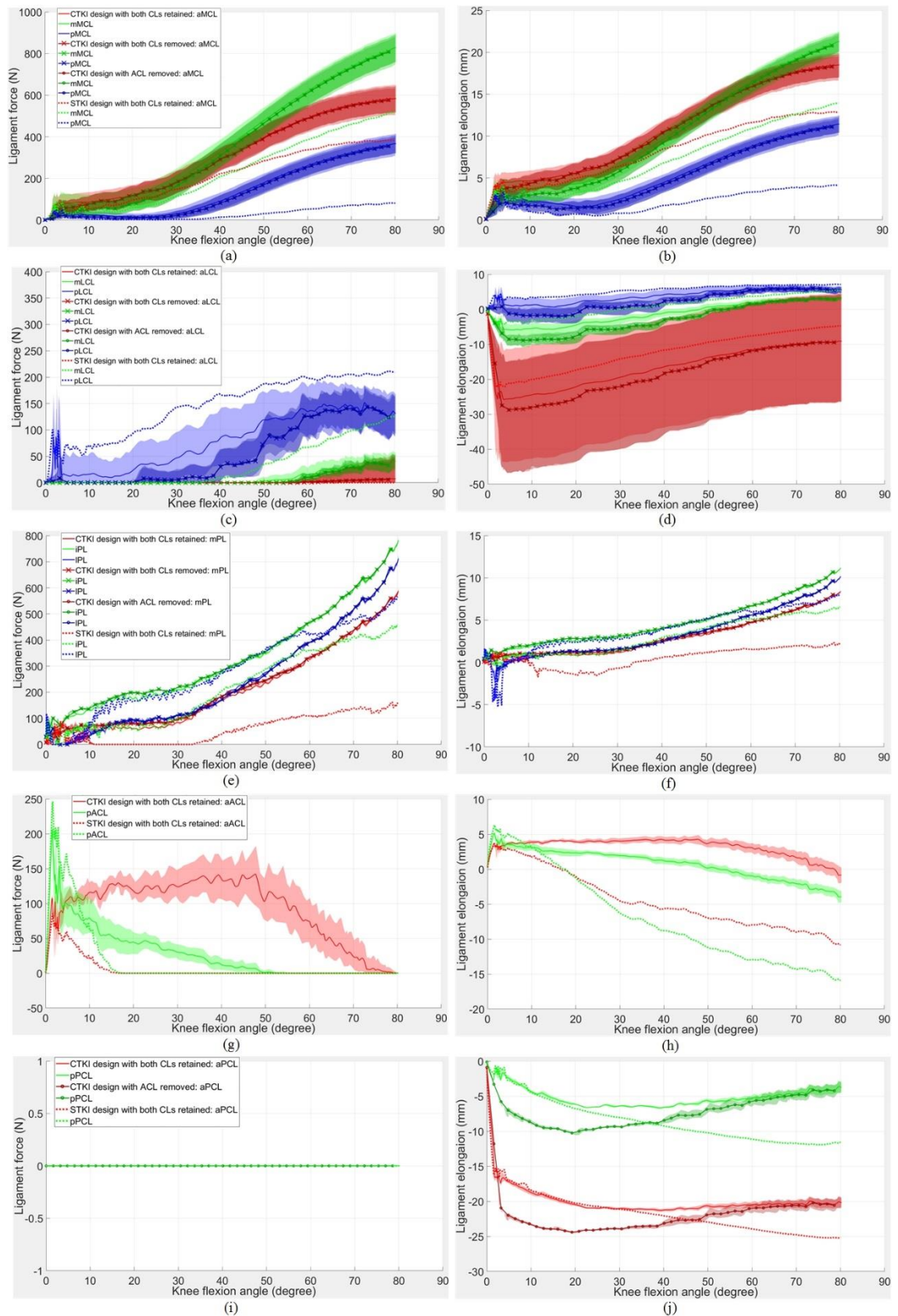
Figure 6. 3 Tensile forces of (a) medial collateral ligaments (MCLs), (c) lateral collateral ligaments (LCLs), (e) patellar ligaments (PLs), (g) anterior cruciate ligaments (ACLs), (i) posterior cruciate ligaments (PCLs) and the elongations of (b) MCL, (d) LCL, (f) PL, (h) ACL, (j) PCL under three scenarios: retained ACL and PCL, removed ACL and PCL and only removed ACL for the CTKI, and one scenario of retained cruciate ligaments for the STKI

6.3 Discussion

This study aimed to simulate the CTKI using a dynamic FE model and considering the close-to-physiological muscle and ankle joint forces. The femoral external rotation and posterior translation of the CTKI with both CLs retained were in good agreement with that of healthy knee measured by Murakami et al. [154] and other tibiofemoral motion ranges and patterns were also consistent with previous results from the literature [25,26].

In contrast, the STKI in this study showed limited femoral external rotation during squatting, which was generally consistent with the results of another referenced STKI design [7] shown in Figure 6. 1(a). Few variations in the medial-lateral direction in the results from the STKI design in Figure 6. 1(c) were due to its symmetric structure. Its exponential increase in adduction rotation in Figure 6. 1(d) may show smaller CLL elongations and forces in the model, which consequently induced much smaller tibiofemoral compressive forces (Figure 6. 2). Smaller femoral superior translation in the STKI model (Figure 6. 1(e)) was mainly due to the revolute radius of the posterior condyles in the STKI being smaller than those of the CTKI whose profile is an ellipse in the sagittal plane.

The STKI resulted in smaller forces than the CTKI after 58° knee flexion. This was mainly due to smaller CLL forces and shorter elongations as shown in Figure 6. 3. It also indicates the significance of designing femoral posterior condyles with appropriate radii. Since a large volume of the posterior condylar bone is removed and replaced with the STKI which has posterior condyles of smaller radius, the distance between the femoral rotational axis and the tibial plateau becomes shorter. This could further decrease the elongation and tensile forces of the CLLs, finally reducing the tibiofemoral contact forces. For the CTKI preliminary design in this study, because the femoral implant geometry was based on patient specific bone anatomy, only the shape or placement of the tibial component could be adjusted to create laxity in the knee joint.

Apart from the tibiofemoral forces, ligaments also affected the tibiofemoral motion of the CTKI model. As shown in Figure 6. 1(b), due to the tensile effect of the ACL, the femoral component could only gradually slide backwards in relation to the tibial

counterpart, in the meantime, interacting with the tibial bearing surface in the medial-lateral direction. However, for the ACL deficient models, the femoral component rapidly moved backwards by 10 mm in the first 5° knee flexion. The ACL is significant for the CTKI for maintaining knee stability during squatting in this study. The elongation variation of ACL in the CTKI was generally consistent with the results of literature [156–158,62]. Although the PCL does not contribute to the knee squat motion due to its negative initial pre-strain, it is still important for other activities such as walking and stair-climbing in leg sway phase. In terms of the STKI design, ACL bundles were only in tensile in the beginning 15° knee flexion due to the setting of positive pre-strain. Therefore, the CLs might not be necessary for the STKI considering that both CLs were not effective in the remaining motion of knee flexion.

The fluctuations in the simulated results in this paper were probably caused by the lack of adduction-abduction moments in ankle and hip joints. The adduction-abduction moments could be applied on FE models in the future when the control algorithm is developed for balancing muscle forces with hip and ankle joint loads.

The measured knee load data in the 4th Grand Challenge Competition to Predict In Vivo Knee Loads [14] were not used for comparing and validating the simulated tibiofemoral compressive forces, because the equations for converting measured data to tibiofemoral compressive forces have been validated only for gait motion.[146] The instrumented implant articulation that was installed on the right knee does not match that of TKI models either.

6.4 Conclusion

The dynamic FE model was successfully created to compare a proposed anatomic CTKI with an off-the-shelf STKI. Different from the traditional knee simulator rig, the dynamic FE model in this study was incorporated close-to-physiological muscle and ankle joint forces, which could make the computer simulations much closer to the actual physical and physiological environment. The CTKI design with both CLs retained was simulated to enable patients' knee to move more naturally. However, improvement is needed on reducing its larger tibiofemoral compressive force than that of the STKI

design after 50° knee flexion, which was caused by the larger knee collateral ligaments in the CTKI model for the larger tibiofemoral relative motions.

Chapter 7

Influence of tibial curvatures on the motions and loads of the customised total knee implant

7.1 Introduction

Customised total knee implant (CTKI) has been shown to restore the kinematics of knee joints by comparing the CTKI of ConforMIS with traditional symmetric total knee implant (STKI) using either in-vivo kinematics study [5] or experiment of the Oxford knee rig [12]. However, the influence of the CTKI design parameters on both kinetic and kinematic responses of the knee joint have never been studied under patient-specific muscle forces and joint reaction forces.

Geometric shapes of knee articulation surfaces differs from person to person. It plays a major role in the knee joint motions during daily activities. Since the natural shape of patient's menisci is severely damaged due to wear problem, the curvature of tibial bearing surface needs to be carefully reconstructed to maximally restore the functionality of a patient's knee joint.

Both tibial longitudinal and transverse radii are normally designed larger than those of the femoral counterpart for the mobility of tibiofemoral joint. Different designs have different parametric values of the tibiofemoral radius such as distal femoral radius and posterior tibial radius, and different knee joint dynamic responses under same boundary conditions.[64] However, there has not yet a definite conclusion or guidance on the best tibiofemoral articulating surface design so far.

Willing et al. [159] used the sequential quadratic programming numerical optimization algorithm to design both tibial and femoral implant components. The knee joint anterior-posterior and internal-external constraint data, and maximum flexion range of motion were used as variables for optimization. However, the true optimum design was not guaranteed due to the limitation of design space, and the boundary conditions for dynamic flexion motions did not include the effect of muscle forces and patella. Ardestani et al. [160] also studied the effect of geometric design parameters of both femoral

and tibial implants on their dynamic performances based on the Stanmore knee simulator. They concluded that the frontal and sagittal radii of the femoral and tibial components had impact on not only the contact pressure but also their relative motions. Uvehammer et al. [161] applied the radiostereometric method to compare the design of flat tibial bearing surface with the design of a concave bearing surface. They found that the concave design resulted in increased anterior-posterior translations compared with normal knees. However, the internal tibial rotations of both designs were observed to be less than normal knees. Ignoring the design parameters of the tibial component, Clary [68] studied different designs of the femoral implant with different femoral sagittal radii, and demonstrated the sensitivity of motion changes to the subtle differences between implant designs.

In this chapter, the influence of the curvatures of tibial bearing surfaces on the motions and loads of the knee joint during a squatting motion is investigated. The dynamic simulations are conducted based on the Oxford knee rig with the effect of muscles and ligaments. The tibiofemoral compressive forces, relative motions, knee joint ligaments forces and contact stresses of the tibiofemoral and patellofemoral joints of both CTKIs and STKI models were extracted from the simulations and compared.

7.2 Changing radius of curvature of tibial bearing surfaces

As explained in Figure 3. 13 in Chapter 3, in the modelling of the tibial bearing surfaces, the longitudinal curves for cutting the tibial plate were two ellipses. The long axis radii (a_ellipse_new) of these two ellipses, were a number ($i = 2,3,4 \cdots n$) times their counterparts (a_ellipse) of the fitting ellipses respectively. In the modelling of the transverse curves of the tibial bearing surfaces, two quadratic curves were used to fit the cross-section curves of each femoral condyle through the method of least squares fitting. The medial and lateral transverse curves of each tibial bearing surface were created through adjusting the coefficients a_1 and a_2 of the fitting quadratic curves into the a_{1_new} and a_{2_new} respectively shown in Figure 3. 14. In this chapter, three different longitudinal curves and six sets of different medial and lateral transverse quadratic curves listed in Table 7. 1 were implemented to investigate their effect on the tibiofemoral and patellofemoral dynamic behaviours during the squat motion. In Table 7. 1, the med.: lat. means the quadratic coefficient of medial side versus that of the lateral

side of each condyle. The medial sides of two condyles are the sides that two condyles adjoin each other. Both longitudinal cutting curves were hypothesized to have the same coefficients i on their long axis radii. Similarly, the medial and lateral quadratic coefficients for the medial tibial bearing surface were consistent with those of the lateral counterpart.

Table 7. 1 Coefficients of the longitudinal elliptical long axis radius and quadratic curves of each tibial bearing surface

i	med.: lat.	med.: lat.	med.: lat.	med.: lat.	med.: lat.	med.: lat.
2	$a_1/2$:$a_2/3$	$a_1/3$:$a_2/2$	$a_1/4$:$a_2/6$	$a_1/6$:$a_2/4$	$a_1/6$:$a_2/8$	$a_1/8$:$a_2/6$
4	$a_1/2$:$a_2/3$	$a_1/3$:$a_2/2$	$a_1/4$:$a_2/6$	$a_1/6$:$a_2/4$	$a_1/6$:$a_2/8$	$a_1/8$:$a_2/6$
6	$a_1/2$:$a_2/3$	$a_1/3$:$a_2/2$	$a_1/4$:$a_2/6$	$a_1/6$:$a_2/4$	$a_1/6$:$a_2/8$	$a_1/8$:$a_2/6$

7.3 Materials

The collateral ligaments were modelled as nonlinear springs with consideration of pretension, which is the same as that in Chapter 3. In order to simulate the nonlinear material property of tibial insert material ultra-high molecular weight polyethylene (UHMWPE), its material property was varied from linear (Elasticity modulus $E = 1016$ MPa, Poisson's ratio $v = 0.46$) in the former chapter to nonlinear elastic-plastic (initial $E = 550$ MPa, $v = 0.46$) [108] with its stress-strain relationship shown in Figure 7. 1. The dynamic simulation with the previous collateral ligament pre-strain setting resulted in a single-side-condylar lift-off due to the insufficient pretensions between the femur and the tibia. Therefore, all the pre-strains were re-set to be 0.1. The spring stiffness of the patellar ligaments was also changed from linear (K=70 N/mm) into nonlinear properties plotted in Figure 7. 2. The nonlinear spring stiffness was plotted based on the patellar ligament force-elongation relationships for men which were experimentally measured by O'Brien et al. [162]. The patellar ligament force was calculated from the measured joint moment during a ramped voluntary isometric knee extension contraction, the antagonist knee extensor muscle co-activation quantified from its EMG activity, and the patellar ligament moment arm measured from magnetic resonance image. The tendon elongation was imaged using the sagittal-plane ultra sound scans throughout the contraction.[162]
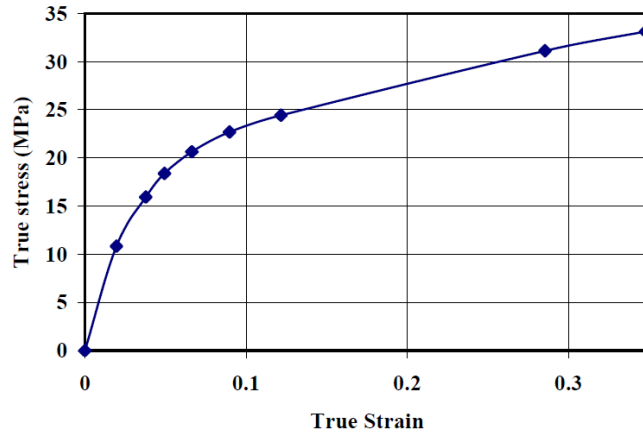
Figure 7. 1 Nonlinear true stress versus true strain for UHMWPE material model [108,163]
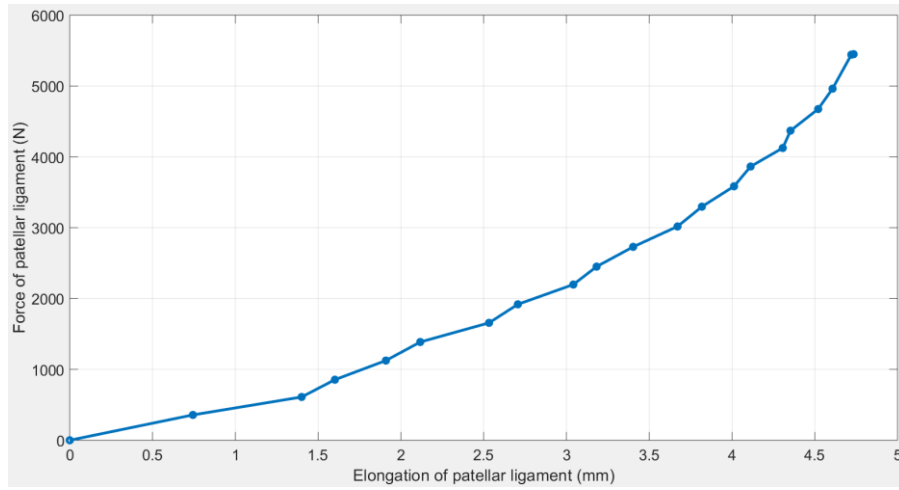
Figure 7. 2 Patellar ligament force-elongation relationships for men [162]

7.4 Boundary conditions and initial conditions for dynamic simulations

The boundary conditions were kept the same as in Chapter 5 except the ankle joint reaction loads which were curve-fitted for saving computational cost and facilitating the contact convergence while introducing the nonlinear material property of UHMWPE. The sum of sine functions $\sum_{i=1}^{i=8} a_i \sin(b_i \cdot x + c_i)$ in the curve fitting tool of MATLAB (R2017a) was used to fit the original OpenSim joint reaction results. The fitted results of the ankle joint reaction loads are shown in Figure 7. 3.
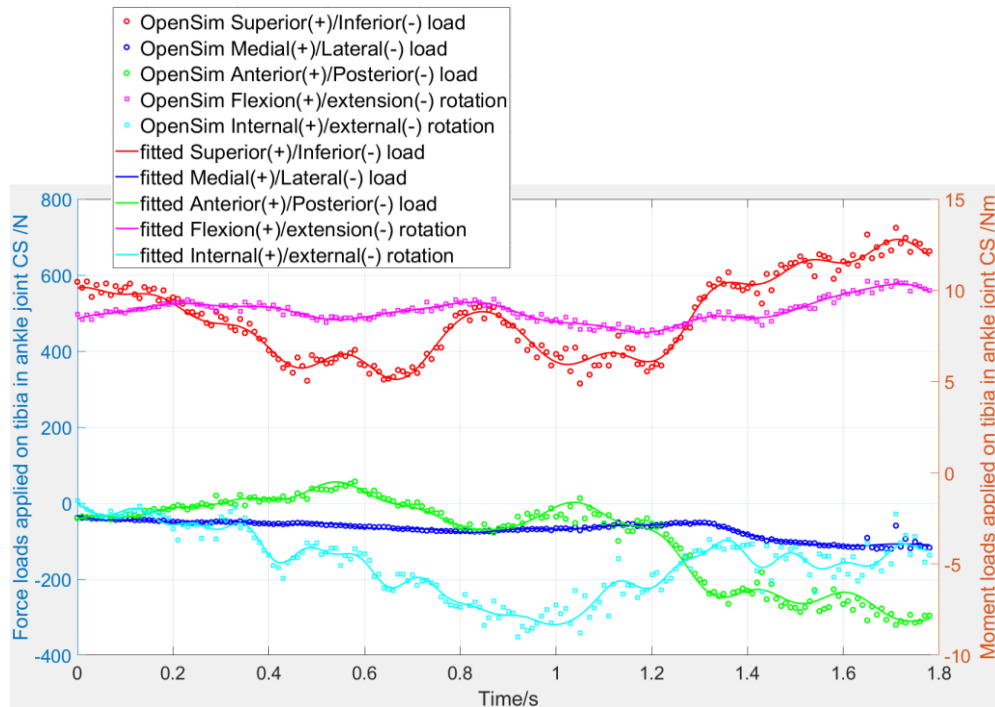
Figure 7. 3 Original OpenSim results of ankle joint loads and fitted ones through MATLAB
curve fitting tool box

Because the finite element model was not balanced initially in the ANSYS transient dynamic FE analyses under many time-varying loads, some boundaries needed to be constrained to make the whole system easily reach a balanced and converged state. In this chapter, the degree of freedom of the tibial internal-external rotation was fixed in the first 0.04 seconds. After 0.04 seconds, those constraints would be removed to allow the tibial component to move freely, however, they would be still under the restraint of the knee collateral ligaments, patellar collateral ligaments and retinaculum ligaments. For the pretension of ligament spring models, since in ANSYS Mechanical APDL it is not allowed to directly set pretension or initial force on the non-linear spring element COMBIN39, the pretension load was converted into displacement load on those springs in the first 0.01 seconds. After 0.01 seconds, the moving end of the spring would be bonded to the ligament insertion point through the node-to-node contact setting for the rest of simulations. The constraints on the mediolateral translation of patella bone were applied in the beginning and would be removed at 0.01 seconds.

7.5 Results and discussion

7.5.1 Tibiofemoral compressive forces of the CTKIs and the STKI
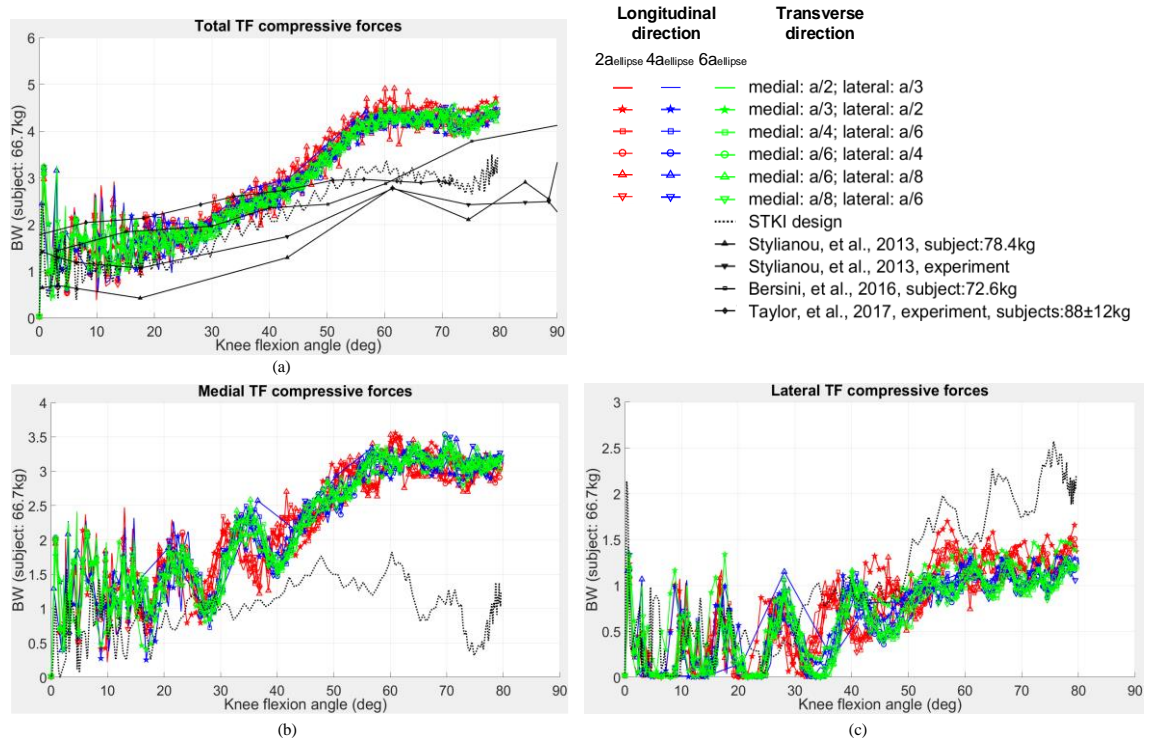
Figure 7. 4 Tibiofemoral compressive forces of the CTKIs and the STKI: (a) total forces; (b) medial forces; (c) lateral forces

There were not significant differences in the tibiofemoral compressive forces among the tibial inserts with different longitudinal and transverse curvatures in Figure 7. 4. However, the tibiofemoral compressive forces of the CTKIs were larger than that produced by the scaled symmetric DePuy model, STKI after 50° knee flexion. Apart from that, it is worth noting that there was big difference in tibiofemoral load distributions between the CTKIs and the STKI. From 30° knee flexion, the medial side of the CTKIs was subjected to larger load than the counterpart of the STKI, while from 50° knee flexion, the STKI showed larger compressive forces on the lateral condyle than the CTKIs. Consequently, the two designs presented different results of the medial-lateral load ratio with an average of 2.4 in the CTKI and 0.6 in the STKI model during the last 30° knee flexion.

Comparing with the published results of other researchers [59, 141, 144] on the total tibiofemoral compressive forces in Figure 7. 4(a), both the CTKIs and the STKI showed

good agreement with either experimental or simulation results in the first 45° of knee flexion. However, in the following knee flexion, the total tibiofemoral compressive forces of the CTKIs tended to be larger than the published results, while those of the STKI was still in the range of the published results.

7.5.2 Tibiofemoral relative motions of the CTKIs and the STKI
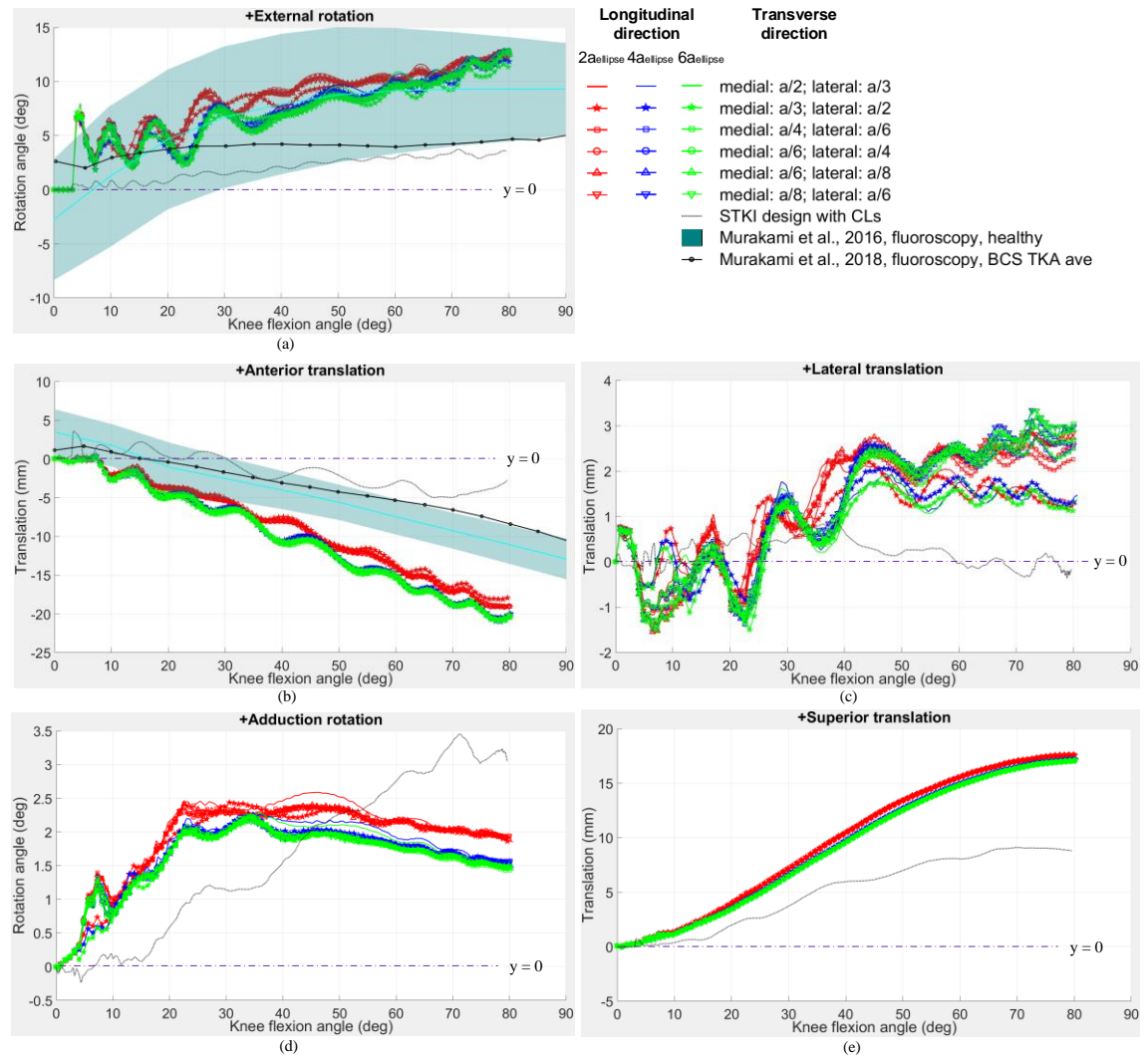
Figure 7. 5 Relative motions of the tibiofemoral joints of eighteen CTKIs (three longitudinal elliptical long axis radii and six transverse curvature sets) and the STKI model with cruciate ligaments retained

Apart from the comparisons of tibiofemoral compressive forces between the CTKIs and the STKI, the relative motions of these two designs were also compared in Figure 7. 5 to investigate how different their motions were and how closely their motions resembled the motion produced by healthy knees (cyan shade). Regarding the femoral external

rotations shown in Figure 7. 5(a), the CTKIs behaved consistently with the healthy male knees measured by Murakami et al. [154] by using the fluoroscopy method. However, the limited ranges of rotational motion were observed not only in the STKI which was simulated in the same conditions as the CTKIs, but also in another STKI model (bi-cruciate stabilized (BCS) TKA) that was in-vivo measured on 22 subjects by Murakami et al. [7]. The femoral external rotation trend of the scaled DePuy STKI model simulated in this study showed good agreement with that of BCS TKR used by Murakami et al. [7]. The femoral external rotational range of both STKI designs were around 3° for the whole squatting motions, while the femoral external rotation ranges of CTKIs were over 10°.

With regard to the femoral anterior-posterior translations shown in Figure 7. 5(b), the CTKIs also showed much greater range of motion (ROM) than both STKIs. From 30° knee flexion onward, the femoral components of the CTKIs slid back more than the measured results of healthy knees. It might be because there was no soft tissue or muscles such as gastrocnemius wrapping around the posterior condyles in these simulations, which could provide further restrictions on the tibiofemoral motions.

Regarding the mediolateral motion of tibiofemoral joints shown in Figure 7. 5(c), a nearly constant motion pattern was observed in the STKI model, which was caused by the good congruency between the femoral and tibial components in the mediolateral direction. In contrast, small amount of mediolateral movements between -1.5 mm and 4 mm was shown in the CTKIs. Since the tibial inserts of the CTKIs in this study were designed as asymmetric structure with less conforming surfaces between the tibial and femoral components, it allowed the CTKIs to self-adjust positions according to the changing muscles and joint loads. However, due to the wedge shape between the two tibial bearing surfaces, these mediolateral translations are not completely unrestrained. Although there was no big difference among the CTKI models in the three long axis radii of the longitudinal elliptical curve of tibial bearing surfaces, the differences can be observed among models with different transverse curvatures in each longitudinal curvature. The smaller the radius of transverse curvature of the tibial bearing surface was, the smaller range the tibiofemoral joint was allowed to move in the mediolateral direction.

For the comparisons of the adduction rotations shown in Figure 7. 5(d), the STKI design showed a linear increase in the adduction rotational angles with the increase of knee flexion angle, while the adduction rotational angles of the CTKIs only increased to 2°~2.5° until 30° knee flexion. After that, the knee joints of the CTKIs abducted about 0.5°~1°. It is worth noting that the CTKIs showed good agreement on this motion pattern with the descriptions in literature [25, 55]. It can also be observed in the results of the CTKIs that the maximum adduction rotational angle of the femoral component was influenced by the longitudinal curvatures of the tibial bearing surface. The maximum adduction angle is about 2.5° for the tibial implant with the long axis radius of $2a_{ellipse}$ in the longitudinal direction, while 2.2° for the tibial implant with the long axis radius of $4a_{ellipse}$ and $6a_{ellipse}$.

Lastly, the superior translation of the STKI design shown in Figure 7. 5(e), was 8 mm smaller than that of the CTKIs, which was caused by the geometry differences between the two designs. The CTKIs are designed based on patient's own distal femur geometry, while the STKI is off-the-shelf, manufactured in batches. It is inevitable that excessive healthy bone would be cut off for installing the implant component. In this case, the distal femoral geometry is dramatically changed especially in the posterior condyles. Because of the smaller radius of posterior condyles, the ROM of the STKI model in the superior direction was significantly smaller than that of the CTKIs. However, the range of superior translation of the CTKIs was also found to be consistent with the descriptions in the literature [25,58] as well as that of the lateral and posterior translations.

7.5.3 Knee joint ligament forces and elongations of the CTKIs and the STKI

In Figure 7. 6, the knee collateral and patellar ligament forces and the elongations in the CTKIs with the longitudinal elliptical long axis radius of $4a_{ellipse}$ and the STKI during the squatting motion were shown. Under the same pre-strains (0.1) of the collateral ligament bundles, the MCLs of CTKIs showed larger tension forces and elongations than those of the STKI, while the LCLs of the CTKIs presented opposite responses. As regard to the PLs, the medial and inner bundles of the CTKIs had larger tension forces and elongations than those of the STKI design did, while the tension forces and elongations of the lateral bundle of the CTKIs were smaller than those of the STKI design.
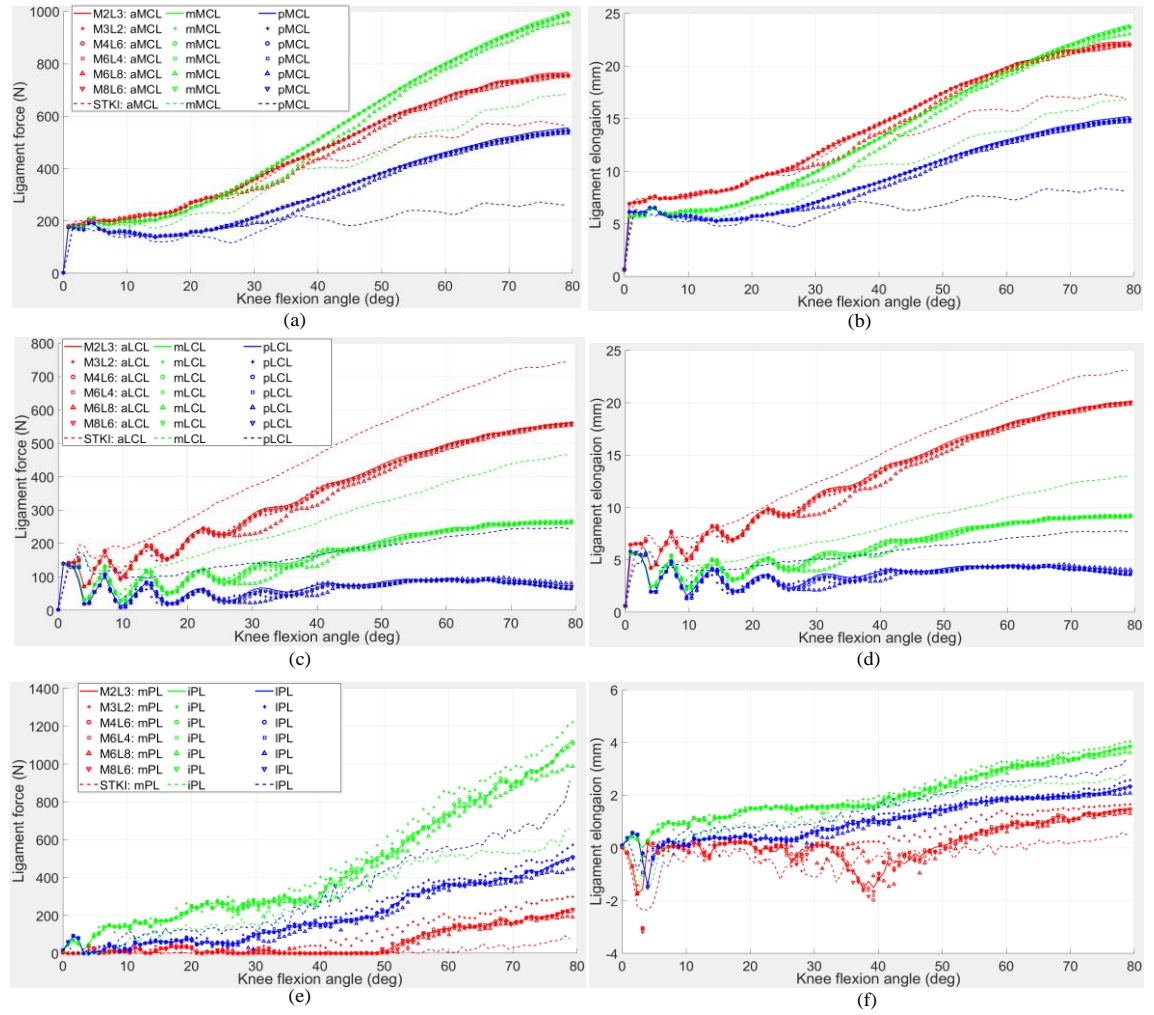
Figure 7. 6 Ligament forces of (a) MCLs; (c) LCLs; (e) PLs and ligament elongations of (b) MCLs; (d) LCLs; (f) PLs of the CTKIs with the longitudinal elliptical long axis radius of 4aellipse and the STKI

The knee cruciate ligament forces and elongations in the CTKIs and STKI during the squatting motion can be seen in Figure 7. 7. The anterior ACL (aACL) of the CTKIs was pulled till about 50° knee flexion angle, then became relaxed with the increase of the knee flexion, while the posterior ACL (pACL) of the CTKIs was quickly stretched by 7mm at 2° knee flexion and gradually shortened to its zero-load length at 70°~80° knee flexion. In contrast, both bundles of ACL of the STKI model became slack in the earlier flexion angles than the CTKIs. Both PCL bundles were in slack condition during the squatting motion in both designs due to the ligament pre-strain setting.
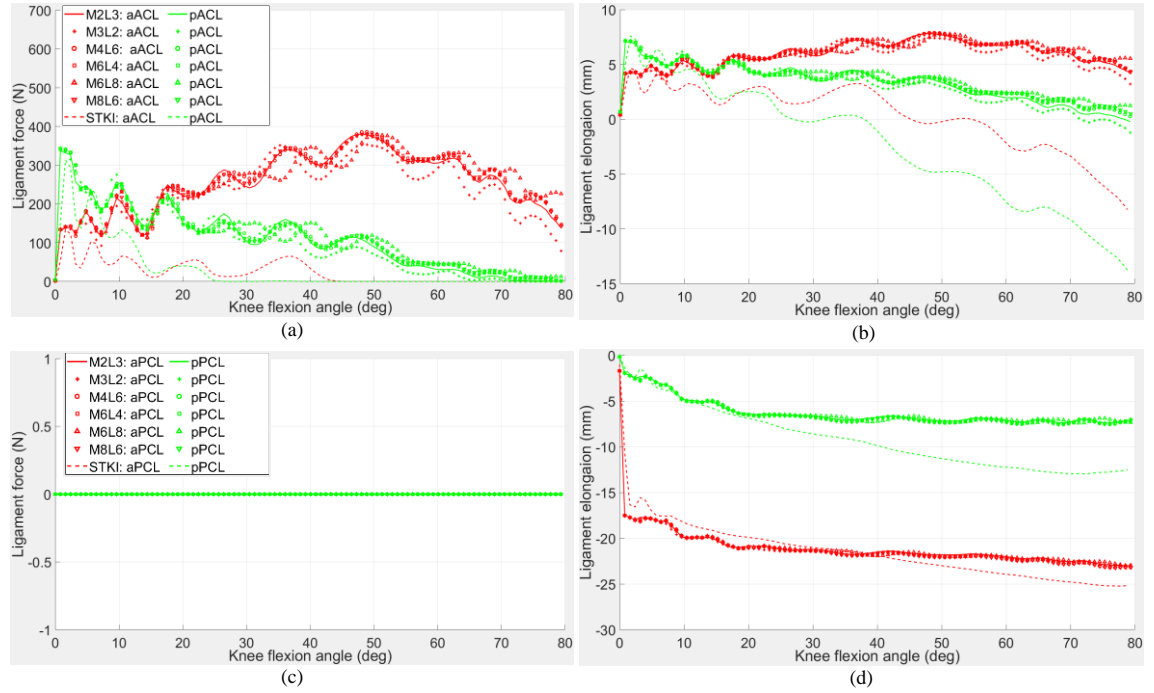
Figure 7. 7 Ligament forces of (a) ACLs; (c) PCLs and ligament elongations of (b) ACLs; (d) PCLs of the CTKIs with the longitudinal elliptical long axis radius of 4$a_{ellipse}$ and the STKI

7.5.4 Contact stress of tibiofemoral and patellofemoral joints

Since there were not big differences among the eighteen tibial insert designs in the tibiofemoral compressive forces and relative motions, the contact stresses of only one CTKI design were shown with medial side curve coefficients of a_1/4, lateral side curve coefficients of a_2/6 and longitudinal elliptical long axis radius of 4$a_{ellipse}$, and compared with those of the STKI design.

As can be seen in Figure 7. 8, the tibiofemoral contact stress of the CTKI at the flexion angle of 1° was much higher than that of the STKI. Then the two designs showed comparable stresses at 30° and 45° knee flexion. Subsequently, the tibiofemoral contact stress of the CTKI increased to 68MPa at 80° knee flexion, while the tibiofemoral contact stress of the STKI increased to 50 MPa at 60° knee flexion and then decreased to 25 MPa at its maximum flexion angle. It might be because the ACL bundles were not subjected to loads after 45° knee flexion in the STKI design shown in Figure 7. 7. But in the CTKI designs, the aACL tensile force kept increasing till 400 N at 50° knee flexion and then decreased to 150 N at the maximum knee flexion angle of 80°.
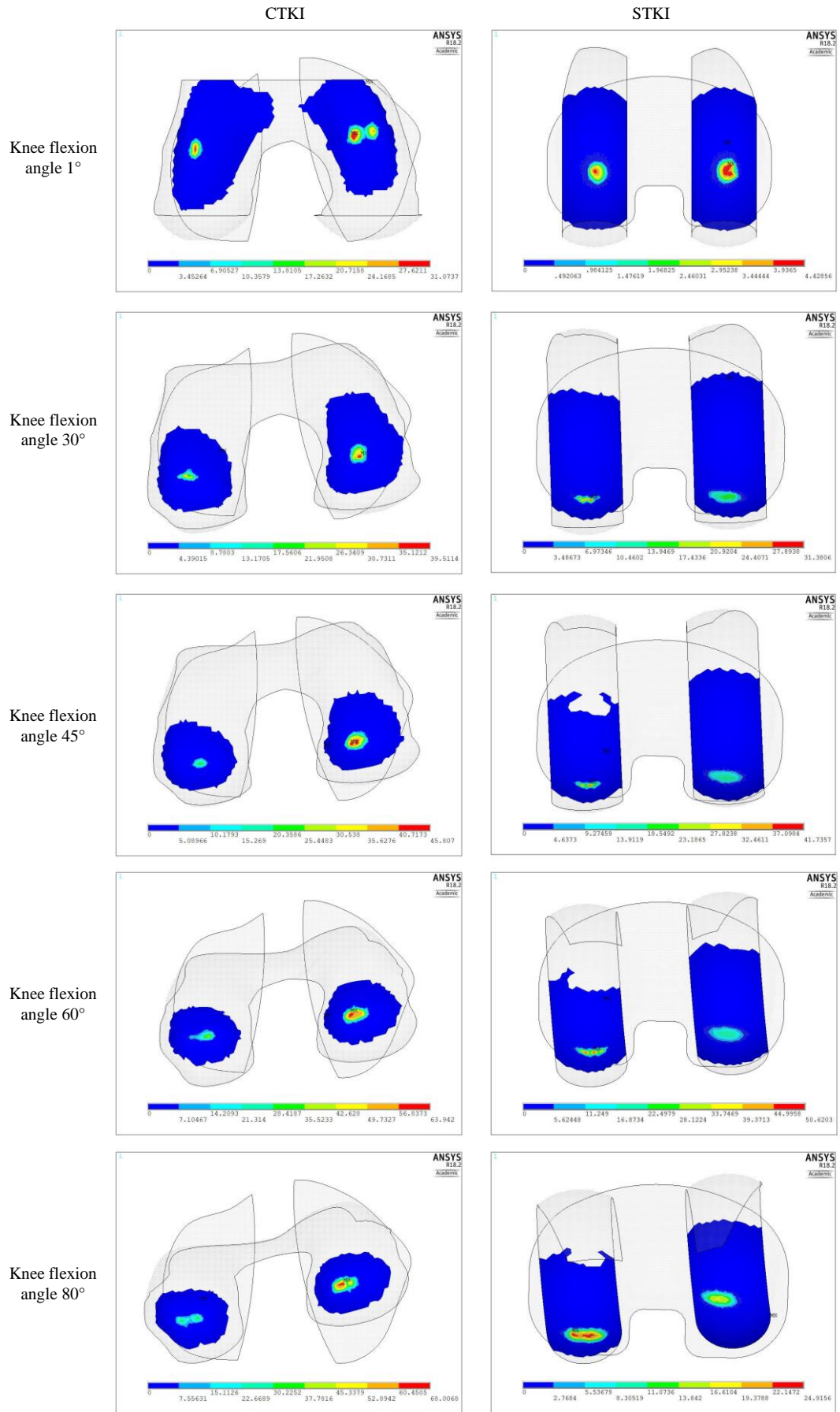
Figure 7. 8 Tibiofemoral normal contact stresses of the CTKI and the STKI

	CTKI	STKI
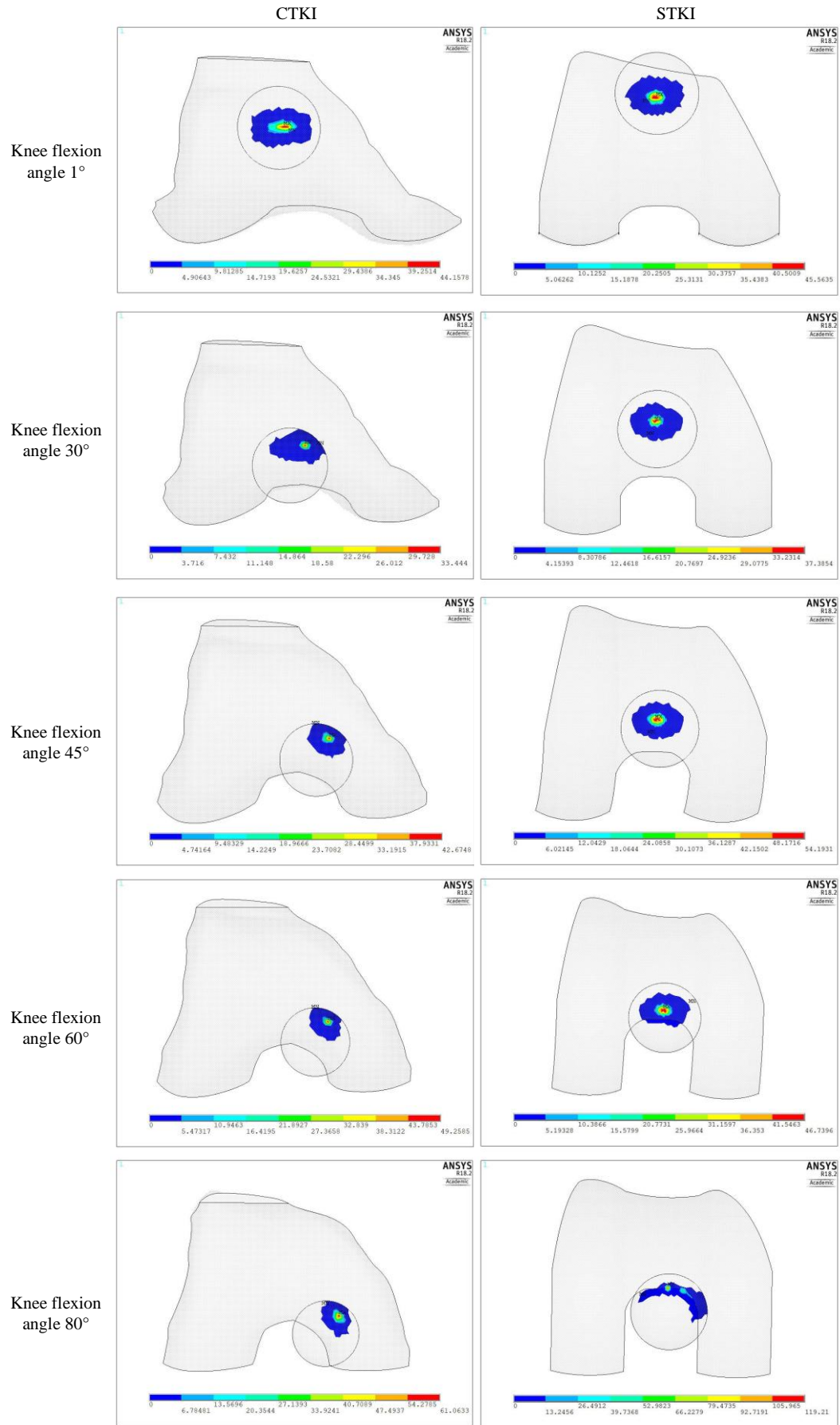
Figure 7. 9 Patellofemoral normal contact stresses of the CTKI and the STKI

Regarding the patellofemoral contact stresses shown in Figure 7. 9, the stress magnitudes in both designs at the corresponding knee flexion angles were almost the same except at the maximum flexion angle where stress concentration occurred in the STKI model when the patellar button slid to the fringe of femoral intercondylar groove. The medial translation of patella of the CTKI was much larger than that of the STKI. It is because the CTKI model resulted in a larger internal rotation of tibia on which the patellar ligament bundles were attached.

Almost all the contact stresses of both tibiofemoral and patellofemoral joints in the two designs exceeded the yield strength (27 MPa) of the UHMWPE [164]. Carr and Goswami [165] also reported high tibiofemoral contact stresses around 50~80 MPa due to the varus tilt of the femoral component and 40~52 MPa due to the medial translation of the femoral component. Simpson et al. [166] built FE models of unicompartmental knee replacements (UKR) for studying the effect of bearing congruency on the stresses of UKR bearings. In-vivo kinematics data and the measured load data from an instrumented implant for a step-up motion were applied on the FE models. They found that only the contact stresses of fully-congruent UKR were below the polyethylene lower fatigue limit (17 MPa) [167], while the partially-congruent UKR with a concave bearing surface and non-congruent UKR with a flat bearing surface experienced high contact stresses of 40~50 MPa. Although the fully-congruent UKR was less likely to fail from fatigue, it was susceptible to different failures such as bearing dislocation.

Too much compressive forces are detrimental to the durability and longevity of the CTKI, especially to the tibial insert which is made of UHMWPE. Too much compressive forces would induce large stresses and further cause the wear failure of component. Therefore, increasing the contact areas between the tibiofemoral components will be investigated in the future study. One potential way to increase the contact areas is to create regular geometric shapes for the femoral and tibial components, in other words, simplified contact surfaces but still based on the patient-specific knee joint characteristics. Another way is to combine the design method for the CTKI in this paper with the design method proposed by Walker [131]. That means the femoral component is created through the methods of key feature

point recognition and least-squares elliptical curve fitting, while the tibial component is created using drape function over the lower surface of multiple rotating positions of the femoral component.

7.6 Conclusion

Changing the transverse and longitudinal curvatures of the tibial bearing surface of the CTKI did not result in significant differences in the tibiofemoral compressive forces, and relative motions, however, the femoral mediolateral translation showed a difference of 2mm which was mainly caused by the transverse curvatures of the tibial bearing surface. The slight difference of $0.3°{\sim}0.5°$ between the femoral adduction angles was influenced by the longitudinal curvatures of the tibial bearing of the CTKI. The differences between the femoral external rotations in the CTKIs were less than $2°$. Good agreement was shown in the femoral external rotation between the CTKIs and healthy knees. Other motions of CTKIs are generally consistent with the published data.

In contrast, the STKI simulated in the same condition as the CTKIs showed relatively constant femoral external rotation, posterior translation and mediolateral translation. It is due to the symmetric structure of the femoral and tibial components and congruency of the tibiofemoral contact surfaces. The design concept of the STKI is mainly to alleviate patient's knee pain and meanwhile help patient's knee to move in a certain range of motion. Apparently, the STKI design cannot fulfil the patients' desire to move naturally and normally.

Based on the simulated kinematic results of the CTKIs, it can be concluded that the CTKI does have the potential to enable patient's knee to move naturally. However, the CTKI doesn't show comparable or even smaller tibiofemoral compressive forces than that of the STKI above 50° knee flexion. It is mainly due to the less restricted CTKIs designed with the less conforming geometric shapes between the femoral and tibial components.

Chapter 8

Influence of resurfaced and unresurfaced patellae on the patellofemoral joint

8.1 Introduction

Resurfacing of patella during total knee arthroplasty (TKA) still remains controversial. It is usually performed on the presence of anterior knee pain, inflammatory arthritis, patellar mal-tracking and damaged articular cartilage. Many surgeons would resurface patella to avoid developing postoperative anterior knee pain and the need of revision surgery.[168] The influence of resurfaced and unresurfaced patellae on the traditional TKA implant have been studied either through experiments based on the Oxford knee rig or using computer simulations, however, their influence on the customised femoral component has not been studied yet with kinematic and kinetic computer simulations. Previous TKA simulations and tests seldom considered the effect of comprehensive muscle and joint forces during a patient-specific squatting motion. The ankle joint loads in those published literatures were either ignored or too small in human squatting motions.

Matsuda et al. [169] used cadaver tests to study the effect of dome-shaped, conforming, and unresurfaced patellar on the patellofemoral contact stresses and areas after total knee replacement surgery. Both the resurfaced patellar designs were reported to have markedly higher contact stresses but smaller contact areas than those of the unresurfaced one. The stresses of both dome-shaped and conforming components exceed the yield limit of polyethylene even at low test loads. Fitzpatrick and Rullkoetter [69] studied the patellofemoral joint motions and contact stresses of three different commercial implants through finite element models. Compressive strain in the patellar bone in the unresurfaced condition was found substantially higher than in the resurfaced conditions in the large knee flexions. Mason et al. [170] reported discrepancies in the patella forces during squat motion through different methods, either using the in-vivo kinematic measurement or the experiments based on the Oxford knee rig. Browne et al. [129] tested central dome-shaped and medialized patellar implants on two different femoral components placed in six human cadaver knees based on the Oxford knee rig. No

significant differences in the patellofemoral compressive and shear forces were observed in both patellar implant designs. But the knee implant with longer extensor moment arm was found to be able to reduce the quadriceps forces and then further reduce the patellofemoral compressive forces. Trepczynski et al. [171] calculated in-vivo patellofemoral and tibiofemoral forces using a musculoskeletal model during different daily activities. The in-vivo peak tibiofemoral forces of 2.9–3.4 bodyweight (BW) varied little across activities, while the peak patellofemoral forces showed significant variability, ranging from less than 1 BW during walking to more than 3 BW during high flexion (over 90°) activities. The peak patellofemoral forces during those high flexion activities were also reported to exceed the peak tibiofemoral forces. Besides, Fekete et al. [172] used analytical method to calculate the patellofemoral forces with consideration of the changing positions of the trunk's centre of gravity and reported a patellofemoral compression force of 3.3 BW at 80° knee flexion.

In this study, the influence of unresurfaced and resurfaced patellae on the patellofemoral joint forces and relative motions of the customised total knee implant (CTKI) was investigated through applying the patient-specific muscle forces and joint reaction forces which were calculated using OpenSim. The pre-strains of patellofemoral collateral ligaments (PFCLs) between the unresurfaced patellofemoral joint were varied to investigate the influence of laxity of PFCLs on the results. The size and shape of the dome-shaped patellar button were changed to investigate their effects on the dynamic responses of the patellofemoral joint and its contact stresses. The simulated patellofemoral joint forces and relative motions were compared with the published results from either experimental measurements or simulations.

8.2 Geometries of the unresurfaced and resurfaced patella

The unresurfaced patella model was created based on the CT images of the patella of subject JW. The articulation surface of the unresurfaced patellar was removed for installing the patellar implant. The dome-shaped/button component is shown in Figure 8. 1. It is created with reference to the literature [108] without any changes and regarded as an extreme condition. The bottom radius of the dome is 15 mm and the depth is 8 mm. In order to cover the patellar bone after resection, the button component was then modified to create two more models. One was only modified to have a larger radius of

28 mm, therefore it looked much flatter in the side view. Another was scaled up from the referenced dome-shaped component by 1.87 times.
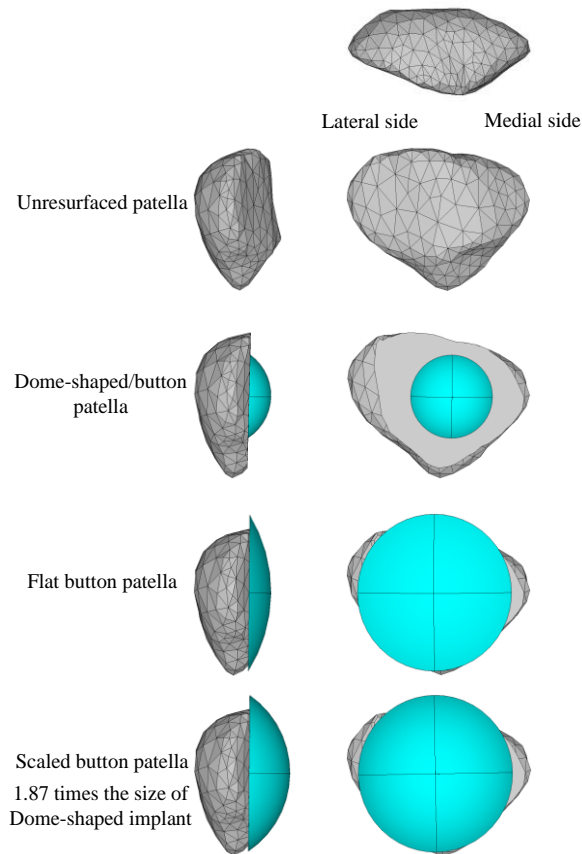
Figure 8. 1 Modelling of the unresurfaced patella and three different patellar buttons: the dome-shaped button referenced from Shi [108]; the flat button which kept the implant depth unchanged but increased the radius of dome bottom; and the scaled button which is 1.87 times the referenced button model.

8.3 Material and boundary conditions

The materials of the patellar implant and tibial insert are UHMWPE with nonlinear elastic-plastic ($E = 550$ MPa, $\nu = 0.46$) property. Its stress-strain relationship is shown in Figure 7. 1. The pre-strains of all collateral ligament bundles were set 0.1. The patellar ligaments were also assigned nonlinear property but with the force-deflection relationship referenced from the literature [162]. The patellar bone was assumed as cortical bone with a constant elastic modulus.

The boundary conditions were set the same as those in Chapter 7 such as applying the

smoothened ankle joint loads, restrained patella with only flexion and superior-inferior motions in the first 0.04 seconds, and time-varying muscle forces.

In the unresurfaced patella model, the PFCLs pre-strain values of 0.1, 0.05, 0.01 and 0.001 were simulated respectively for different laxity scenarios with the ligament stiffness of 2000 N/m.

8.4 Results and discussion

8.4.1 Contact forces and motions of the unresurfaced and resurfaced patella models

As can be seen in Figure 8. 2, the patellofemoral contact forces of both resurfaced and unresurfaced models were in good agreement with the referenced research results except at the early knee flexion and the last 20° of knee flexion in this study. The differences in the early knee flexion were mainly due to the laxities of the patellar collateral ligaments. The smaller the spring pre-strain was, the smaller reaction force was produced between the femoral component and patella or patellar implant. At the last 20° of knee flexion, the patellofemoral contact forces of both resurfaced and unresurfaced patella models were smaller than the results published by Komistek et al. [173] and Sharma et al. [174]. It might be caused by the contact between quadriceps muscles and femoral component while the quadriceps wrapped around the distal femur. But in general, the trend of the simulated patellofemoral forces agreed well with the published research results.
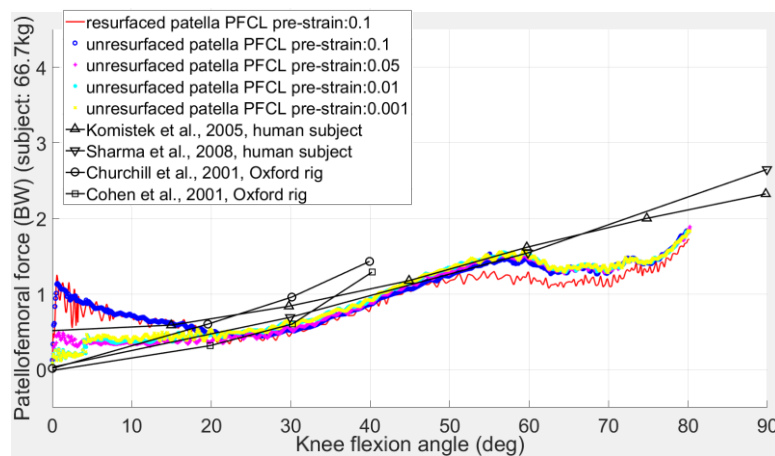
Figure 8. 2 Patellofemoral contact forces under different laxities of patellofemoral collateral ligament (PFCL)

Figure 8. 3 Relative motions of patella over femoral component: (a) flexion-extension rotation; (b) external-internal rotation; (c) medial-lateral rotation; (d) medial-lateral translation; (e) posterior-anterior translation; (f) inferior-superior translation

The relative motions between the patella and femoral component are presented in Figure 8. 3. The values of the relative motions were solved through the rotational matrix and Euler angles. In Figure 8. 3(a), the flexions of patella in the resurfaced and unresurfaced models were consistent with the results obtained from simulation conducted by Fitzpatrick et al. [69] and the results measured by Dagneaux et al. [175]. However, the external-internal rotations of all simulated patella models shown in Figure 8. 3 did not match the result trends from Fitzpatrick et al. [69] and Dagneaux et al. [175]. The resurfaced patella firstly rotated towards the lateral side of the knee joint till the knee flexed to 20°, and then it internally rotated, which is similar to the results obtained by Fitzpatrick et al. [69]. It was due to the PFCL pre-strains with assumed values rather than measured from the subject JW. Once the lateral side PFCLs produced larger tensile forces than the

medial side, the patella would inevitably rotate externally. In contrast, the unresurfaced patella under the different PFCL pre-strains only rotated linearly towards the medial side of the knee joint. It might be caused by the non-conforming shapes between the patellar bone and femoral component. At a certain angle of knee flexion, the contact area of the patellofemoral joint would shift superiorly to the top of the patella, which could reduce the contact area between the patella and femoral component, and further cause difficulty in reducing the patellar internal rotation.

The trends and magnitudes of the unresurfaced patella in medial tilt rotation are shown in Figure 8. 3(c) and the medial translation in Figure 8. 3(d). They matched well with the measured results from Dagneaux et al. [175], except that the sharp increases at 4° knee flexion were observed in the two patellar motions when the pre-strain of PFCLs was less than 0.01. The same situation occurred in the patellar external rotation as well. It was mainly due to the pretension forces of PFCLs that were too small to resist the medial patellofemoral force, which caused the patella to suddenly slide towards the medial side of the knee joint. In contrast, the resurfaced patella experienced smaller medial tilt from 20° knee flexion and larger medial translation from 50° knee flexion.

The patellar posterior translation shown in Figure 8. 3(e) was almost linearly proportional to the knee flexion angle, however, there was a slight posterior translation in the Dagneaux's results [175]. It is probably due to the smaller load on the ankle joint of Dagneaux's subject, and the differences in geometric shapes of the femoral grooves and the initial position of the patella. Different shaped trochlear groove would guide the patella to slide on it and affect its motion trajectory. In Figure 8. 3(f), the inferior translations of the resurfaced and unresurfaced patellae were in good agreement with Dagneaux's results [175] in the first 30° of knee flexion. After that, patellar inferior translations in this study gradually reached 31 mm at 55° knee flexion. The curve of the simulated results in   Figure 8. 3(f) also showed that the patella slid from its initial location to almost the end of trochlear groove.

8.4.2 Contact forces and motions of three different resurfaced patellar buttons

The size and shape of the patellar button can affect its motion trajectory and loads on the trochlear groove of the femoral component. Therefore, the CTKI models with different patellar button sizes and surface curvatures, were simulated to reveal differences in kinetic and kinematic characteristics as shown in Figure 8. 4.
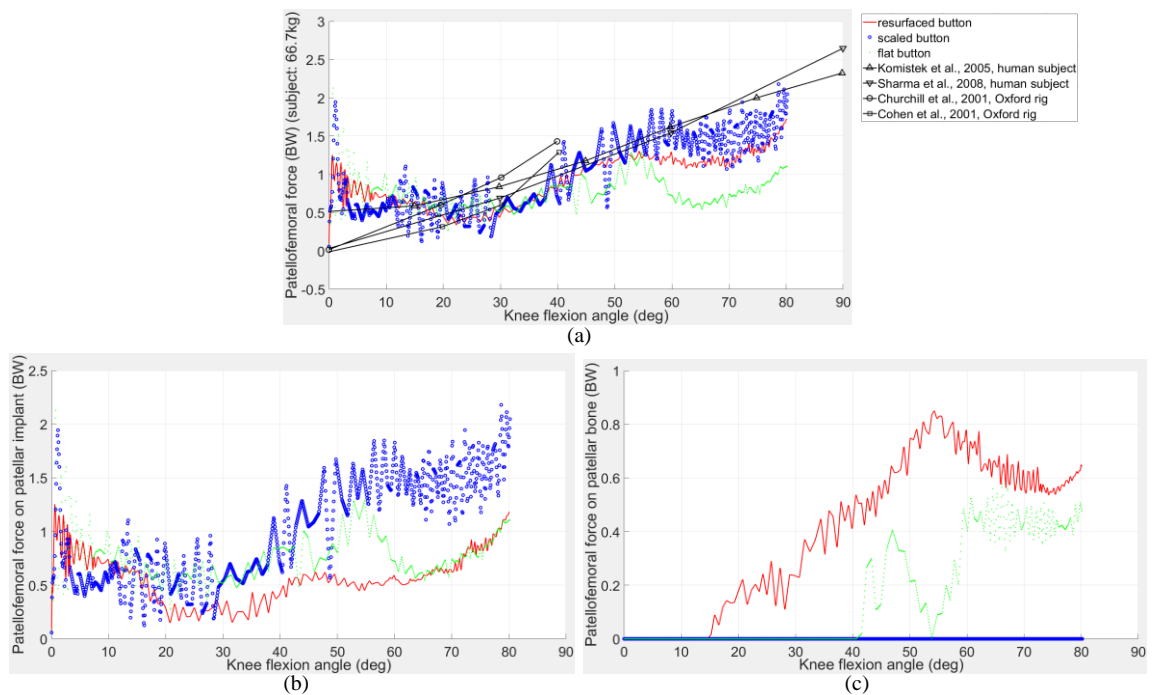
Figure 8. 4 Patellofemoral contact forces of three different patellar buttons: (a) total patellofemoral contact forces and results from other studies in black lines; (b) patellofemoral contact forces on the patellar buttons; (c) patellofemoral contact forces on the patellar bones

The patellofemoral joint contact forces were extracted and plotted in Figure 8. 4. The total patellofemoral contact force on each of the three patellar buttons was generally consistent with the results presented by Komistek et al. [173], Sharma et al. [174], Churchill et al. [176] and Cohen et al. [177] during the squatting motion. These forces increased sharply in the beginning, but increased slowly after 50° knee flexion. The sharp load increase in the initial knee flexion was caused by releasing the constraints on the two sides of the patella. Because the patellofemoral and tibiofemoral joints were initially unstable under the ligament forces, musculotendons and joint reaction forces, only the flexion-extension rotation and superior-inferior translation of the patella were allowed in order to make the simulation easily converge. Meanwhile, the internal-external rotation of the ankle

joint was also locked. At 0.04 seconds of the squatting simulation, the constraints on the patella and ankle joint were removed for the simulation model to reach a new balanced state through the contact pair self-adjustment. However, the initial constraints could have resulted in extra loads such as the internal-external moment on the ankle joint and imbalance forces between the medial and lateral PFCLs before the constraints were removed. Therefore, the sharp load increases on the patellofemoral joint occurred in the initial knee flexion of the simulation.

As shown in Figure 8. 4(b), the scaled-up patellar button resulted in larger load than both the small and the flat buttons due to the increased moment arm to the patellofemoral joint centre. There were larger load fluctuations in the scaled-up patellar button than other two models. It is mainly due to the larger radius of the button surface comparing to the femoral trochlear groove, which would result in two contact areas on the scaled-up button implant and further lead to jumping forces between two contact locations.

The contact forces between the patellar bone and femoral component were shown in Figure 8. 4(c). Since the scaled-up patellar button from the original smaller one was intended to cover the resected bone surface of the patella, there was no contact occurred between the patellar bone and the femoral implant during the squatting motion. Although the flat button was also scaled from the original one for the same purpose, there was still some bone uncovered in the proximal areas of the patella. The uncovered patella bone came into contact with the femoral component at 40° knee flexion, while, in the original patella implant model, it occurred at 15° knee flexion.

The patellofemoral relative motions are shown in Figure 8. 5. Larger motion fluctuations occurred in the CTKI model with scaled-up patellar implant, which had the least mediolateral range of motion (ROM) among the three patellar buttons as shown in Figure 8. 5(d). In Figure 8. 5(f), the scaled-up patella translated inferiorly and sharply to 30 mm in the early 5° knee flexion, and subsequently translated superiorly to 10 mm at about 13° knee flexion. The ROMs of the scaled-up patellar implant in both inferior-superior translation and internal-external rotation were larger than those of the other two buttons. There were few differences in the patellar flexion rotation, medial tilt and posterior translation. Since the radius of the trochlear groove of the customised femoral implant

is gradually decreasing like a normal knee joint, when the radius of the scaled patellar implant surface is larger than the radius of the trochlear groove, the two sides of patellar button would contact the femoral component, while there was no contact in the middle.
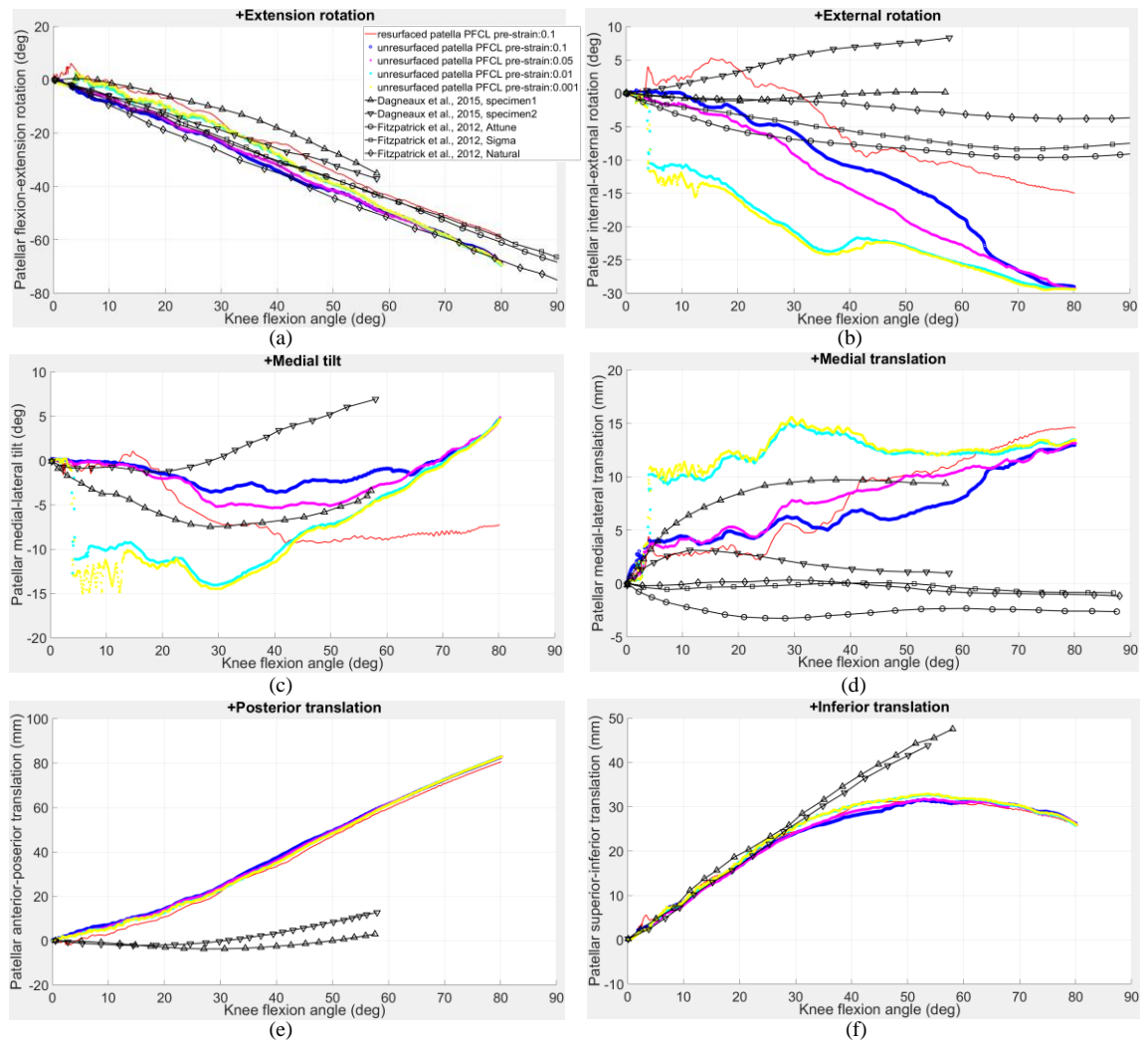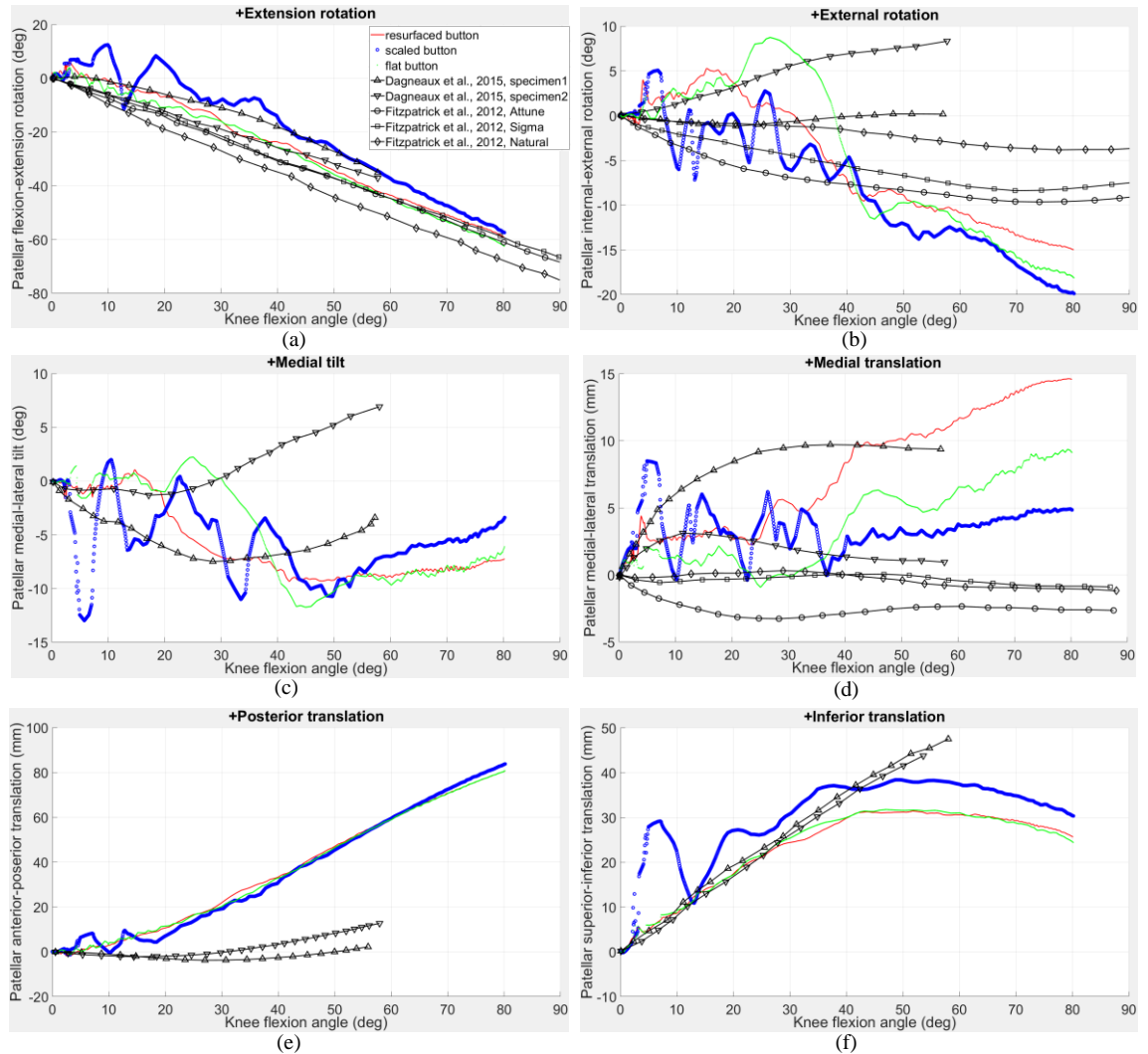

Figure 8. 5 Relative motions of the patella over the femoral component: (a) flexion-extension rotation; (b) external-internal rotation; (c) medial-lateral rotation; (d) medial-lateral translation; (e) anterior-posterior translation; (f) inferior-superior translation

8.4.3 Contact stresses of the patellofemoral joint
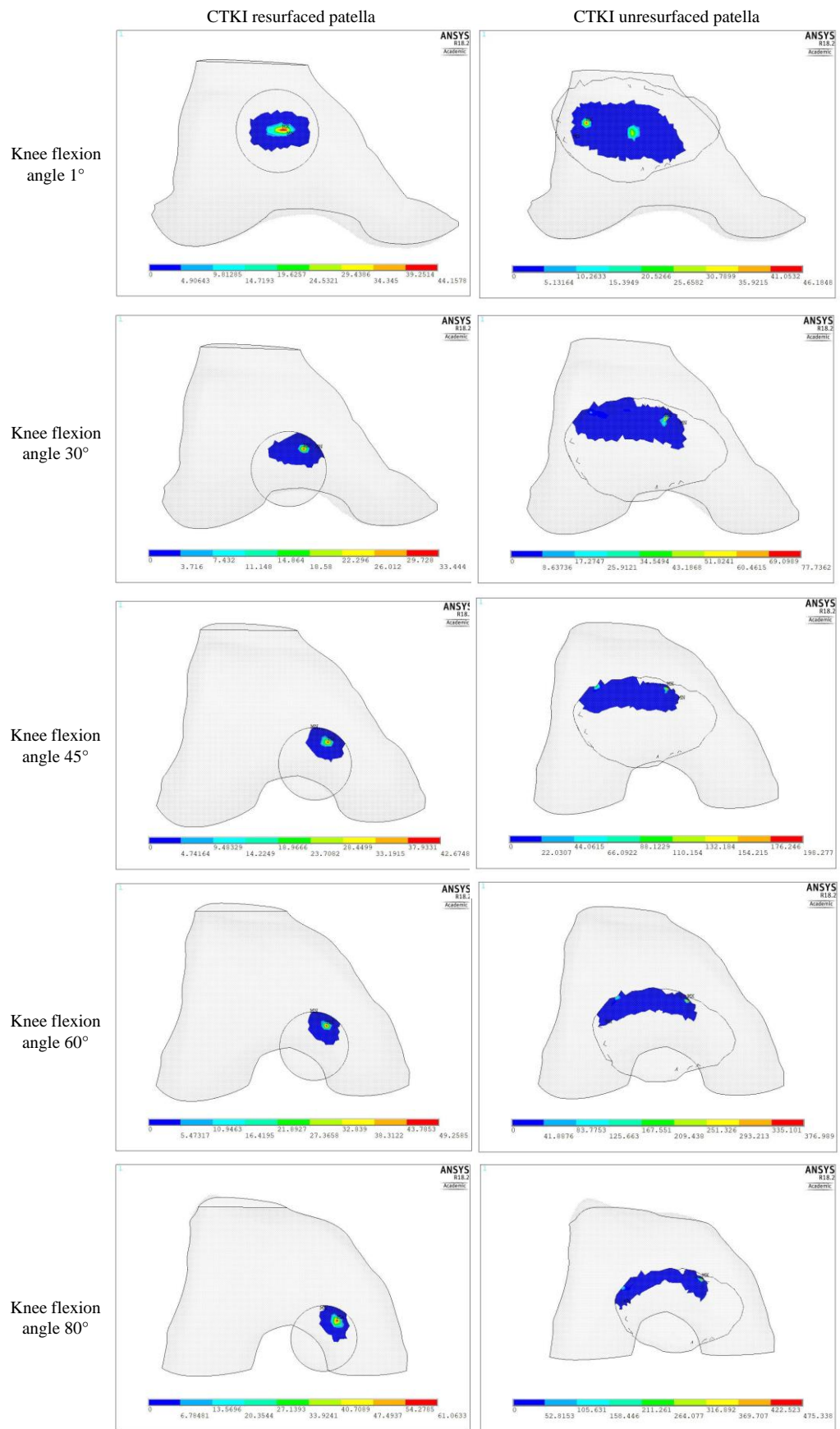
Figure 8. 6 Patellofemoral normal contact stresses of CTKIs with resurfaced and unresurfaced patellae

Scaled patellar button   Flat patellar button
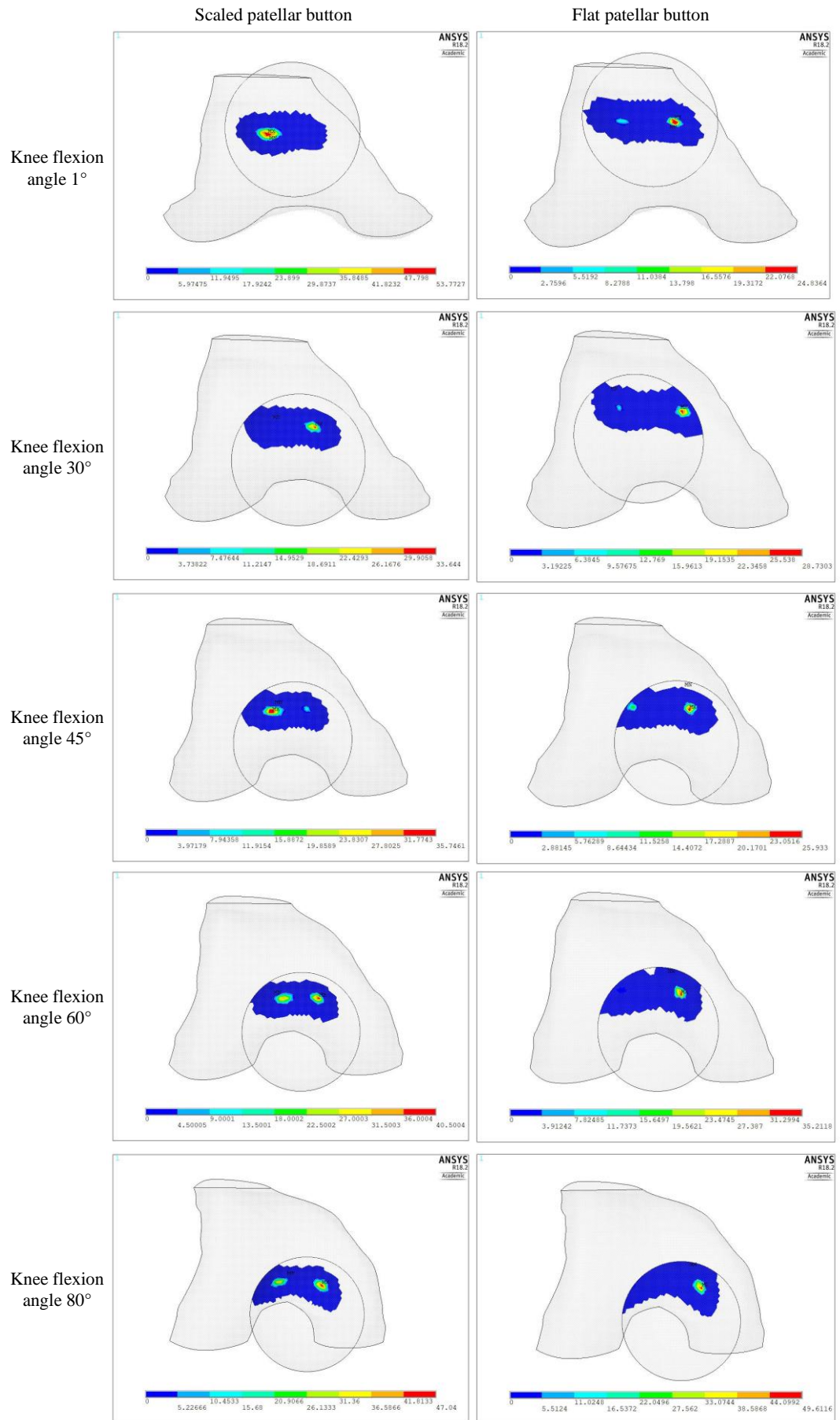
Figure 8. 7 Patellofemoral normal contact stresses of CTKIs with scaled and flat patellae

The patellofemoral contact stresses of CTKIs at the flexion angles of 0°, 30°, 45°, 60° and 80° were presented in Figure 8. 6 for the resurfaced and unresurfaced patellae. The contact locations on the resurfaced patella shifted from the centre of the patellar button to the superior right area along with the medial translation of the patella button, while the contact locations on the unresurfaced patella changed from its centre to the superior side due to the restraint of the saddle-shaped articular surface of the patella. The excessive high contact stresses were observed on the unresurfaced patella due to the incongruent surfaces of the patellofemoral joint and the unsmooth patellar articular surface, which was built from the CT images using 3D Slicer and consisted of several discontinuous small surfaces. The localised high stresses were then resulted.

The contact stresses on both scaled-up patellar buttons are shown in Figure 8. 7. The initial contact stress on the flat button was much smaller than that on the scaled patella due to the dual contact areas on the flat button. The contact area on the scaled-up button changed from a single contact area at the flexion angles of 0° and 30° to dual contact areas at the flexion angles of 45°, 60° and 80°. In contrast, the flat button changed from dual contact areas to a single contact area at around 60° knee flexion, however, as shown in Figure 8. 4, one of the contact areas on the flat button shifted from the button implant to the patellar bone at 40° knee flexion. Although the magnitudes of the contact stresses on both scaled patellar implant were very close, both exceeded the yield stress of the patellar implant material UHMWPE.

In order to reduce the contact stresses on the patellofemoral joint, one of the potential solutions would be the saddle-shaped patellar button, which is designed according to the shape of femoral trochlear groove. However, it is challenging to find a conforming shape of the patellar button due to the irregular shapes of femoral trochlear groove.

8.4.4 Further discussion

The laxity of PFCLs is important in the dynamic simulations of knee joint. If the initial strain of PFCLs is too small to provide enough pretensions on the patellofemoral joint, it would occur malposition or separation of patella from the femoral component during the dynamic simulations. In this study, due to the lack of relevant data about the mechanical properties of PFCLs, the ligament stiffness and initial strain of PFCLs were

assumed based on the knee collateral ligaments. The results of the patellofemoral and tibiofemoral joints could only show a trend of their responses to the design parameters through the nonlinear dynamic model. On the other hand, because of the complexity of human joint, it was very difficult to build a computer simulation model that could include too many joint details. It is necessary to find and identify the most important structures or elements in the future musculoskeletal models.

There were differences in the motions of patella internal rotation and medial tilt between the resurfaced and unresurfaced patellae. It is mainly caused by the different bearing surfaces between the button-shaped patellar implant and saddle-shaped natural patella. The patellar internal rotations in the resurfaced and unresurfaced patellae are different from the test results measured by Dagneaux et al. [175]. It might be due to the differences in boundary conditions and shapes of the femoral trochlear groove.

The size and shape of patellar button are important to the performance of patellofemoral joint. If the patellar button is too small to cover the exposed patella bone, the patella bone will contact the femoral component during the deep knee bend motion, which will cause the discomfort or pain on the knee joint. If the patellar button is large enough to cover the resection area of patella, the patellar medial translation is then reduced, however, the patellofemoral joint contact force become much fluctuating due to less conformity of the contact surfaces of the patellar button and femoral component.

The scaled patellar buttons were found to have two contact areas on the patellofemoral joint, while the original one had only one contact area. It is because the curvature of the scaled patellar implant was smaller than the original one. The contact stress was reduced on the scaled implant comparing to the original one that has a single contact area during the squat motion. However, the contact stresses on all patellar buttons in this study were larger than the yield stress of the patellar implant material, UHMWPE, making the implant susceptible to early wear failure.

There were limitations in the modelling of knee joint with the dynamic model. Firstly, the cartilage on the unresurfaced patella was not considered, which might affect the motions and loads of the patellofemoral joint. Secondly, the patellar articular surface was modelled as several small, irregular and unsmooth surfaces from the medical image

processing software, 3D Slicer, which resulted in the excessive patellofemoral contact stress. Thirdly, the initial location of the patellar button in relation to the femur was based on the CT images. The locations and the pre-strains of ligaments were referenced and assumed based on literature. However, despite these limitations, the dynamic FE model can predict a trend of patellofemoral joint motion and contact locations, and compare different designs of patellar button.

8.5 Conclusion

In this chapter, the influences of the unresurfaced patella and three patellar buttons on contact forces, relative motions and contact stresses of the patellofemoral joint were investigated. The dynamic FE simulations were driven by the patient-specific muscle and joint forces that were calculated through OpenSim for the squatting motion. Differences in the patellar internal rotation and medial tilt were found between the resurfaced and unresurfaced patellar buttons. The original patellar button resulted in contact between the patellar bone and the femoral component in addition to the contact between the patellar button and the femoral component. The scaled-up patellar button was able to avoid contact between patellar bone and femoral component and reduce the patellar medial translation. However, the scaled-up patellar button also resulted in larger patellofemoral force than other patellar buttons due to the increased moment arm. The patellofemoral forces on the scaled-up button were fluctuating due to the less conformity of the contact surfaces of patellar button and femoral component. The scaled-up patellar button implant was found to have two contact areas on the patellofemoral joint, while the original sized patellar button had only one contact area. In general, the computer models in this thesis can predict the trends of different designs of patellar button, though the FE model still needs to be improved.

Chapter 9

Discussion and conclusions

As a routine operation, total knee replacement (TKR) has been a very effective therapy to relieve knee pain and restore knee function for decades. However, the post-operative dissatisfactions have been widely reported. One of the two leading reasons are the residual pain caused by the overhang of total knee implants (TKIs) on bones, and another is the knee function limitation which might be attributed to the shapes of knee implants. Therefore, nowadays, improving TKI function and patient satisfaction, and restoring native anatomy and kinematics are becoming more important.

This research mainly investigated the performance of a customised total knee implant (CTKI) based on the knee anatomy to restore the knee kinematics of a specific subject. Its dynamic responses were compared with those of a traditional off-the-shelf knee implant under the same boundary conditions during a squatting motion. Effects of laxity of knee collateral ligaments, curvatures of tibial bearing surfaces, sizes and shapes of patellar implant buttons have also been studied.

9.1 Creating a CTKI model and its knee simulation model

9.1.1 Modelling the CTKI

In Chapter 3, a customised femoral component was created based on the shape of a patient's distal femur through the methods such as key feature point recognition, least-squares elliptical curve fitting and surface generation. The tibial bearing surface was created based on the geometry of femoral component condyles by defining an elliptical cutting guidance track in the longitudinal direction and two quadratic curves in the transverse direction for each condyle. The problem of femoral component overhang/underhang over the femur bone was solved by recognizing and obtaining the boundary key points on both femur and tibial resection surfaces. Through ANSYS Mechanical APDL modelling, the customised model can be modified by changing some parameters such as the long axis radius of longitudinal elliptical curve of tibial bearing surface and transverse quadratic coefficients.

9.1.2 Acquiring the patient-specific loading

To test specific dynamic responses of customised total knee implant (CTKI) under close-to-physiological muscles, a patient-specific musculoskeletal model was created in OpenSim in Chapter 4. Using the software tools such as inverse kinematics, residual reduction algorithm and static optimization, muscle forces of a patient-specific lower limb under a squatting motion were obtained.

Because the accuracy of the muscle forces is still challenging to be validated experimentally, muscle activation patterns for performing a daily activity are commonly used to compare with EMG measurement data. This can help find out approximate contributions or involvements of muscle bundles into desired activities. It is worth noting that the muscle model in this study is still a simplified model with many muscle parameters that were scaled from a generic model rather than measured from the subject. It could also affect the accuracy of simulations. In reality, it is not easy to measure realistic muscle parameters such as pennation angle, maximum isometric force and tendon slack length. Therefore, the calculated pattern of muscle forces in this study is only a numerous possible solution for driving the dynamic knee simulations rather than the absolute result that the subject muscles can produce. Those muscle forces were used to compare performances between the CTKIs and STKI. Comparing to the simplified experimental quadriceps loads and constant hamstring load used in other studies without considering the practical ground reaction forces during squatting motions, the muscle forces that were calculated under the effect of the measured ground reaction forces in this study are closer-to-human-physiological to test the dynamic responses of the customised total knee implant. However, the effect of variations of muscle parameters on muscle forces and joint loads should be considered in the musculoskeletal model in the future in order to make the patient-specific simulations more accurate.

OpenSim forward dynamic analysis with the detailed geometric shape of knee implant was attempted. However, the simulation trials failed due to the in-built simplified contact algorithm. The contact algorithm used in OpenSim is the elastic foundation which needs to know the approximate relative motions between two components. Contact forces are then calculated based on the interpenetration depths between two components in a self-

defined contact stiffness. No penetration tolerance or internal force balance was considered in this algorithm to obtain a reasonable result of relative contact position. Since the relative motion of resurfaced tibiofemoral joint could not be adjusted under the muscle and joint reaction forces derived from the motion of pre-resurfaced knee joint, the excessive contact forces that could not balance the muscle forces and joint forces, resulted in the forward dynamic simulation in OpenSim to diverge with wrong joint angles.

Therefore, instead of conducting dynamic performance assessments of CTKI in OpenSim directly, a knee simulation model was built in ANSYS Mechanical APDL to test contact responses of the knee implant components under the patient-specific muscle forces and ankle joint reaction loads that were obtained in OpenSim. The muscle insertion points in the OpenSim model were also used to help locate specific muscle bundles and direct the muscle forces in a closer-to-physiological way.

9.1.3 Building the dynamic knee simulation model

In Chapter 5, a transient dynamic model of CTKI was created based on the principles of Oxford knee rig and Kansas knee simulator. Twenty-three muscles in a left lower limb were recruited with the referenced muscle insertion points from the OpenSim musculoskeletal model. To provide dynamic balance, knee joint ligaments such as collateral ligaments and cruciate ligaments were also included in this model with their nonlinear spring stiffness and pre-strains referenced from literature. Actuator element in ANSYS Mechanical APDL was used to apply time-varying muscle forces to the quadriceps bundles that connect patella and femur, while a rotating-slider mechanism was used to apply muscle forces to those muscles that has only one end attached to either femur or tibia. The wrapping effect of the quadriceps bundles around the femoral component was created by discretizing the springs into several segments of springs with several nodes. Node-to-surface contact element was used to realize the wrapping effect when the knee joint flexes to a certain degree. Euler angles and rotation matrix were applied to track and record the relative motions between femur and tibia and between femur and patella. The material properties of the femoral component, tibial insert and tibial tray were set as linear for the consideration of computational cost and convergence difficulty.

This knee simulation model can provide a platform for assessing the dynamic responses of all kinds of TKIs by applying more recruited time-varying muscle forces and joint reaction loads during squatting motion. Both kinetic and kinematic results of tibiofemoral and patellofemoral joints can be obtained. Both the muscle insertion locations and the parameters of lower limb can be adjusted from person to person.

Due to limited functionality in ANSYS software, control loop or feedback was not used in the dynamic FE simulations in this study. In the future study, active control of muscle and joint reaction forces should be included in the dynamic analysis of knee implants rather than just tracking the known motion or applying known muscle and joint reaction forces without motion tracking. Based on output feedbacks such as hip flexion angle, adjustments should be applied on the inputs of muscle, joint reaction forces and the lower limb motion acquired from the inverse kinematics analysis in each time step.

9.2 Comparison between the CTKI and the traditional knee implant

In Chapter 6, the dynamic responses of CTKI were simulated under three treatment scenarios of cruciate ligament (CL): both CLs retained, anterior cruciate ligament (ACL) removed and both CLs removed. An off-the-shelf symmetric total knee implant (STKI) was simulated only with both CLs retained for comparison analysis. The CTKI with both CLs retained showed larger ranges of femoral external rotation and posterior translation than the STKI did. These two motions of CTKI were also in good agreement with those of referenced healthy knees. Regarding the dynamic tibiofemoral compressive forces, there were little differences in the CTKI model under the three CL treatment scenarios. The trends and magnitudes were generally consistent with other experimental and simulation results. However, for the STKI model, smaller tibiofemoral compressive forces and more even medial-lateral load ratios above 50° knee flexion were shown during the squatting simulation due to a better articular conformity. Due to its restricted mobility, smaller collateral ligament forces and shorter elongations were also obtained.

The installation of the STKI was considered with the alignment of femoral and tibial mechanical axes, while the alignment of mechanical axes in the CTKIs was neglected to keep the original knee joint angle of subject in the CT data and corresponding

musculoskeletal model that was scaled from the OpenSim generic model. It is probably one of the reasons why the medial-lateral load distributions presented in the CTKIs were larger than those of the STKI. In the future, the alignment of mechanical axes in CTKI designs will be varied to investigate how the dynamic responses of CTKIs will be affected.

The fluctuations of simulated results in this study might be due to lack of adduction-abduction torques in the ankle and hip joints. The adduction-abduction torques were usually neglected in the knee simulators or corresponding computer simulations. In the initial simulations of the dynamic FE model, the adduction-abduction torques were applied on the ankle and hip joints or one of these joints. But all of them failed with one side femoral condyle lift-off from the tibial bearing due to the load imbalance of system in the frontal/coronal plane. Therefore, a feedback control loop should be introduced in the dynamic FE simulations. The calculated muscle forces from other simulation software or other methods should be revised and updated according to instantaneously measured variables such as the knee or hip flexion angle. Through this method, it is possible to reduce the fluctuations of simulated tibiofemoral compressive forces and relative motions; and take into account the adduction-abduction torques into the hip and ankle joints to make the simulation more realistic.

9.3 Influence of the tibial bearing curvatures of the CTKI

In Chapter 7, influence of several tibial bearing curvatures of CTKI on the dynamic responses of knee joint was investigated. The transverse curvatures of the tibial bearing of the CTKI design had six combinations, while longitudinal curvature of the tibial bearing had three values. The material property of tibial insert was changed from linear to nonlinear for both CTKI and STKI designs. The spring stiffness of patellar ligament bundles was also nonlinear. Under the same longitudinal curvature, the CTKIs with relative flat tibial bearing showed 2 mm larger in the femoral mediolateral translation than the ones with curved tibial bearing surfaces. The differences of femoral external rotations were less than 2°. The longitudinal curvatures of tibial bearing were found to mainly affect the adduction-abduction rotation of femoral component in relation to the tibial counterpart.

Similar to the results of CTKI with the linear material property of tibial insert in Chapter 6, the femoral external rotation of the CTKIs was in good agreement with the measured healthy knees. Although the femoral posterior translations of CTKIs were greater than the referenced range of healthy knees in this study, they were still in the range of normal knees presented in another published literature. In contrast, the STKI simulated under the same conditions experienced relatively constant femoral external rotation, posterior translation and mediolateral translation.

In terms of forces, the CTKIs did not show comparable or even smaller tibiofemoral compressive forces than the STKI above 50° knee flexion. It was mainly due to the less conforming geometric shapes between the CTKI femoral and tibial components, which increased the involvements of CLLs and ACL in the tibiofemoral relative motions. In contrast, both ACL bundles of the STKI became relaxed quickly in the earlier flexion angles.

The contact stresses of tibiofemoral joint of the CTKI design and the STKI were also compared. The contact stresses of the CTKI increased with the increasing knee flexion angle, and reached 68 MPa at the maximum flexion angle of 80°, while the tibiofemoral contact stress of the STKI increased to 50 MPa at 60° knee flexion and then decreased to 25 MPa at the maximum flexion angle. It might be due to the ACL bundles being not subjected to loads after 45° knee flexion in the STKI model.

The tibiofemoral contact stresses of the CTKI in the initial knee flexion and late knee flexion angles were found to be larger than those of the STKI. The larger contact stresses of the CTKI in the early stage are mainly due to the less congruency between tibiofemoral components. Although decreasing the congruency between tibiofemoral components for mimicking the anatomic knee joint could help patient's knee recover to its normal kinematics, larger contact stresses were also resulted on the articular surfaces due to the decreased contact areas. The larger contact stress of the CTKI than that of the STKI also occurred in the knee flexion angle above 60°. This is mainly caused by the elongated bundles of ACL in the CTKI models. They were produced by the wider range of motions of CTKIs such as the femoral external rotation and posterior translation that could lead to the larger elongations of collateral and cruciate ligaments. Therefore, it can be concluded that the congruency between femoral and tibial implants affect not only

the knee kinematics but also the knee forces. The congruency and mobility of TKIs are essentially contradictory. The better tibiofemoral joint congruency is, the smaller contact stresses and ligament forces of knee joint are produced. But meanwhile, the knee mobility is reduced making patient move unnaturally and uncomfortably.

Although the STKI model resulted in smaller contact stresses than the CTKI, the contact stresses of both designs were larger than the yield stress of UHMWPE material during the squatting simulations. Large contact stresses could lead to early wear problem. The UHMWPE debris particles could further induce osteolytic reactions leading to the loosening and failure of implant. The larger contact stresses than the material's yield strength were also reported in other published papers. Therefore, increasing the contact surface between tibiofemoral joint and keeping its asymmetric characteristic would be a research direction in the future. One way to potentially increase the contact areas is to create simple shapes of femoral and tibial components but still based on the patient-specific knee joint characteristics. Another way is to combine the design method of CTKI in this study with the design method proposed by Peter S. Walker from the Department of Orthopaedic Surgery, New York University. The femoral component can be created through the methods of key feature point recognition and least squares elliptical curve fitting, while the tibial component can be created using drape function over the lower surface of multiple rotating positions of the femoral component.

9.4 Influence of the patellar button component

In Chapter 8, influences of an unresurfaced patella and resurfaced patellar buttons with different sizes and curvatures were investigated. Differences in the patellar internal rotation and medial tilt between the resurfaced and unresurfaced patellae were observed. They might be caused by the geometric difference between the button-shaped and the saddle-shaped patellar surfaces. The differences between this study results and other research results might be due to the different loading boundary conditions and geometric shapes of femoral trochlear groove. There was not much difference in the patellofemoral contact forces between two patella components.

The laxity of patellofemoral collateral ligaments (PFCLs) was simulated in the unresurfaced patella model. When the initial strain of PFCLs was too small to provide

enough pretensions on the patellofemoral joint, the relative motions between the patellofemoral components would diverge during the dynamic simulations with either malposition or separating of patella from the femoral component.

The sizes and shapes of patellar button component influenced the mechanical performances of patellofemoral joints. If the patellar button was too small to cover the exposed patella bone, the patella bone would be in contact with the femoral component during the deep knee bend motion, which could cause discomfort or pain on the knee joint. If the patellar button was large enough to cover the resection area of patella, the patellar medial translation could be effectively reduced, however, the patellofemoral joint contact force became more fluctuating due to the less congruency of contact surfaces between the patellar button and the femoral component.

9.5 Limitation of the ligament pre-strains

In Chapters 5 and 6, the UHMWPE material property of tibial insert was specified as linear elasticity modulus, the ligament pre-strains were referenced from the literature that was highly cited by other researchers. In Chapters 7 and 8, when the material property of tibial insert was changed from linear to nonlinear, applying the same pre-strain values on the knee collateral ligaments resulted in single-side-condylar lift-off. In order to achieve the initial stability of knee joint, the pre-strains of all collateral ligament bundles were increased to 0.1. That is the reason why the tibiofemoral compressive forces calculated in the nonlinear tibial insert model were larger than that in the linear tibial insert models. Due to the lack of laxity tests of the patient-specific knee collateral ligaments and the large number of iterative solutions to find the ligament pre-strains and spring stiffnesses that could result in the required joint rotations and translations under certain experimental loads, therefore all the pre-strains of the knee joint ligaments were either based on values from literature or increased until the solution could converge.

9.6 Conclusions

Through the computer simulations, the CTKI has shown its great potential to help patient's knee to move closer to the healthy knee motion range and characteristics in comparison with one traditional STKI model under the same boundary conditions, even

though the larger tibiofemoral compressive forces and medial-lateral load ratio were produced in the CTKI models than STKI model above 50° knee flexion. The ANSYS dynamic FE knee simulation model developed in this study was able to predict the dynamic responses of different designs of total knee implants under the same boundary conditions and allow designers and patients to understand the differences of performances of various total knee implants.

Chapter 10

Future work

The angle between the two tibial bearing longitudinal guide curves could be investigated. The tibiofemoral relative motions, especially the femoral external rotation, might be affected by this angle.

To reduce the contact stresses of tibiofemoral joint and prolong the longevity of the CTKIs, more regular articular shapes should be investigated. With reference to the ConforMIS design method, three J-shaped curves in the sagittal plane can be firstly determined through optimisation, then different profiles that could be swept along the J-shaped curves can be investigated to find a compromising solution between the knee mobility and congruency for wear problem.

Another possible solution for increasing the contact area of knee joint is to use the design method for the femoral component in this thesis, but to build the tibial bearing shapes by using the method of drape function, which is to envelope the lower surface of the rotating positions of femoral component.

The alignment of tibiofemoral mechanical axes should be investigated in the design of CTKIs to reduce the uneven distribution of joint forces between the femoral and tibial components.

The muscle forces should be controlled and adjusted at each numerical iteration step, and the knee flexion angles can be used as one of the objective functions.

Muscle parameters, activations and forces should be studied and applied on the knee simulator. Future experiments should be set up with consideration of the effect of the active muscle forces.

Other daily activities such as walking, running, and chair rising should be simulated for the design of CTKIs.

References

1. Hamilton DF, Howie CR, Burnett R, et al. Dealing with the predicted increase in demand for revision total knee arthroplasty: challenges, risks and opportunities. *The Bone & Joint Journal* 2015; 97-B: 723–728.

2. Kurtz S. Projections of Primary and Revision Hip and Knee Arthroplasty in the United States from 2005 to 2030. *The Journal of Bone and Joint Surgery (American)* 2007; 89: 780.

3. Baker PN, van der Meulen JH, Lewsey J, et al. The role of pain and function in determining patient satisfaction after total knee replacement: DATA FROM THE NATIONAL JOINT REGISTRY FOR ENGLAND AND WALES. *The Journal of Bone and Joint Surgery British volume* 2007; 89-B: 893–900.

4. Nam D, Nunley RM, Barrack RL. Patient dissatisfaction following total knee replacement: a growing concern? *The Bone & Joint Journal* 2014; 96-B: 96–100.

5. Zeller IM, Sharma A, Kurtz WB, et al. Customized versus Patient-Sized Cruciate-Retaining Total Knee Arthroplasty: An In Vivo Kinematics Study Using Mobile Fluoroscopy. *The Journal of Arthroplasty* 2017; 32: 1344–1350.

6. Bourne RB, Chesworth BM, Davis AM, et al. Patient Satisfaction after Total Knee Arthroplasty: Who is Satisfied and Who is Not? *Clinical Orthopaedics and Related Research* 2010; 468: 57–63.

7. Murakami K, Hamai S, Okazaki K, et al. Knee kinematics in bi-cruciate stabilized total knee arthroplasty during squatting and stair-climbing activities. *Journal of Orthopaedics* 2018; 15: 650–654.

8. Mahoney OM, Kinsey T. Overhang of the Femoral Component in Total Knee Arthroplasty: Risk Factors and Clinical Consequences: *The Journal of Bone and Joint Surgery-American Volume* 2010; 92: 1115–1121.

9. Bonnin MP, Schmidt A, Basiglini L, et al. Mediolateral oversizing influences pain, function, and flexion after TKA. *Knee Surgery, Sports Traumatology, Arthroscopy* 2013; 21: 2314–2324.

10. Walker PS. The design and pre-clinical evaluation of knee replacements for osteoarthritis. *Journal of Biomechanics* 2015; 48: 742–749.

11. CONFORMIS Custom-made total and partial knee replacements. [Internet]. c2004-06-23 [updated 2019 February 11]; [cited 2019 March]. Available from: https://www.conformis.com/surgeon-resource-center/products/itotal-cr/.

12. Patil S, Bunn A, Bugbee WD, et al. Patient-specific implants with custom cutting blocks better approximate natural knee kinematics than standard TKA without custom cutting blocks. *The Knee* 2015; 22: 624–629.

References

13. SimTK: Grand Challenge Competition to Predict In Vivo Knee Loads: Project Home. [Internet]. c2004-12-10 [updated 2018 August 27]; [cited 2019 March]. Available from: https://simtk.org/projects/kneeloads.

14. Fregly BJ, Besier TF, Lloyd DG, et al. Grand challenge competition to predict in vivo knee loads. *Journal of Orthopaedic Research* 2012; 30: 503–513.

15. Knee/Wikipedia. [Internet]. c2001-01-13 [updated 2015 December 12]; [cited 2019 March]. Available from: https://en.wikipedia.org/wiki/Knee.

16. Patella, meniscus, cruciate ligament location/anatomynote. [Internet]. c2017-09-26 [updated 2018 September 21]; [cited 2019 March]. Available from: https://www.anatomynote.com/human-anatomy/knee/patella-meniscus-cruciate-ligament-location/.

17. Menisci on tibial plateau. [Internet]. c2011-05-15 [updated 2019 April 22]; [cited 2019 March]. Available from: http://www.specialistkneesurgeon.com/conditions/cartilage-tear.

18. menisci in isomeric view. [Internet]. c2015-11-26 [updated 2019 July 26] ; [cited 2019 March]. Available from: https://thedoctorsofpt.com/pt-versus-surgery-meniscus-tear/.

19. Patellofemoral Joint/Physiopedia. [Internet]. c2008-03-09 [updated 2015 September 09]; [cited 2019 March]. Available from: https://www.physio-pedia.com/Patellofemoral_Joint.

20. Knee joint anatomy lateral view/anatomynote. [Internet]. c2017-09-26 [updated 2018 September 21]; [cited 2019 March]. Available from: https://www.anatomynote.com/human-anatomy/knee/knee-joint-anatomy-lateral-view/.

21. Kakarlapudi TK, Bickerstaff DR. Knee instability: isolated and complex. *British Journal of Sports Medicine* 2000; 34: 394–400.

22. Maletsky LP. *Validation of the next generation knee simulator*. Doctoral thesis. Purdue University, 1999.

23. Human lower extremity muscles. [Internet]. c2018-11-21 [updated 2019 April 16]; [cited 2019 March]. Available from: http://www.days-eye.com/knee-muscles-anatomy-diagram/band-hamstring-tendon-quadriceps-knee-muscles-patella-lateral-patellar-retinaculum-tibia-fibula-medial-meniscus-beautiful-study/.

24. Van De Graaff. *Human Anatomy 6th edition*. McGraw-Hill Publishing Company, 2002.

25. Nordin M, Frankel VH. *Basic Biomechanics of the Musculoskeletal System*. 3rd ed. Philadelphia, USA: Lippincott Williams & Wilkins, 2001.

26. Belvedere C, Leardini A, Giannini S, et al. Does medio-lateral motion occur in the normal knee? An in-vitro study in passive motion. *Journal of Biomechanics* 2011; 44: 877–884.

27. Freeman MAR, Pinskerova V. The Movement of the Knee Studied by Magnetic Resonance Imaging: *Clinical Orthopaedics and Related Research* 2003; 410: 35–43.

28. Before and after total knee replacement surgery. [Internet]. [cited 2019 March]. Available from: https://medlineplus.gov/ency/article/002974.htm.

29. Knee parts and materials, University of Missouri Health Care. [Internet]. c1998-01-16 [updated 2019 July 01]; [cited 2019 March]. Available from: https://www.muhealth.org/conditions-treatments/orthopaedics/hip-and-knee/knee-surgery/knee-parts-and-materials.

30. Knee Replacement Implants, OrthoInfo. [Internet]. c1995-04-10 [updated 2019 April 11]; [cited 2019 March]. Available from: https://orthoinfo.aaos.org/en/treatment/knee-replacement-implants/.

31. Akasaki Y, Matsuda S, Shimoto T, et al. Contact Stress Analysis of the Conforming Post-Cam Mechanism in Posterior-Stabilized Total Knee Arthroplasty. *The Journal of Arthroplasty* 2008; 23: 736–743.

32. Van Duren B, Pandit H, Zavatsky AB, et al. POSTERIOR STABILISED TKA: IS THE CAM-POST MECHANISM EFFECTIVE? *52nd Annual Meeting of the Orthopaedic Research Society*; 1.

33. Mazzucchelli L, Deledda D, Rosso F, et al. Cruciate retaining and cruciate substituting ultra-congruent insert. *Annals of Translational Medicine* 2016; 4: 7.

34. Blunn GW, Joshi AB, Minns RJ, et al. Wear in retrieved condylar knee arthroplasties. *The Journal of Arthroplasty* 1997; 12: 281–290.

35. Lützner J, Firmbach F-P, Lützner C, et al. Similar stability and range of motion between cruciate-retaining and cruciate-substituting ultracongruent insert total knee arthroplasty. *Knee Surgery, Sports Traumatology, Arthroscopy* 2015; 23: 1638–1643.

36. Parcells B. TKA-PRIMARY DESIGN. [Internet]. c2016-03-19 [updated 2019 March 04]; [cited 2019 March]. Available from: http://hipandkneebook.com/tka-implants/2017/3/15/tka-primary-design (2017).

37. Victor J, Mueller JKP, Komistek RD, et al. In Vivo Kinematics after a Cruciate-substituting TKA. *Clinical Orthopaedics and Related Research®* 2010; 468: 807–814.

38. Knee/Orthopedic Devices/Healthcare Professionals/MicroPort®. [Internet]. [cited 2019 March]. Available from: http://www.microport.com/en/product.php?curr_page=product_detail&id=51.

39. Kim Y-H, Yoon S-H, Kim J-S. The long-term results of simultaneous fixed-bearing and mobile-bearing total knee replacements performed in the same patient.pdf. *Journal of Bone and Joint Surgery*; 89-B, No.10.

40.   Lu Y-C, Huang C-H, Chang T-K, et al. Wear-pattern analysis in retrieved tibial inserts of mobile-bearing and fixed-bearing total knee prostheses. *The Journal of Bone and Joint Surgery British volume* 2010; 92-B: 500–507.

41.   Understanding Implants in Knee and Hip Replacement. [Internet]. c1994-02-10 [updated 2019 June 25]; [cited 2019 March]. Available from: https://www.hss.edu/conditions_understanding-implants-in-knee-and-hip-replacement.asp#TypesKnee.

42.   Howell SM, Hull ML. Kinematic Alignment in Total Knee Arthroplasty. Chapter 121 in *Insall & Scott Surgery of the Knee*. Elsevier, pp. 1255–1268.

43.   Ji H-M, Han J, Jin DS, et al. Kinematically aligned TKA can align knee joint line to horizontal. *Knee Surgery, Sports Traumatology, Arthroscopy* 2016; 24: 2436–2441.

44.   Zavatsky AB. A kinematic-freedom analysis of a flexed-knee-stance testing rig. *Journal of biomechanics* 1997; 30: 277–280.

45.   Bourne R, Goodfellow JW, O'Connor JJ. A functional analysis of various knee arthroplasties. In: *Transactions of the 24th Annual Orthopaedic Research Society*. Dallas: Orthopaedic Research Society (ORS), 1978.

46.   Varadarajan KM, Harry RE, Johnson T, et al. Can in vitro systems capture the characteristic differences between the flexion–extension kinematics of the healthy and TKA knee? *Medical Engineering & Physics* 2009; 31: 899–906.

47.   Guess TM, Maletsky LP. Computational modelling of a total knee prosthetic loaded in a dynamic knee simulator. *Medical Engineering & Physics* 2005; 27: 357–367.

48.   Maletsky LP, Hillberry BM. Simulating Dynamic Activities Using a Five-Axis Knee Simulator. *Journal of Biomechanical Engineering* 2005; 127: 123.

49.   Maletsky LP, Hillberry BM. Loading Evaluation of Knee Joint During Walking Using the Next Generation Knee Simulator. *Advances in Bioengineering* 2000; 48: 91–92.

50.   Guess TM, Maletsky LP. Computational Modeling Of A Dynamic Knee Simulator For Prediction Of Joint Loading. Sonesta Beach Resort in Key Biscayne, Florida: American Society of Mechanical Engineers ASME, 2003, pp. 0859–0860.

51.   Guess TM, Maletsky LP. Computational Modeling of a Dynamic Knee Simulator for Reproduction of Knee Loading. *Journal of Biomechanical Engineering* 2005; 127: 1216.

52.   Baldwin MA, Clary C, Maletsky LP, et al. Verification of predicted specimen-specific natural and implanted patellofemoral kinematics during simulated deep knee bend. *Journal of Biomechanics* 2009; 42: 2341–2348.

53.   Baldwin MA, Clary CW, Fitzpatrick CK, et al. Dynamic finite element knee simulation for evaluation of knee replacement mechanics. *Journal of Biomechanics* 2012; 45: 474–483.

54.   Bloemker KH, Guess TM, Maletsky L, et al. Computational knee ligament modeling using experimentally determined zero-load lengths.pdf. *The open biomedical engineering journal* 2012; 6: 33–41.

55.   Verstraete MA, Victor J. Possibilities and limitations of novel in-vitro knee simulator. *Journal of Biomechanics* 2015; 48: 3377–3382.

56.   Walker PS, Blunn GW, Broome DR, et al. A knee simulating machine for performance evaluation of total knee replacements.pdf. *Journal of Biomechanics* 1997; 30, No. 1: 83–89.

57.   Godest AC, Beaugonin M, Haug E, et al. Simulation of a Knee Joint Replacement During a Gait Cycle Using Explicit Finite Element Analysis. *Journal of biomechanics* 2002; 35: 267–275.

58.   Forlani M. *A new test rig for in-vitro evaluation of the knee joint behaviour*. Doctoral thesis. University of Bologna, 2015.

59.   Fitzpatrick CK, Rullkoetter PJ. Estimating total knee replacement joint load ratios from kinematics. *Journal of Biomechanics* 2014; 47: 3003–3011.

60.   Fitzpatrick CK, Komistek RD, Rullkoetter PJ. Developing simulations to reproduce in vivo fluoroscopy kinematics in total knee replacement patients. *Journal of Biomechanics* 2014; 47: 2398–2405.

61.   Fitzpatrick CK, Maag C, Clary CW, et al. Validation of a new computational 6-DOF knee simulator during dynamic activities. *Journal of Biomechanics* 2016; 49: 3177–3184.

62.   Bersini S, Sansone V, Frigo CA. A dynamic multibody model of the physiological knee to predict internal loads during movement in gravitational field. *Computer Methods in Biomechanics and Biomedical Engineering* 2016; 19: 571–579.

63.   Shu L, Yamamoto K, Yao J, et al. A subject-specific finite element musculoskeletal framework for mechanics analysis of a total knee replacement. *Journal of Biomechanics* 2018; 77: 146–154.

64.   Walker PS, Lowry MT, Kumar A. The Effect of Geometric Variations in Posterior-stabilized Knee Designs on Motion Characteristics Measured in a Knee Loading Machine. *Clinical Orthopaedics and Related Research* 2014; 472: 238–247.

65.   Willing R, Kim IY. Design optimization of a total knee replacement for improved constraint and flexion kinematics. *Journal of Biomechanics* 2011; 44: 1014–1020.

66.   Gerus P, Sartori M, Besier TF, et al. Subject-specific knee joint geometry improves predictions of medial tibiofemoral contact forces. *Journal of Biomechanics* 2013; 46: 2778–2786.

67. Pandit H, Ward T, Hollinghurst D, et al. Influence of surface geometry and the cam-post mechanism on the kinematics of total knee replacement. *Journal of Bone & Joint Surgery, British Volume* 2005; 87: 940–945.

68. Clary CW, Fitzpatrick CK, Maletsky LP, et al. The influence of total knee arthroplasty geometry on mid-flexion stability: An experimental and finite element study. *Journal of Biomechanics* 2013; 46: 1351–1357.

69. Fitzpatrick CK, Rullkoetter PJ. Influence of patellofemoral articular geometry and material on mechanics of the unresurfaced patella. *Journal of Biomechanics* 2012; 45: 1909–1915.

70. Simpson DJ, Gray H, D'Lima D, et al. The effect of bearing congruency, thickness and alignment on the stresses in unicompartmental knee replacements. *Clinical Biomechanics* 2008; 23: 1148–1157.

71. Rawlinson JJ, Bartel DL. Flat medial–lateral conformity in total knee replacements does not minimize contact stresses. *Journal of biomechanics* 2002; 35: 27–34.

72. Walker PS. Application of a novel design method for knee replacements to achieve normal mechanics. *The Knee* 2014; 21: 353–358.

73. Harrysson OL, Hosni YA, Nayfeh JF. Custom-designed orthopedic implants evaluated using finite element analysis of patient-specific computed tomography data: femoral-component case study. *BMC Musculoskeletal Disorders* 2007; 8: 91.

74. Li K, Tashman S, Fu F, et al. Automating Analyses of the Distal Femur Articular Geometry Based on Three-Dimensional Surface Data. *Annals of Biomedical Engineering* 2010; 38: 2928–2936.

75. Sholukha V, Chapman T, Salvia P, et al. Femur shape prediction by multiple regression based on quadric surface fitting. *Journal of Biomechanics* 2011; 44: 712–718.

76. Cerveri P, Marchente M, Bartels W, et al. Automated Method for Computing the Morphological and Clinical Parameters of the Proximal Femur Using Heuristic Modeling Techniques. *Annals of Biomedical Engineering* 2010; 38: 1752–1766.

77. Cerveri P, Manzotti A, Confalonieri N, et al. Automating the design of resection guides specific to patient anatomy in knee replacement surgery by enhanced 3D curvature and surface modeling of distal femur shape models. *Computerized Medical Imaging and Graphics* 2014; 38: 664–674.

78. Wismans J. A three-dimensional mathematical model of the human knee joint. 1980. DOI: 10.6100/ir155825.

79. Blankevoort L, Kuiper JH, Huiskes R, et al. Articular contact in a three-dimensional model of the knee. *Journal of Biomechanics* 1991; 24: 1019–1031.

80. Blankevoort L, Huiskes R. Ligament-Bone Interaction in a Three-Dimensional Model of the Knee. *Journal of Biomechanical Engineering* 1991; 113: 263.

81. Galbusera F, Freutel M, Dürselen L, et al. Material Models and Properties in the Finite Element Analysis of Knee Ligaments: A Literature Review. *Frontiers in Bioengineering and Biotechnology* 2014. DOI: 10.3389/fbioe.2014.00054.

82. Beidokhti HN, Janssen D, van de Groes S, et al. The influence of ligament modelling strategies on the predictive capability of finite element models of the human knee joint.pdf. *Journal of Biomechanics* 2017; 65: 1–11.

83. Escamilla RF. Knee biomechanics of the dynamic squat exercise: *Medicine and Science in Sports and Exercise* 2001; 127–141.

84. Delp SL, Anderson FC, Arnold AS, et al. OpenSim: Open-Source Software to Create and Analyze Dynamic Simulations of Movement. *IEEE Transactions on Biomedical Engineering* 2007; 54: 1940–1950.

85. Delp SL, Loan JP. A graphics-based software system to develop and analyze models of musculoskeletal structures. *Computers in Biology and Medicine* 1995; 25: 21–34.

86. Delp SL, Loan JP. A computational framework for simulating and analyzing human and animal movement. *Computing in Science & Engineering* 2000; 2: 46–55.

87. Delp SL, Loan JP, Hoy MG, et al. An interactive graphics-based model of the lower extremity to study orthopaedic surgical procedures. *IEEE Transactions on Biomedical Engineering* 1990; 37: 757–767.

88. Sherman MA, Seth A, Delp SL. Simbody: multibody dynamics for biomedical research. *Procedia IUTAM* 2011; 2: 241–261.

89. Reinbolt JA, Seth A, Delp SL. Simulation of human movement: applications using OpenSim. *Procedia IUTAM* 2011; 2: 186–198.

90. Mansouri M, Reinbolt JA. A Platform for Dynamic Simulation and Control of Movement Based on Opensim and Matlab. *Journal of Biomechanics* 2012; 45: 1517–1521.

91. DeMers MS, Pal S, Delp SL. Changes in tibiofemoral forces due to variations in muscle activity during walking: TIBIOFEMORAL FORCES AND MUSCLE ACTIVITY. *Journal of Orthopaedic Research* 2014; 32: 769–776.

92. Steele KM, DeMers MS, Schwartz MH, et al. Compressive tibiofemoral force during crouch gait. *Gait & Posture* 2012; 35: 556–560.

93. Kim HJ, Fernandez JW, Akbarshahi M, et al. Evaluation of predicted knee-joint muscle forces during gait using an instrumented knee implant. *Journal of Orthopaedic Research* 2009; 27: 1326–1331.

94. Fregly BJ, Reinbolt JA, Rooney KL, et al. Design of patient-specific gait modifications for knee osteoarthritis rehabilitation. *Biomedical Engineering, IEEE Transactions on* 2007; 54: 1687–1695.

95. Schache AG, Fregly BJ, Crossley KM, et al. The effect of gait modification on the external knee adduction moment is reference frame dependent. *Clinical Biomechanics* 2008; 23: 601–608.

96. Walter JP, D'Lima DD, Colwell CW, et al. Decreased knee adduction moment does not guarantee decreased medial contact force during gait. *Journal of Orthopaedic Research* 2010; 28: 1348–1354.

97. Ali A, Sundberg M, Robertsson O, et al. Dissatisfied patients after total knee arthroplasty: A registry study involving 114 patients with 8–13 years of follow-up. *Acta Orthopaedica* 2014; 85: 229–233.

98. Noble PC, Gordon MJ, Weiss JM, et al. Does Total Knee Replacement Restore Normal Knee Function?: *Clinical Orthopaedics and Related Research* 2005; 157–165.

99. Bonnefoy-Mazure A, Kämpfen S, Sagawa Junior Y, et al. Evolution of knee kinematics three months after total knee replacement. *Gait & Posture* 2015; 41: 624–629.

100. Rahman J, Tang Q, Monda M, et al. Gait assessment as a functional outcome measure in total knee arthroplasty: a cross-sectional study. *BMC Musculoskeletal Disorders* 2015; 16: 66.

101. Cates HE, Komistek RD, Mahfouz MR, et al. In Vivo Comparison of Knee Kinematics for Subjects Having Either a Posterior Stabilized or Cruciate Retaining High-Flexion Total Knee Arthroplasty. *The Journal of Arthroplasty* 2008; 23: 1057–1067.

102. Kramers-de Quervain IA, Kämpfen S, Munzinger U, et al. Prospective study of gait function before and 2years after total knee arthroplasty. *The Knee* 2012; 19: 622–627.

103. McClelland JA, Webster KE, Feller JA. Gait analysis of patients following total knee replacement: A systematic review. *The Knee* 2007; 14: 253–263.

104. Fedorov A, Beichel R, Kalpathy-Cramer J, et al. 3D Slicer as an image computing platform for the Quantitative Imaging Network. *Magnetic Resonance Imaging* 2012; 30: 1323–1341.

105. Cignoni P, Callieri M, Corsini M, et al. MeshLab: an Open-Source Mesh Processing Tool. 2008, p. 8.

106. Collette B, Falck D, Havre Y van. *FreeCAD [how-to]: solid modeling with the power of Python*. Birmingham Mumbai: Packt Publishing, 2012.

107. Fitzgibbon AW, Pilu M, Fisher RB. Direct least squares fitting of ellipses. In: *Proceedings of 13th International Conference on Pattern Recognition*. Vienna, Austria: IEEE, pp. 253–257 vol.1.

108. Shi J. *Finite element analysis of total knee replacement considering gait cycle load and malalignment*. Doctoral thesis. University of Wolverhampton, 2007, http://wlv.openrepository.com/wlv/handle/2436/14404.

109. Dai Y, Scuderi GR, Penninger C, et al. Increased shape and size offerings of femoral components improve fit during total knee arthroplasty. *Knee Surgery, Sports Traumatology, Arthroscopy* 2014; 22: 2931–2940.

110. meniscus function. [Internet]. c2011-04-22 [updated 2019 April 18]; [cited 2019 March]. Available from: http://www.ivysportsmed.com/en/knee-pain/meniscus-function.

111. Seth A, Sherman M, Reinbolt JA, et al. OpenSim: a musculoskeletal modeling and simulation framework for in silico investigations and exchange. *Procedia IUTAM* 2011; 2: 212–232.

112. Anderson FC, John CT, Guendelman E, et al. SimTrack: Software for Rapidly Generating Muscle-Actuated Simulations of Long-Duration Movement. Available from:https://simtk.org/docman/view.php/55/1500/Anderson_SimTrack_ISOBME 2006.pdf

113. John CT. Residual Reduction Algorithm (RRA). 2008; 6. Available from: https://simtk.org/docman/view.php/55/1501/RRA_COMAdjustmentBackOfTheE nvelopeCalculations.pdf

114. Thelen DG, Anderson FC. Using computed muscle control to generate forward dynamic simulations of human walking from experimental data. *Journal of Biomechanics* 2006; 39: 1107–1115.

115. Thelen DG, Anderson FC, Delp SL. Generating dynamic simulations of movement using computed muscle control. *Journal of Biomechanics* 2003; 36: 321–328.

116. Machado MMF. *A multibody approach to the contact dynamics : a knee joint application*. Ph.D. Thesis, University of Minho, Portugal, 2013.

117. Simtk.org: Grand Challenge Competition to Predict In Vivo Knee Loads: Overview. [Internet]. c2011-04-22 [updated 2019 April 18]; [cited 2019 March] Available from: https://simtk.org/home/kneeloads.

118. Examples and Tutorials - OpenSim documentation. [Internet]. c1985-10-04 [updated 2019 June 26]; [cited 2019 March] Available from: https://simtk-confluence.stanford.edu/display/OpenSim/Examples+and+Tutorials.

119. Getting Started with RRA/ OpenSim Documentation. [Internet]. c1985-10-04 [updated 2019 June 26]; [cited 2019 March] Available from: https://simtk-confluence.stanford.edu/display/OpenSim/Getting+Started+with+RRA.

120. Marchetti PH, Jarbas da Silva J, Jon Schoenfeld B, et al. Muscle Activation Differs between Three Different Knee Joint-Angle Positions during a Maximal Isometric Back Squat Exercise. *Journal of Sports Medicine* 2016; 2016: 1–6.

121. Slater LV, Hart JM. Muscle activation patterns during different squat techniques. *Journal of Strength and Conditioning Research* 2017; 31: 667–676.

122. McCaw ST, Melrose DR. Stance width and bar load effects on leg muscle activity during the parallel squat. *Medicine & Science in Sports & Exercise* 1995; 27: S159.

123. Wibawa AD, Verdonschot N, Halbertsma JPK, et al. A Trap Motion in Validating Muscle Activity Prediction from Musculoskeletal model using EMG. *International Journal of Bio-Science and Bio-Technology* 2017; 8: 61–72.

124. Navacchia A, Myers CA, Rullkoetter PJ, et al. Prediction of in vivo knee joint loads using a global probabilistic analysis. *Journal of biomechanical engineering* 2016; 138: 031002.

125. Thelen DG, Won Choi K, Schmitz AM. Co-simulation of neuromuscular dynamics and knee mechanics during human walking. *Journal of Biomechanical Engineering* 2014; 136: 021033.

126. Zheng L, Li K, Shetye S, et al. Integrating dynamic stereo-radiography and surface-based motion data for subject-specific musculoskeletal dynamic modeling. *Journal of Biomechanics* 2014; 47: 3217–3221.

127. Adouni M, Shirazi-Adl A. Evaluation of knee joint muscle forces and tissue stresses-strains during gait in severe OA versus normal subjects. *Journal of Orthopaedic Research* 2014; 32: 69–78.

128. Trinler U, Leboeuf F, Hollands K, et al. Estimation of muscle activation during different walking speeds with two mathematical approaches compared to surface EMG. *Gait & Posture* 2018; 64: 266–273.

129. Browne C, Hermida JC, Bergula A, et al. Patellofemoral forces after total knee arthroplasty: effect of extensor moment arm. *The Knee* 2005; 12: 81–88.

130. Walker PS, Sathasivam S. Controlling the motion of total knee replacements using intercondylar guide surfaces. *Journal of Orthopaedic Research* 2000; 18: 48–55.

131. Walker PS. The design and pre-clinical evaluation of knee replacements for osteoarthritis. *Journal of Biomechanics* 2015; 48: 742–749.

132. Walker PS, Heller Y, Yildirim G, et al. Reference axes for comparing the motion of knee replacements with the anatomic knee. *The Knee* 2011; 18: 312–316.

133. Asano T, Akagi M, Nakamura T. The functional flexion-extension axis of the knee corresponds to the surgical epicondylar Axis. *The Journal of Arthroplasty* 2005; 20: 1060–1067.

134. Cherian JJ, Kapadia BH, Banerjee S, et al. Mechanical, anatomical, and kinematic axis in TKA: concepts and practical applications. *Current Reviews in Musculoskeletal Medicine* 2014; 7: 89–95.

135. Eckhoff D, Hogan C, DiMatteo L, et al. Difference between the epicondylar and cylindrical axis of the knee. *Clinical Orthopaedics and Related Research* 2007; 238–244.

136. Feng Y, Tsai T-Y, Li J-S, et al. In-vivo analysis of flexion axes of the knee: Femoral condylar motion during dynamic knee flexion. *Clinical Biomechanics* 2016; 32: 102–107.

137. Kobayashi H, Akamatsu Y, Kumagai K, et al. Is the surgical epicondylar axis the center of rotation in the osteoarthritic knee? *The Journal of Arthroplasty* 2015; 30: 479–483.

138. Wünschel M, Leichtle U, Lo J, et al. Differences in tibiofemoral kinematics between the unloaded robotic passive path and a weightbearing knee simulator. *Orthopedic Reviews* 2012; 4: 6–8.

139. Yildirim G, Walker PS, Boyer J. Total knees designed for normal kinematics evaluated in an up-and-down crouching machine. *Journal of Orthopaedic Research* 2009; 27: 1022–1027.

140. Zachman NJ, Hillberry BM, Kettelkamp DB. *Design of a load simulator for the dynamic evaluation of prosthetic knee joints*. ASME publication, https://books.google.co.uk/books?id=lCxIGwAACAAJ (1978).

141. Halloran JP, Clary CW, Maletsky LP, et al. Verification of predicted knee replacement kinematics during simulated gait in the Kansas Knee Simulator. *Journal of Biomechanical Engineering* 2010; 132: 081010-081010–6.

142. Buschmann J, Meier Bürgisser G. Biomechanical properties of tendons and ligaments in humans and animals. In: *Biomechanics of Tendons and Ligaments*. Elsevier, pp. 31–61.

143. Butler D, Kay M, Stouffer D. Comparison of material properties in fascicle-bone units from human patellar tendon and knee ligaments. *Journal of Biomechanics* 1986; 19(6): 425–32.

144. LaValle SM. *Planning Algorithms*. Cambridge: Cambridge University Press. 2006. DOI: 10.1017/CBO9780511546877.

145. Wie B. *Part III. Attitude Dynamics and Control, Space Vehicle Dynamics and Control (2nd Edition)*. American Institute of Aeronautics and Astronautics, 2008.

146. Zhao D, Banks SA, D'Lima DD, et al. In vivo medial and lateral tibial loads during dynamic and high flexion activities. *Journal of Orthopaedic Research* 2007; 25: 593–602.

147. Mündermann A, Dyrby CO, D'Lima DD, et al. In vivo knee loading characteristics during activities of daily living as measured by an instrumented total knee replacement. *Journal of Orthopaedic Research* 2008; 26: 1167–1172.

148. Taylor WR, Schütz P, Bergmann G, et al. A comprehensive assessment of the musculoskeletal system: The CAMS-Knee data set. *Journal of Biomechanics* 2017; 65: 32–39.

149. Bergmann G, Bender A, Graichen F, et al. Standardized Loads Acting in Knee Implants. *PLoS ONE* 2014; 9: e86035.

150. Kutzner I, Heinlein B, Graichen F, et al. Loading of the Knee Joint During Activities of Daily Living Measured in Vivo in Five Subjects. *Journal of Biomechanics* 2010; 43: 2164–2173.

151. Stylianou AP, Guess TM, Kia M. Multibody Muscle Driven Model of an Instrumented Prosthetic Knee During Squat and Toe Rise Motions. *Journal of Biomechanical Engineering* 2013; 135: 041008.

152. Wilson DR, Feikes JD, Zavatsky AB, et al. The components of passive knee movement are coupled to flexion angle. *Journal of biomechanics* 2000; 33: 465–473.

153. Schmitz A, Piovesan D. Development of an Open-Source, Discrete Element Knee Model. *IEEE Transactions on Biomedical Engineering* 2016; 63: 2056–2067.

154. Murakami K, Hamai S, Okazaki K, et al. In vivo kinematics of healthy male knees during squat and golf swing using image-matching techniques. *The Knee* 2016; 23: 221–226.

155. Tamaki M, Tomita T, Watanabe T, et al. In Vivo Kinematic Analysis of a High-Flexion, Posterior-Stabilized, Mobile-Bearing Knee Prosthesis in Deep Knee Bending Motion. *The Journal of Arthroplasty* 2009; 24: 972–978.

156. Beynnon BD, Fleming BC. Anterior cruciate ligament strain in-vivo: A review of previous work. *Journal of Biomechanics* 1998; 31: 519–525.

157. Li G, DeFrate LE, Sun H, et al. In Vivo Elongation of the Anterior Cruciate Ligament and Posterior Cruciate Ligament during Knee Flexion. *The American Journal of Sports Medicine* 2004; 32: 1415–1420.

158. Hosseini A, Gill TJ, Li G. In vivo anterior cruciate ligament elongation in response to axial tibial loads. *Journal of Orthopaedic Science* 2009; 14: 298–306.

159. Willing R, Kim IY. Design Optimization of a Total Knee Replacement for Improved Constraint and Flexion Kinematics. *Journal of Biomechanics* 2011; 44: 1014–1020.

160. Ardestani MM, Moazen M, Jin Z. Contribution of geometric design parameters to knee implant performance: Conflicting impact of conformity on kinematics and contact mechanics. *The Knee* 2015; 22: 217–224.

161. Uvehammer J, Kärrholm J, Brandsson S, et al. *In vivo* kinematics of total knee arthroplasty: Flat compared with concave tibial joint surface. *Journal of Orthopaedic Research* 2000; 18: 856–864.

162. O'Brien TD, Reeves ND, Baltzopoulos V, et al. Mechanical properties of the patellar tendon in adults and children. *Journal of Biomechanics* 2010; 43: 1190–1195.

163. Taylor M, Barrett DS. Explicit Finite Element Simulation of Eccentric Loading in Total Knee Replacement: *Clinical Orthopaedics and Related Research* 2003; 414: 162–171.

164. Chu T. An Investigation on Contact Stresses of New Jersey Low Contact Stress (NJLCS) Knee Using Finite Element Method. *Journal of Systems Integration* 1999; 9: 187–199.

165. Carr BC, Goswami T. Knee implants – Review of models and biomechanics. *Materials & Design* 2009; 30: 398–413.

166. Simpson DJ, Gray H, D'Lima D, et al. The effect of bearing congruency, thickness and alignment on the stresses in unicompartmental knee replacements. *Clinical Biomechanics* 2008; 23: 1148–1157.

167. Ries MD, Weaver K, Rose RM, et al. Fatigue strength of polyethylene after sterilization by gamma irradiation or ethylene oxide. *Clinical orthopaedics and related research* 1996; 87–95.

168. Abdel MP, Parratte S, Budhiparama NC. The patella in total knee arthroplasty: to resurface or not is the question. *Current Reviews in Musculoskeletal Medicine* 2014; 7: 117–124.

169. Matsuda S, Ishinishi T, White E, et al. Patellofemoral joint after total knee arthroplasty effect on contact area and contact Stress. *The Journal of Arthroplasty* 1997; 12: 790–797.

170. Mason JJ, Leszko F, Johnson T, et al. Patellofemoral joint forces. *Journal of Biomechanics* 2008; 41: 2337–2348.

171. Trepczynski A, Kutzner I, Kornaropoulos E, et al. Patellofemoral joint contact forces during activities with high knee flexion. *Journal of Orthopaedic Research* 2012; 30: 408–415.

172. Fekete G, MáLnáSi Csizmadia B, Abdel Wahab M, et al. Patellofemoral model of the knee joint under nonstandard squatting. *DYNA* 2014; 81: 60.

173. Komistek RD, Kane TR, Mahfouz M, et al. Knee mechanics: a review of past and present techniques to determine in vivo loads. *Journal of Biomechanics* 2005; 38: 215–228.

174. Sharma A, Leszko F, Komistek RD, et al. In vivo patellofemoral forces in high flexion total knee arthroplasty. *Journal of Biomechanics* 2008; 41: 642–648.

175. Dagneaux L, Thoreux P, Eustache B, et al. Sequential 3D analysis of patellofemoral kinematics from biplanar x-rays: In vitro validation protocol. *Orthopaedics & Traumatology: Surgery & Research* 2015; 101: 811–818.

176. Churchill DL, Incavo SJ, Johnson CC, et al. The influence of femoral rollback on patellofemoral contact loads in total knee arthroplasty. *The Journal of Arthroplasty* 2001; 16: 909–918.

177. Cohen ZA, Roglic H, Grelsamer RP, et al. Patellofemoral Stresses during Open and Closed Kinetic Chain Exercises: An Analysis Using Computer Simulation. *The American Journal of Sports Medicine* 2001; 29: 480–487.